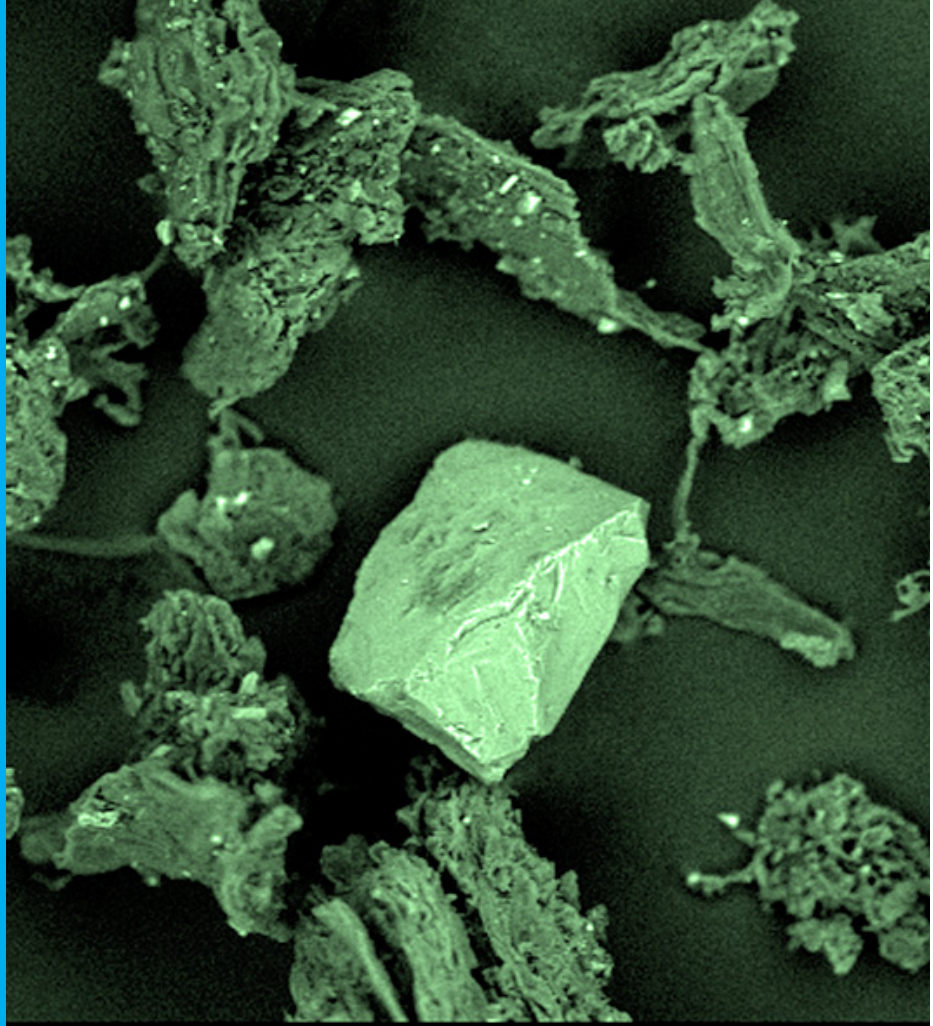

TECHNOLOGY • RESEARCH HIGHLIGHTS • VISIONS • SCIENCE •

210

Biomass gasification fundamentals to support the development of BTL in forest industry

Publishable final scientific report of Nordsyngas project

VTT

VTT TECHNOLOGY 210

Biomass gasification fundamentals to support the development of BTL in forest industry

Publishable final scientific report of Nordsyngas project

Edited by

Minna Kurkela

ISBN 978-951-38-8220-4 (URL: http://www.vtt.fi/publications/index.jsp)

VTT Technology 210

ISSN-L 2242-1211
ISSN 2242-122X (Online)

JULKAISIJA – UTGIVARE – PUBLISHER

Teknologian tutkimuskeskus VTT Oy
PL 1000 (Tekniikantie 4 A, Espoo)
02044 VTT
Puh. 020 722 111, faksi 020 722 7001

Teknologiska forskningscentralen VTT Ab
PB 1000 (Teknikvägen 4 A, Esbo)
FI-02044 VTT
Tfn +358 20 722 111, telefax +358 20 722 7001

VTT Technical Research Centre of Finland Ltd
P.O. Box 1000 (Tekniikantie 4 A, Espoo)
FI-02044 VTT, Finland
Tel. +358 20 722 111, fax +358 20 722 7001

Cover image: SEM image of bark char, SINTEF Energy Research

Preface

The research described herein was carried out during the period 2010–2014 as part of the project "Biomass gasification fundamentals to support the development of BTL in forest industry". This project, known as the NORDSYNGAS-project number TFi PK-bio 03, was coordinated by VTT Technical Research Centre of Finland Ltd.

NORDSYNGAS was funded by the Nordic Energy Research under Top-level Research Initiative (TRI) Programme "Sustainable biofuels". Additional funding was pro-vided by VTT.

The work of the project was carried out in co-operation with the following project participants:

VTT Technical Research Centre of Finland Ltd	www.vtt.fi
ETC Energy Technology Centre, Sweden	http://www.etcpitea.se/
LTU Luleå University of Technology, Sweden	http://www.ltu.se/
SINTEF Energy Research, Norway	http://www.sintef.no/

Contents

Executive summary

The overall objective of this project was to create new scientific knowledge on fluidised-bed and entrained-flow gasification of biomass residues and black liquor in order to support the Nordic industrial development and demonstration projects. The aim of the project was broken into the following more specific objectives:

- The fate of alkali metals and other inorganic species in the conditions of pressurised fluidised-bed and entrained flow gasification.
- Data on fuel pyrolysis and reactivity in the conditions of entrained-flow gasification and to incorporate this data in the reactor modelling.
- The fate of inorganic species with regards to fouling in gas coolers, to the removal efficiency in hot gas filtration and with respect to slag formation in entrained flow gasifiers.
- System studies on BTL integrated to forest industry

The project was realised in four work packages (WP) in the co-operation between the Finnish, Swedish and Norwegian R&D organisations VTT, ETC, LTU and SINTEF Energy Research. Also the contribution of Umeå University was significant.

The titles of the work packages and the involvement of the partners in the different work packages are the following:

WP1. Experimental studies and modelling of pressurised fluidised-bed gasification of biomass fuels, temperature below 1000ºC and pressure range 1-20 bar (VTT, SINTEF)

WP2. Studies on entrained-flow gasification of black liquor and woody biomass (ETC, LTU)

WP3. Fate of inorganic species during gasification, gas cooling and filtration (SINTEF, VTT, LTU)

WP4. System studies on biomass-to-liquids integrated to forest industry (LTU)

WP1 Experimental studies and modelling of pressurised fluidised-bed gasification of biomass fuels, temperature below 1000ºC and pressure range 1–20 bar

The char formation and its effect on reactivity was studied to create data for the modelling of carbon conversion. The conditions simulated biomass feeding into a pressurised gasifier.

The pyrolysis took place in the same gas atmosphere and at the same pressure and temperature as used for the char gasification test. The main result was that the sample amount and its layer thickness plays a role in the char formation and also has a significant effect on char reactivity. This was concluded after the biomass sample amount and gas velocity was varied and compared with the tests that had been carried out with char samples prepared separately in another reactor. The result indicates that the sample amount and its layer thickness as well as the gas flow passing the sample should be optimized, before any kinetic parameters can be determined. This work needs to be carried out in a further research project.

Two different thermogravimetric (TGA) set-ups in SINTEF and VTT were compared for the reactivity measurements. Both TGAs operated under high heating rate. Comparison tests gave the same results in spite of the remarkable difference of sample amounts of 5 mg in SINTEF and the one of 100-200 mg in VTT. Reason for this result was assumed to be in the low linear gas velocities passing the samples. The low gas velocity may not be able to transport the volatilising material from the sample layer during pyrolysis and thereby secondary carbon may be formed due to the cracking of the volatile compounds which has a lower reactivity than that of fresh biomass char.

WP2 Studies on entrained-flow gasification of black liquor and woody biomass

The results showed that methane could not be predicted at the outlet of the gasifier. The experiments showed a methane concentration ranging from 0.5 % mol to about 2.5% mol whilst the model predicted 0%. In order to resolve and investigate the influence of this, CH_4 concentration had to be prescribed, by treating part of the CH_4 as inert, in order to get reasonable predictions for the main gas components.

OpenFOAM appears to be at least as capable as Ansys CFX in simulating biomass gasification or combustion.

The studies of the particulate matter in the entrained flow (EF) gasification showed that particles with an aerodynamic diameter < 1 µm submicron particles dominate the particle size distribution in the syngas after the quench during entrained flow gasification of biomass. Practically this means that an advanced gas cleaning technology, e.g. filter or electrostatic precipitator, need to be installed downstream the quench if the particle concentration needs to be reduced further. The elemental composition of the submicron particles are dominated by carbon with smaller amounts of easily volatile ash forming elements K, S, Cl, and Z, and traces of refractory elements Si, Ca, Mg, and Fe. A significantly larger fraction of

the zinc introduced to the gasifier with the fuel ends up in the submicron fraction compared to the other easily volatile ash elements potassium, chlorine and sulphur. The amount of ash forming elements in the submicron particles is significant dependent on the parent fuel ash composition and increases with increasing ash content of the parent fuels. Therefore, the concentration of ash forming elements in the submicron particles was higher for bark compared to stem wood. Smaller particle sizes in the particle mass size distribution have a higher concentration of ash forming elements compared to larger particle sizes. Submicron particles could penetrate through the quench scrubber system to some extent. The resulting particle concentration in the raw syngas after the quench varied between 46-289 mg/Nm3 in this work. Practically this means that the particle concentration needs to be reduced several order of magnitudes before it for example can be used in a catalytic process for production of liquid fuels.

Two types of classic soot particles are formed during EF gasification of low ash content stem wood. Traces of metallic potassium could also be found in these particles. The concentration of ash forming elements significantly influences the type of individual particles formed during entrained flow gasification of biomass. For bark, several types of particles could be identified following its concentration of carbon and ash forming elements, i.e., soot particles, graphite flakes, ash forming element dominated particles, zinc dominated particles and finally pure zinc particles. Zinc interacts in the formation of the particles.

In the study of fuel particle conversion of pulverized biomass during pyrolysis in an entrained flow reactor (laminar-flow) it was observed that first, biomass swelled by thermal expansion, and then shrank during initial stage of pyrolysis. Whereas char experienced the plastic stage during pyrolysis, volatiles that existed inside char particles were released outside the char particles due to its high internal pressure. At the same time, primary fragmentation of char particles occurred by the force from the gas flow. Ash forming elements were first released from the char particles to the gas phase and then adsorbed on the surface of char. Incomplete pyrolysis conversion of biomass was observed for the particle size of 500−1000 μm with the short reaction zone (650 mm). The particle simulation successfully predicted transition of high fuel conversion of biomass particle to low conversion quantitatively. Particle simulation showed that the fuel conversion in an entrained flow reactor depended on the competition between residence time and the time required for the pyrolysis. High reaction temperature, small particles, and slower gas flow were favorable for high fuel conversion.

The char gasification study of black liquor and pyrolysis oil mixture concluded that mixed samples showed high reactivity, not significantly different from that of black liquor, implying strong catalytic activity of alkali from black liquor in the mixtures. Char reactivity of black liquor and mixed samples were significantly higher than those for other types of biomass. Char reactivity determined for black liquor was slightly higher than that from extrapolation of a previous study at lower temperatures. The samples of black liquor and mixtures showed similar degree of char carbon conversion. The pyrolysis char yield was approximately constant for black liquor and mixtures even though ash content decreases with increasing

pyrolysis oil fraction. The random pore model with Arrhenius equation was found to fit the dynamics of char conversion in CO_2 well. However, the effect of CO_2 pressure on reactivity did not follow typical relations for other types of biomass. The results indicate that the black liquor gasification process may also be used for mixture of pyrolysis oil and black liquor without major modification.

The study of the high-speed interferometric measurement and visualization of the conversion of a black liquor droplet during laser heating showed that the holographic interferometry can be used to measure the velocity of the gases released during heating of a black liquor drop as well as the swelling of the drop. It is also possible to roughly estimate the temperature profile of the ejected gas bursts.

WP3: Fate of inorganic species during gasification, gas cooling and filtration
Comparison of the elemental compositions of possible melts within actual reactor deposits and those predicted by thermochemical equilibrium calculations for pressurised entrained-flow gasification (PEFG) of wood and bark fuels have shown large discrepancies. The most obvious difference is the enrichment of Si and reduction of Ca in the actual deposits compared to their respective calculation results, as well as compared to the fuel ash compositions. In bark derived deposits that there are interactions between K, Ca and Si upon quartz and feldspar particles. This demonstrates the fractionation of different ash-forming elements during the PEFG process can lead to speciation of particular phases. Such instances constitute localised behaviour that cannot be adequately studied with global thermodynamic analysis. Hence, ascertaining the ash fractionation and speciation in different regions and pathways through the reactor is necessary to enable appropriate thermochemical equilibrium modelling of such localised interactions. Consequently, these more relevant comparisons would, in turn, lead to greater elucidation of the ash transformation processes during the PEFG process. In addition to the ash collections, there must also be longer and more consistent experimental campaigns. The experimental campaigns utilised for this study had interruptions and did not reach steady-state, as least thermally. Further knowledge such as reactions kinetics and bulk process phenomena is also required in order to refine calculation inputs and interpretation of results.

When no additive is present, it was concluded:

- Oxide melt formation potential is greater for the bark fuel than wood fuel
- Potassium is readily volatilised from wood and bark with increasing temperature
- Substantial amounts of Ca and Si can also be volatilised for both wood and bark fuels when the temperature 1600–1800 °C
- More elements are stabilised into the oxide melt and solubility of CO_2 is higher with increasing pressures. These occur relatively more markedly for the wood fuel.
- For wood, crystalline CaO and Ca-silicates can exist up to 1800–2000 °C but their levels are reduced with increasing pressure; instead Si and Ca stabilise within the oxide melt

- For bark, there is a tendency to form crystalline Ca-silicates at temperatures below 1300 °C independent of pressure, giving rise to similarity in the fractionation of Si and Ca

When kaolinite additive is present, it was concluded:

- Potassium volatility increases with increasing temperature and decreases with increasing levels of kaolinite additive.
- Increasing levels of the additive produces alkali/alkaline-aluminosilicate, aluminosilicate and aluminium oxide crystalline phases that can co-exist with the oxide melt phase at temperatures below 1600 °C
- Temperature plays a more significant role in determining the oxide melt composition than pressure
- Oxide melt viscosity generally decreases with increasing temperature, but increases with increasing amounts of additive
- Oxide melts from the bark fuel show significantly lower viscosities compared to those from the wood fuel

When olivine additive is present, it was concluded:

- The slag formation potential is lower than kaolinite; stabilisation of olivine group crystalline phases is favoured even up to high temperatures
- Temperature plays a more significant role in determining the oxide melt composition than pressure
- Viscosity of the oxide melt is lower than that for the kaolinite additive scenario
- Volatility of potassium is higher than for the kaolinite additive scenario

According to the comparison of the equilibrium calculations and the measured ash characteristics it looks that if the silicon is not included and the results seem to reflect better the analytical observations.

WP4: System studies on biomass-to-liquids integrated to forest industry

The techno-economic evaluation of methanol and ammonia production via integrated biomass gasification in an existing pulp and paper mill was performed. In general, methanol assumed to replace fossil gasoline showed good production profitability if exempted from taxes. The ammonia production was per produced unit, significantly more capital intensive than methanol production. The plant profitability in the ammonia cases was therefore lower in comparison to the profitability in the methanol cases. The highest efficiency and the most favourable economic benefits were reached when methanol was produced via parallel operation of a solid biomass gasifier and a black liquor gasifier. Favourable economies of scale effects were also obtained for this system due to the possibility to co-utilize upstream (air separation unit) as well as downstream process equipment (gas conditioning units and synthesis loop).

The main conclusion was that green chemical production via industrially integrated biomass gasification show technical and economic benefits compared to

stand-alone production alternatives. Integration of large scale biomass gasification system is therefore important in the development towards a more sustainable green chemical production.

A summary of each work packages with respect to achievements towards objectives is presented in the following chapters 1–5.

Chapter 1

Experimental studies and modelling of pressurised fluidised-bed gasification of biomass fuel and fate of inorganic species during gasification, gas cooling and filtration

Antero Moilanen, Jere Lehtinen, Minna Kurkela, Mirja Muhola, Sanna Tuomi and Esa Kurkela, VTT Technical Research Centre of Finland Ltd

Contents

1. Experimental studies and modelling of pressurised fluidised-bed gasification of biomass fuel

The task consisted of thermobalance measurement for determining parameters of char gasification reaction required by the gasifier model development. The measurements were carried out both under atmospheric and pressurised conditions with the pressurised TG of VTT and the high-heating-rate TGA of SINTEF-ER (1 bar pressure).

1.1 Gasification reactivity

1.1.1 Experimental

Three biomasses (bark, wood and pine) were selected for the samples and analysed in detail (Table 1). Also reed canary grass and forest residue samples were included.

Table 1. Fuel characteristics of the samples; dry matter basis except moisture (HHV=Higher heating value, O diff is oxygen determined by difference).

Sample	Moisture %	Volatiles %	Ash %	C %	H %	N %	S %	O diff %	HHV MJ/kg
Bark pellet Mönsterås	7.7	70.1	4.1	52.7	5.5	0.3	0.04	37.4	20.9
Wood pellet Glommersträsk	4.9	82.9	0.3	51.0	6.0	0.1	0.01	42.6	20.7
Pine bark Koirasaari	10.1	67.2	0.9	56.0	5.3	0.2	0.03	37.6	21.8
Pine bark Kattilavesi Uusikaupunki	-	68.4	1.7	58.3	5.4	0.16	0.02	36.1	23.0
Reed canary grass	12.3	74.3	7.4	46.0	5.6	1.2	0.09	39.7	18.5
Forest residue	10.5	76.2	2.6	51.8	5.7	0.4	0.03	39.5	21.1

Measurements were carried out at constant temperatures (isothermal measurement). In VTT's pressurised thermogravimetric instrument (Figure 1) the tests were executed under fast heating to resemble the heating occurring when the fuel is fed to a reactor. The heating of the sample took place in situ in the test conditions set in the reactor. The heating rate for the sample was high and it was produced by lowering the sample holder into the preheated reactor with a chain mechanism in the apparatus. The method is described more in detail in /1/. The lowering to the position at which the balance mechanism started to measure the weight took about 7 seconds. The maximum heating rate was therefore approximately 100 K/s when the reactor was heated to 850 °C. The sample holder was relatively heavy, weighing about 6 grams, so it heated up more slowly than the sample. Hence, the heating rate of the biomass sample was lower on average than the maximum 100 K/s. This behaviour of the weighing mechanism made it difficult to define the exact point on the weight-time curve (Figure 8) at which char gasification starts. For this reason, it was practical for the conversion to be calculated as total fuel conversion X_t (ash-free)

$$X_t = \frac{m_{sample,af} - m}{m_{sample,af}} \quad (1)$$

where $m_{sample,\ af}$ is the ash-free sample mass and m is the instantaneous sample mass. Reactivity was expressed as reaction (conversion) rate dX/dt or instantaneous reaction rate dX/dt/(1-X), where X is X_t. The rates were plotted against the conversion when the rates were compared.

The basic temperature in the reactivity measurements was 850 °C and the total pressure range 1–20 bar. The effect of pressure on char structure was studied with the samples obtained from PTG.

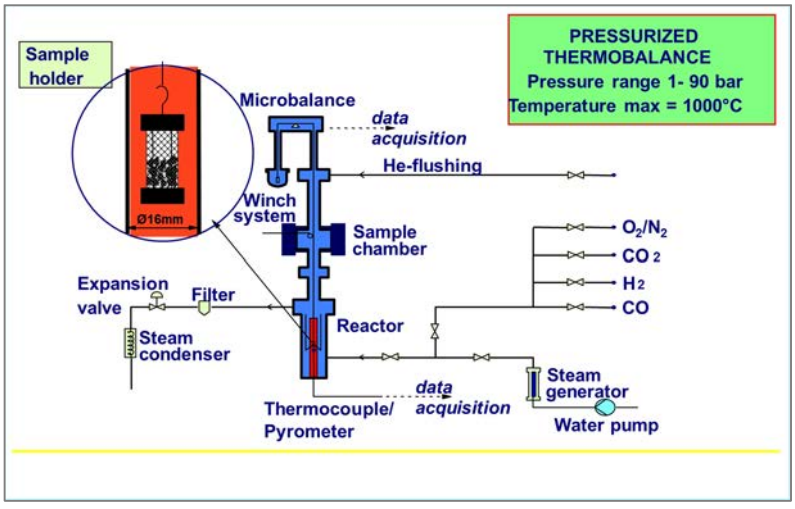

Figure 1. The schema of the pressurised thermobalance of VTT.

1.1.2 Results

For the samples, the main reactivity characteristics of the atmospheric gasification are presented in Figure 2. In general, the steam gasification reactivity was higher than that of CO_2. The highest steam gasification reactivity was measured for forest residue followed by Mönsterås bark pellett and Glommersträsk wood pellet. The reactivity of reed canary grass had a decreasing trend in the reaction rate with conversion in steam gasification. In CO_2 gasification, the forest residue had the highest reactivity at lower char conversion degrees (just after pyrolysis), and it reduced strongly to the same level as pine barks when the conversion increased. The reason for this is assumed to come from the inhomogeneity of the biomass. Forest residues consist of different wood parts having different reactivities, the most reactive parts react first. Reed canary grass had also high reactivity at lower char conversion degrees but it decreased significantly when the conversion increased. The lowest reactivities were measured for pine barks. In CO_2 the pine barks had the lowest reactivity and also the forest residue at higher conversion degrees.

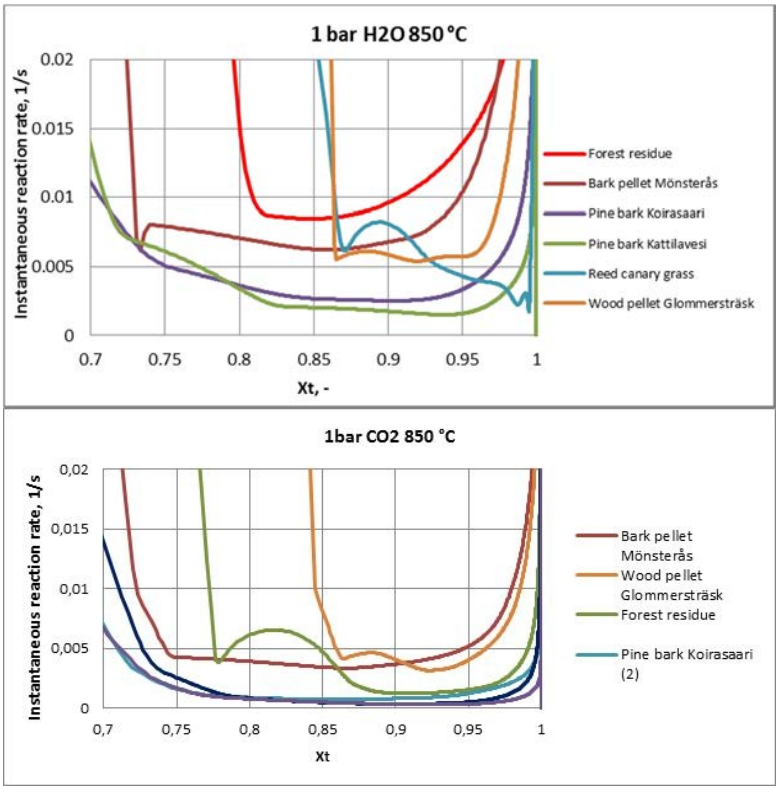

Figure 2. Comparison of the atmospheric steam (top) and CO_2 gasification reactivities of the samples at 850 °C.

1.2 Effect of pressure

The reactivity of bark pellet Mönsterås and wood pellet Glommersträsk decreased with the increase of pressure in CO_2 gasification (Figure 3), but for pine bark it seemed to have increasing reactivity trend with pressure, however it was observed that there was a great scattering in the results (see 1 bar test results in Figure 3 Pine bark Koirasaari). The reason for this scattering was assumed to come from the earlier observation that gasification reactivity of pine bark is dependent on the location in the tree; thick rind has significantly lower reactivity than that of thin bark taken e.g. from the upper tree parts /2/. For forest residue, the trend was decreasing. The CO_2 gasification reactivity for reed canary grass was not measured.

The steam gasification reactivity had an increasing trend with pressure except that of the reed canary grass (Figure 4). The increase of the reactivity with pressure was greatest when the pressure was raised from 1 bar to 5 bar and it levelled off with the further pressure increase. Furthermore, it was observed that the char formation conditions affect the reactivity, so this result of the pressure dependence is not reliable. The char formation and its effect on reactivity were studied under

conditions simulating biomass feeding into a pressurised biomass gasifier. The pyrolysis took place in the same gas atmosphere and at the same pressure and temperature as those used for the char gasification test. The most important result was that the sample amount and its layer thickness played a role in the char formation and also had a significant effect on the char reactivity (Figure 6). This means that the sample amount and its layer thickness as well as the gas flow passing the sample should be optimised before any kinetics can be measured reliably. When char samples prepared from the same biomass in a separate reactor were tested, no corresponding effect was found. The chars prepared separately had lower reactivity than the nascent chars obtained by pyrolysing biomass in situ under the same reactor conditions as those under which the reactivity was determined. This is probably due to the fresh (nascent) surface of char as well as catalytically active inorganic particles are more reactive than the char, which surface was in touch with air. How this phenomenon takes place in practise, for instance, inside large feedstock particles, need further studies. To build the reactivity model, this pyrolysis stage needs to be taken into account. The issue however is quite large so only qualitative measure for this project could be included. Also the char produced in the pressurised inert gas (10 bar N_2) had a lower the reactivity in CO_2 gasification carried out in lower pressure (5 bar) compared to that of the char generated directly in 5 bar CO_2 (Figure 5). The results are similar as it was observed by Cetin et al. /3/. In this work like Cetin it was observed that char formed in the pressurised conditions had a liquid like structure (Figure 7).

Char gasification model was developed in international co-operation (LTU, University of Sevilla, University of Jyväskylä and VTT) /4/. The model describes well CO_2 gasification but for steam gasification it still needs further development. The char gasification model was created using the results obtained earlier for a set of biomass samples. To study more the factors influencing this discrepancy, another effort was done using a set of 4 biomass samples from USA analysed in another VTT's project. Their ash chemical composition was analysed and possible compounds in different gasification conditions were determined using equilibrium calculations by Rainer Backman in UMU. The results have been published in Ref. /5/. The reactivity model seems to be possible to build for atmospheric pressure based on TG measurements.

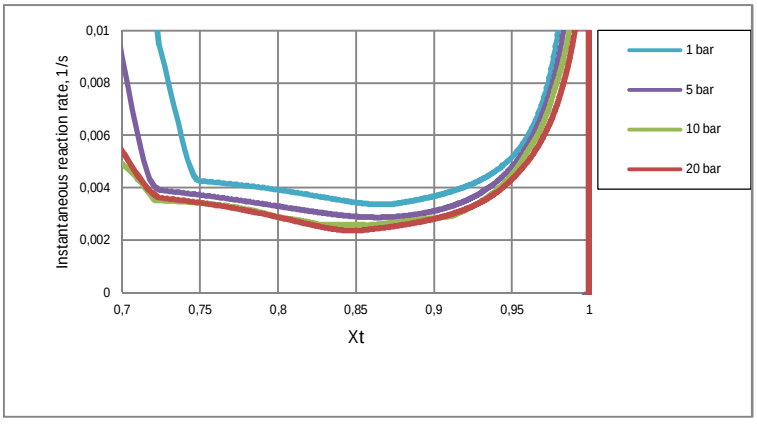

Bark pellet Mönsterås

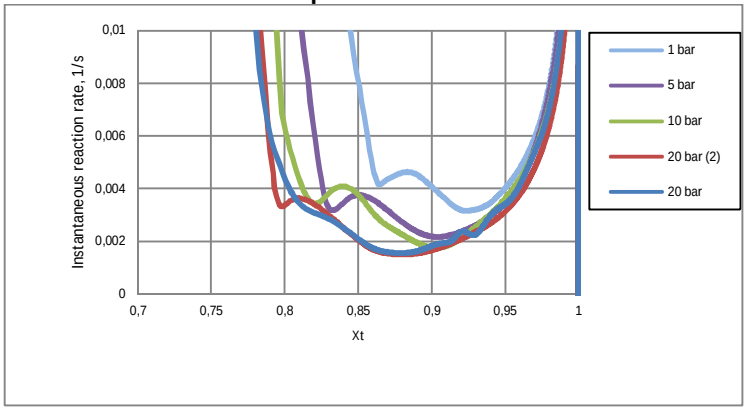

Wood pellet Glommersträsk

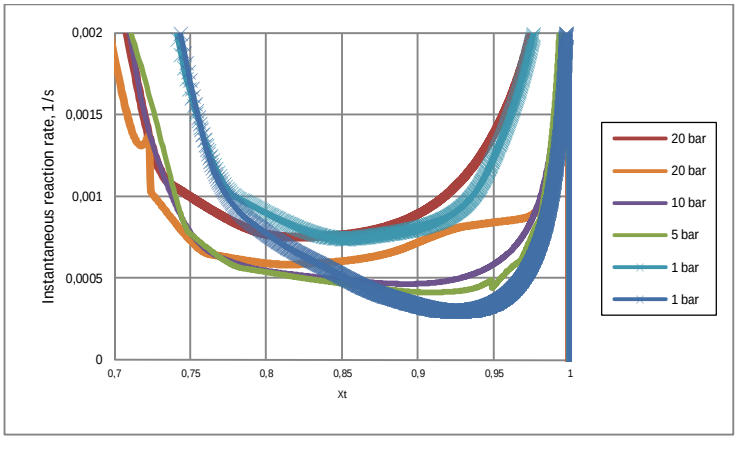

Pine bark Koirasaari

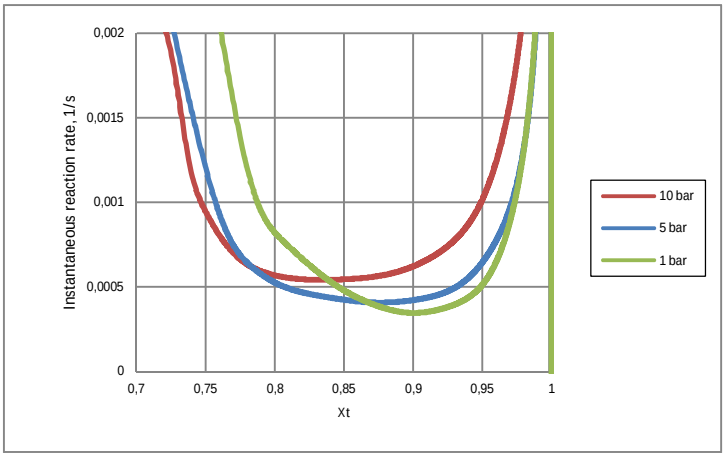

Pine bark Kattilavesi

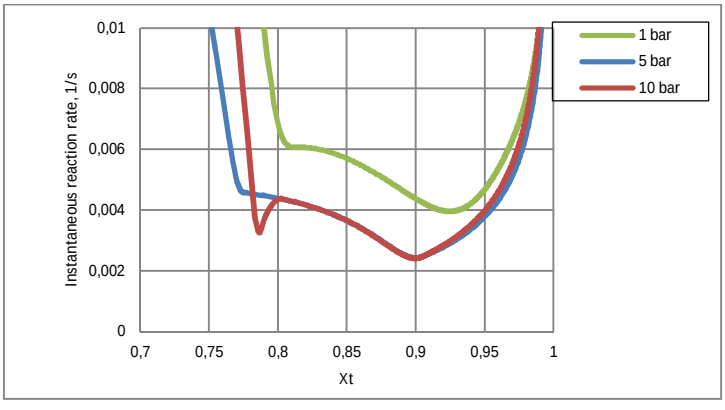

Forest residue

Figure 3. The effect of pressure in CO_2 gasification at 850 ºC of the samples.

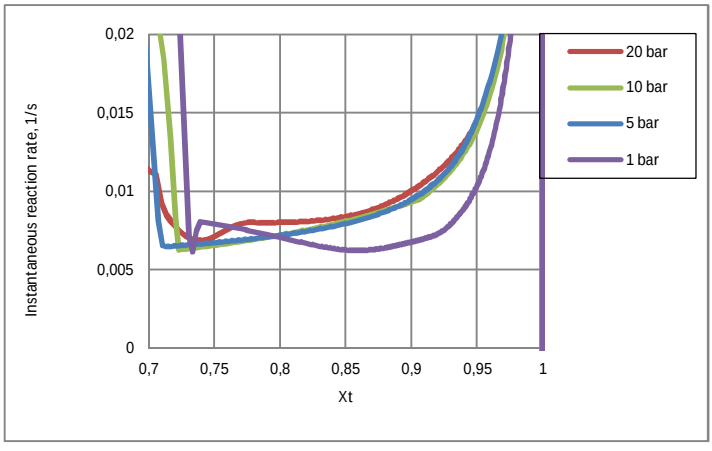

Bark pellet Mönsterås

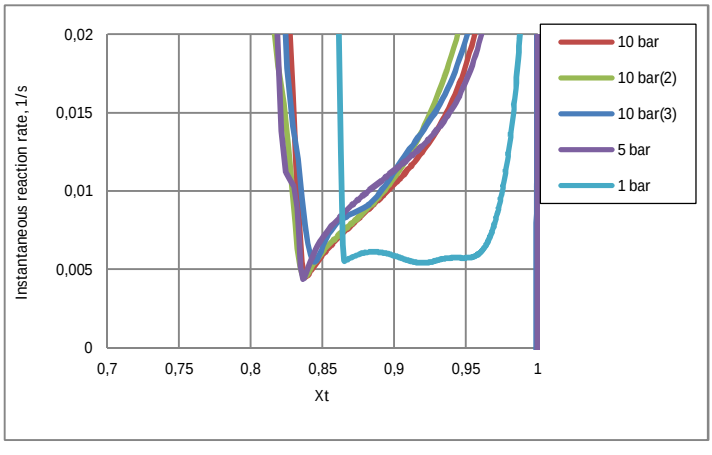

Wood pellet Glommersträsk

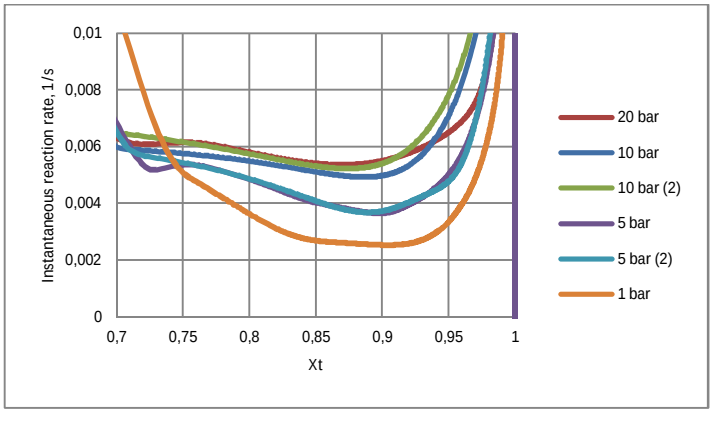

Pine bark Koirasaari

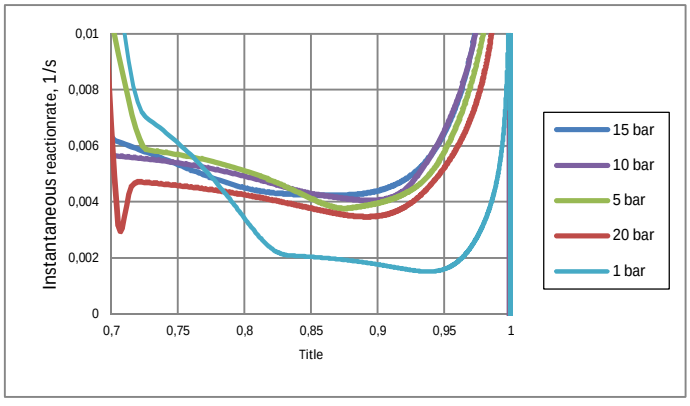

Pine bark Kattilavesi

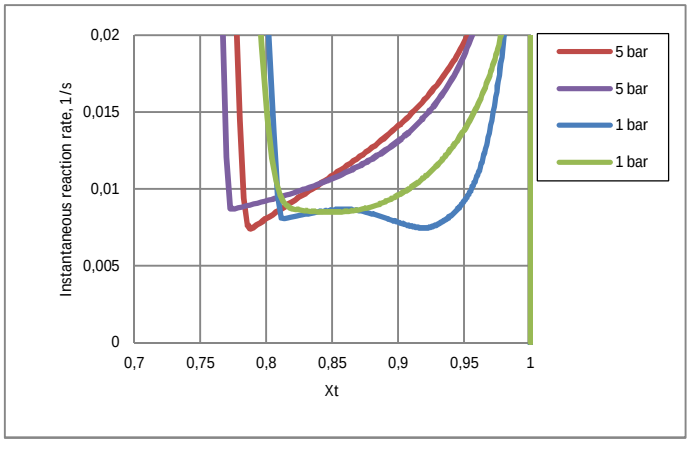

Forest residue

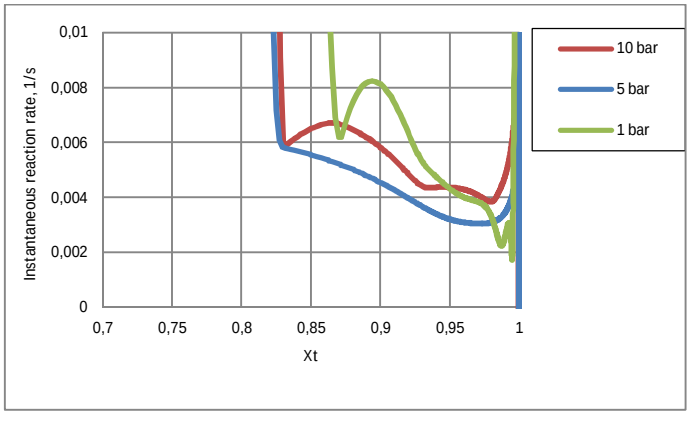

Reed canary grass

Figure 4. The effect of pressure in steam gasification at 850 °C of the samples.

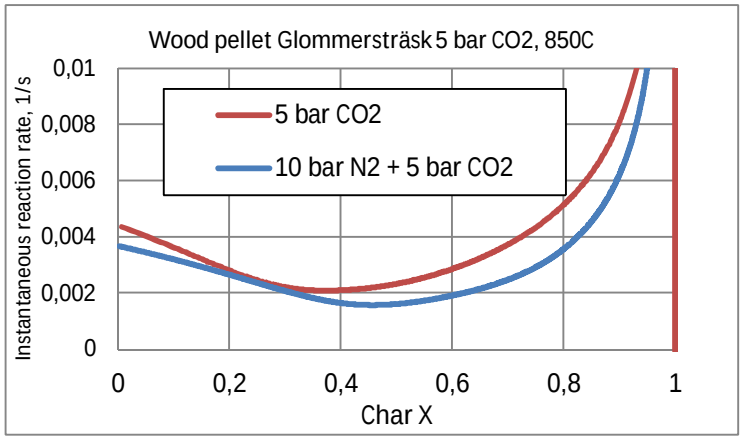

Figure 5. The effect of the pyrolysis pressure on CO_2 gasification at 850 °C of wood pellet Glommersträsk.

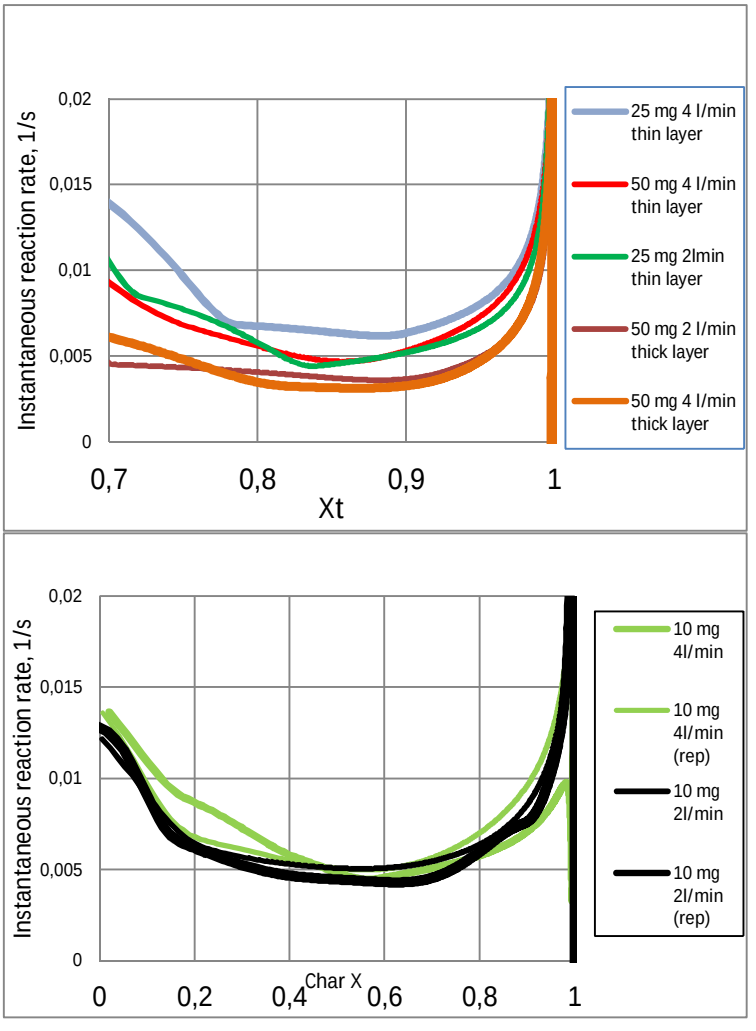

Figure 6. CO_2 gasification reactivity of bark pellet Mönsterås chars, which were prepared in situ in the TG reactor in 20 bar CO_2 at 850 °C (upper graph)and in a separate reactor (lower graph). Sample amounts, layer thickness and gas velocities are shown in the legend (rep.= repetition test, Char X = char conversion).

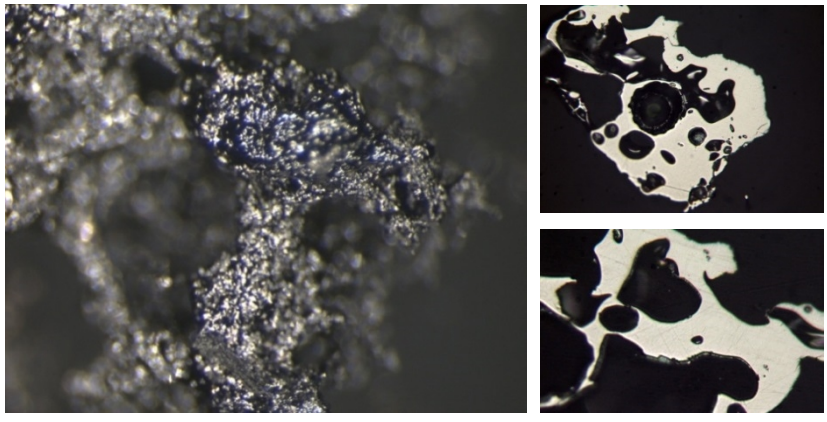

Figure 7. Molten structure of wood pellet char Glommersträsk prepared for 60 seconds at 1 MPa N_2 at 850 °C under the stereomicroscope; cross sections on the right.

1.3 Comparison of the thermogravimetric set-ups

Two different thermogravimetric set-ups were compared for the reactivity measurements /6/, both are able to operate under high heating rate but they have different operation principles: In the other TG (SINTEF), the high heating rate was produced with the controlled heating of the TG furnace in a so called jump mode. In the other one (VTT), the sample was introduced into the hot TG reactor using a winch system equipped in the apparatus. Typical weight and temperature behaviour with time of the both TGs are shown in Figure 8.

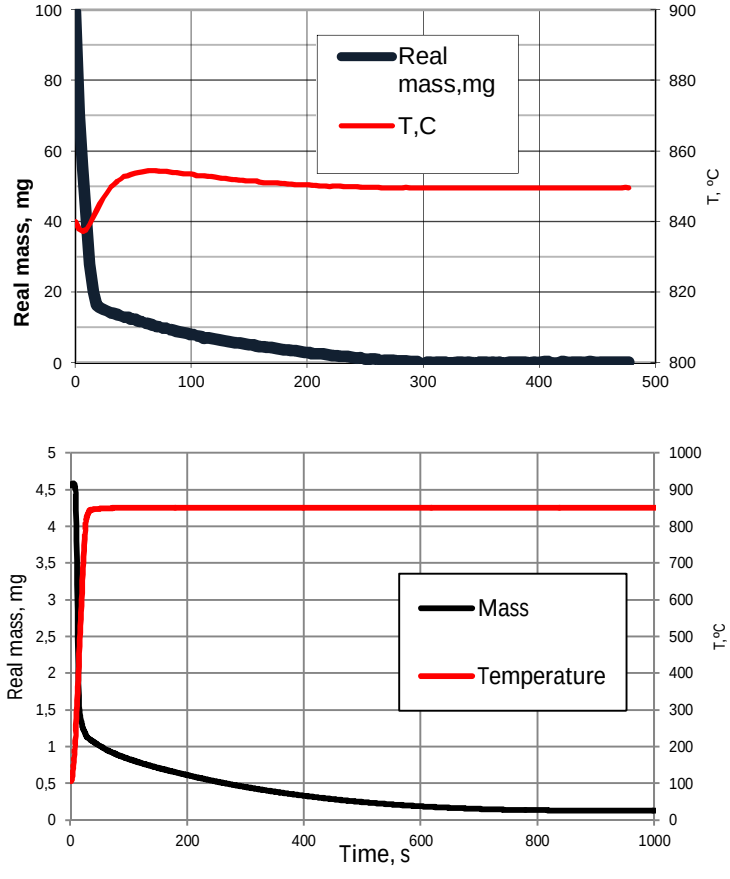

Figure 8. Weight and temperature against time of a typical TG measurement in VTT's TGA (top) and SINTEF's instrument where the jump mode was applied. The steep mass decrease during the first 30 seconds represents pyrolysis.

The structures of the sample arrangements in the sample holders are shown in Figure 9.

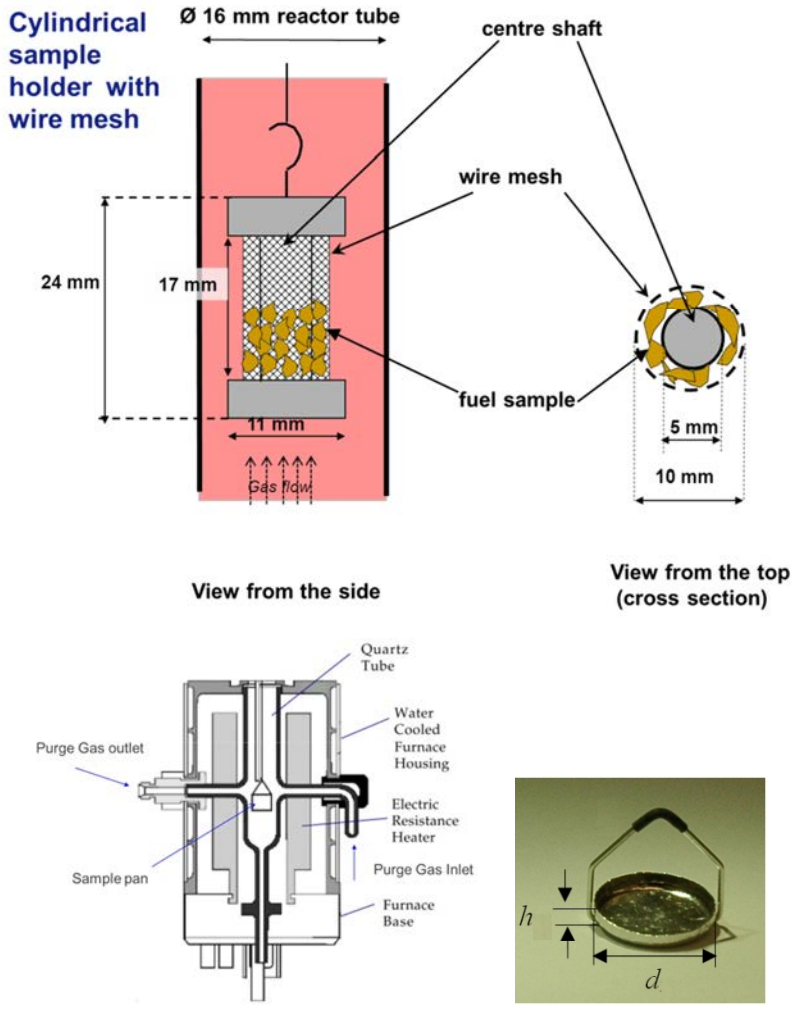

Figure 9. Structures of the sample holders and placement of the sample. VTT upper, SINTEF lower with the sample pan (d x h: 10 x 1 mm).

Comparison tests between two different thermobalances of SINTEF and VTT gave the same results in spite of the great difference in the sample amounts: 5 mg in SINTEF and 100–200 mg in VTT (Figure 10). The reason for these results may be that the linear gas velocities passing the samples were quite low. The gas flow rate in SINTEF's TG was 35 milliliter/min and that of VTT 1.5 liter/min. This low gas velocity may not be able to transport the volatilising material from the sample layer during pyrolysis and thereby secondary carbon may be formed due to the cracking of the volatile compounds which has a lower reactivity than that of fresh biomass char.

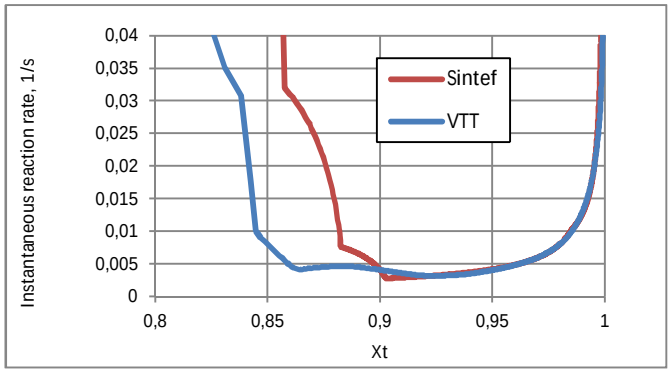

Wood pellet Glommersträsk

Figure 10. Comparison of CO_2 gasification reactivity bark pellet Mönsterås (up) and wood pellet Glommersträsk measured in SINTEF and in VTT in 1 bar CO_2 at 850 °C.

1.4 Conclusions

The effect of pressure on biomass char formation and reactivity was studied for pressurised gasification processes. The char samples were generated in in situ pyrolysis in TG with a high heating rate under the same conditions, under which the char gasification reactivity was measured. In the measurements, the sample amount and gas velocities were varied. The results were compared with the reactivities of the char samples prepared separately in another reactor. The results showed that the char reactivity was affected significantly by the pressurised pyrolysis conditions: the smaller the sample amount and the higher the gas velocity, the higher the reactivity. This behaviour was not observed for the chars generated in the separate reactor. The reason for this result was assumed to be in the behaviour of the volatiles during pyrolysis: under pressure, especially they form secondary char on the sample, and this char has lower reactivity and may block the active sites of the biomass char itself, lowering the reactivity of the whole char. This phenomenon was also observed in atmospheric conditions with big sample sizes. When biomass was pyrolysed under pressurised conditions, the char looked like molten metal, when inspected under microscope.

Furthermore, from this study it can be concluded that when kinetic parameters are to be measured for gasification, the char generation process should be taken into account. This means that the sample amount and its layer thickness as well as the gas flow passing the sample should be optimised. Chars prepared separately had lower reactivity than chars prepared in situ where nascent chars were formed.

Additionally, for entrained flow reactor, the higher temperature (> 1000 °C), than the one of fluidised bed reactor, affects the char properties through very high heating rate and also through the evaporation of catalytically active alkaline metals.

Two different (TGAs in SINTEF and VTT were compared for the reactivity measurements, both are able to operate under high heating rate. Comparison tests of the thermogravimetric set-ups gave the same results in spite of the great difference of sample amounts of (5 mg and 100–200 mg). Reason for these results was assumed to be in the low linear gas velocities passing the samples.

2. Fate of inorganic species during gasification, gas cooling and filtration

The study of this task aimed at the behaviour of ash forming components like alkali metals, heavy metals, chlorine in the conditions of fluidised-bed gasification. It contained chemical fractionation of the biomasses and chars, predictions of the ash composition in different parts of a biomass gasifier by means of the thermochemical model.

2.1 Experimental

The chemical fractionation (CF) analysis on the biomass samples and the chars derived from them was performed by Labtium laboratory. The biomass samples were those shown in Table 1 except forest residue and reed canary grass, also wood pellet Glommersträsk was not included, because of its too low ash content.

The char samples were prepared in TG, where biomass was gasified to desired conversion degrees. The tests were carried out in 1 bar steam gasification at 850 °C. The samples were bark pellet Mönsterås and pine bark Koirasaari. The char conversion degrees were approximately 0, 50 and 75%. The analysis comprised the total analysis and amount of water solubles. Acetate leaching tests were also carried out for determining the amount of ionexchangeable elements.

Fluidised bed experiments with VTT's AFB-test focused on the fate of inorganics during gasification (detailed analysis of hot filter dust)

2.2 Results

The results of the chemical fractionation of biomass samples are presented in Table 2 and Figs. 11 and 12. The evaluation of the chlorine behaviour was not possible due to very low chlorine contents in all the biomasses (the range of 0.01%). The results of the analysis carried out for char samples are presented in Table 3 and Figs. 13 and 14.

The distribution of the CF fractions of the bark samples (Mönsterås, pine barks Koirasaari and Kattilavesi) were rather similar, as shown in Figure12 and deviating from that of wood pellet.

The amounts of watersolubles in char as a function conversion degree, (Table 3 and Figures 13 and 14) showed that for Mönsterås, the trend was that the share of water soluble calcium increased from 6% up to 77% with conversion degree, but potassium seemed to be quite constant, for Mg and P no trend was seen, for Cu the trend seemed to be decreasing and the share of the water soluble copper could be quite high. For Mn and Zn the shares of water solubles were small, for Zn about 5%, and no trend with conversion was observed. For Al, Na and Si an increasing trend was seen. Ni, Cr and Fe results were not relevant in the char analysis since the sample holder of TG, in which char samples were prepared, contaminated them. The sample holder was made of inconel alloy containing iron, nickel and chrome. Pine bark Koirasaari had a different pattern in the watersolubles, than Mönsterås. The levels of watersolubles in general were somewhat higher than those of Mönsterås. For Ca no clear trend with increasing conversion was observed, as it was seen for Mönsterås. The behaviour of K was similar, but for P the trend was decreasing. For Cu, there was a similar trend but for Mn a decreasing trend was observed, a slight decreasing trend was observed for Zn, but taking into account the uncertainty in the analysis the trend cannot be regarded as certain. For Al, Na and Si, increasing trend was seen as it was for Mönsterås. It was observed that the amount of ion exchangeables was significantly higher than the one of water solubles indicating that water soluble determination was not enough to determine reactive ash components (Table 3).

Table 2. Chemical fractionation analysis of the biomass samples, mg/kg, Tot.=total, Ione=ionexchangeables, Ws=water solubles, Acid=acid leaching, numbers 1 and 2 indicate duplication analysis.

Wood pellet Glommersträsk										Bark pellet Mönsterås				
	Tot	Ws1	Ws2	Ione	Ione2	Acid1	Acid2	sum 1	sum2	Tot.	Ws	Ione	Acid	sum
Ca	790	190	320	1500	420	33	16	1723	756	8600	440	3400	4300	8140
Mg	180	60	100	110	78	10	10	180	188	710	210	460	27	697
K	480	330	470	130	24	13	10	473	504	2100	1300	560	31	1891
P	20	25	25	20	20	10	10	55	55	400	200	64	110	374
Cu	1.6	0.5	0.5	1	1	1.6	1.6	3.1	3.1	4	0.61	1	2.9	4.51
Mn	110	28	28	78	78	1.3	1.3	107	107	500	92	360	72	524
Zn	12	2.2	2.2	10	10	4.8	4.8	17	17	100	15	32	63	110
Fe	14	0.5	0.5	1	1	13	13	14.5	14.5	470	6.4	1	310	317.4
Al	10	2.1	2.1	1	1	5.6	5.6	8.7	8.7	900	44	7.4	170	221.4
Na	20	10	10	20	20	25	10	55	40	380	97	30	34	161
Cr	0.5	0.5	0.5	1	1	0.5	0.5	2	2	7	0.5	1	2.5	4
Ni	0.5	0.5	0.5	1	1	0.5	0.5	2	2	3.1	0.5	1	1.7	3.2
Si	84	16	16	16	16	5.5	5.5	38	38	4500	47	64	100	211
S	49	15	15	20	20	12	12	47	47	290	46	20	25	91

Pine bark Koirasaari						Pine bark Kattilavesi Uusikaupunki				
	Tot.	Ws	Ione	Acid	sum	Tot.	Ws	Ione	Acid	sum
Ca	2900	77	1400	1300	2777	6100	70	1300	2900	4270
Mg	110	16	72	11	99	160	27	130	10	167
K	330	160	120	25	305	440	280	130	13	423
P	130	38	23	49	110	130	28	20	21	69
Cu	3.7	0.5	1	3.8	5.3	2.8	0.5	1	2.2	3.7
Mn	34	2.5	18	12	32.5	39	2.5	21	9.2	32.7
Zn	26	1.1	3.5	21	25.6	18	0.67	1	11	12.7
Fe	110	0.5	1	85	86.5	56	0.5	1	23	24.5
Al	490	31	6.7	320	357.7	430	95	7.7	140	243
Na	31	16	20	25	61	83	32	20	10	62
Cr	0.79	0.5	1	0.57	2.07	0.86	0.5	1	0.5	2
Ni	0.62	0.5	1	0.65	2.15	0.5	0.5	1	0.5	2
Si	630	10	30	42	82	500	2.8	1	19	22.8
S	270	49	20	37	106	280	17	20	15	52

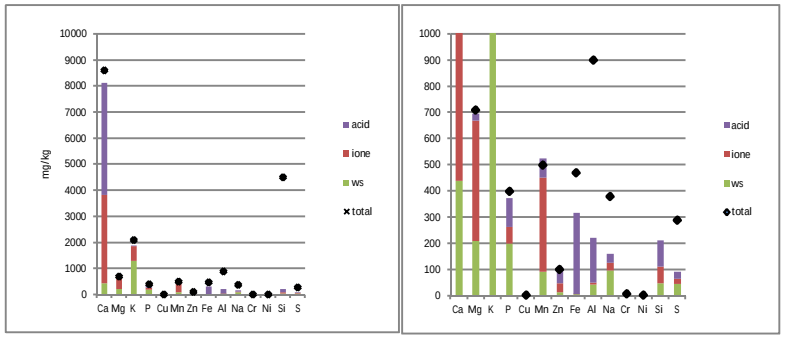

Mönsterås

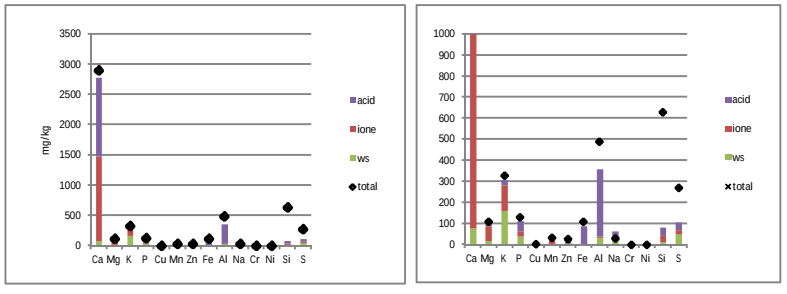

Koirasaari

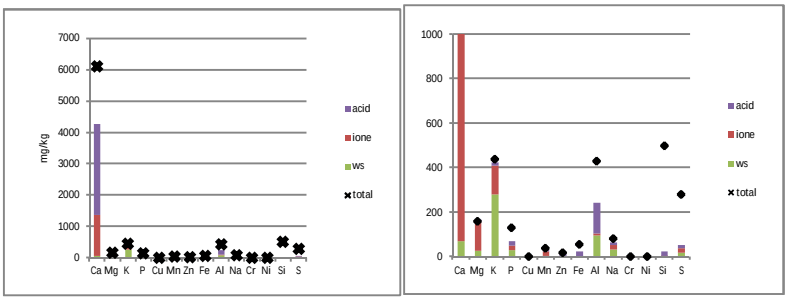

Kattilavesi

Figure 11. Chemical fractionation of the biomass samples in absolute values, the graphs on the right are rescaled for the smaller concentrations (ws=water solubles, ione=ion exchangeables, acid=acid soluble).

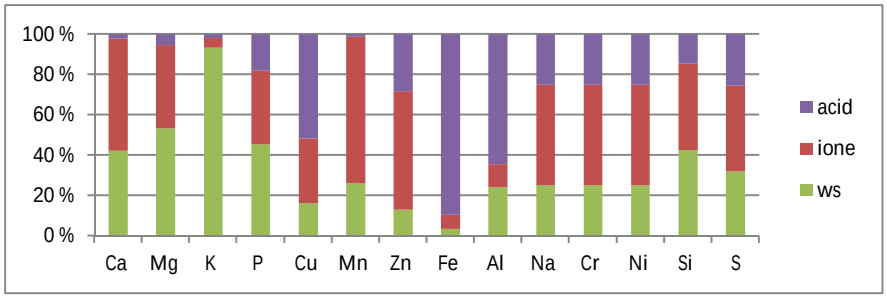

Glommersträsk

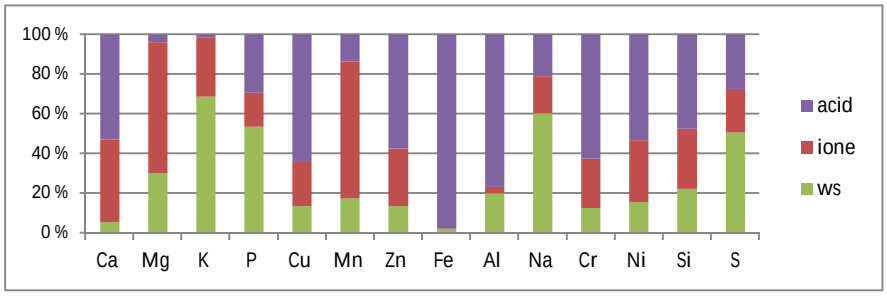

Mönsterås

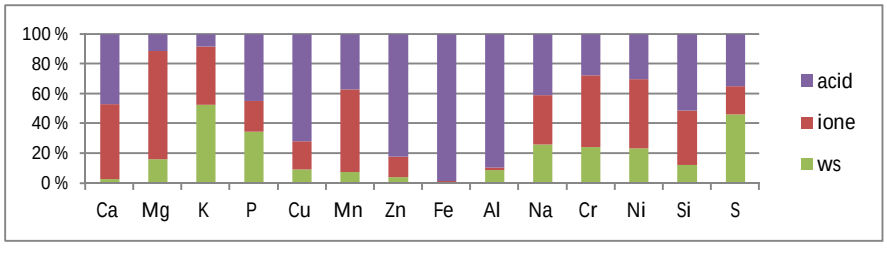

Koirasaari

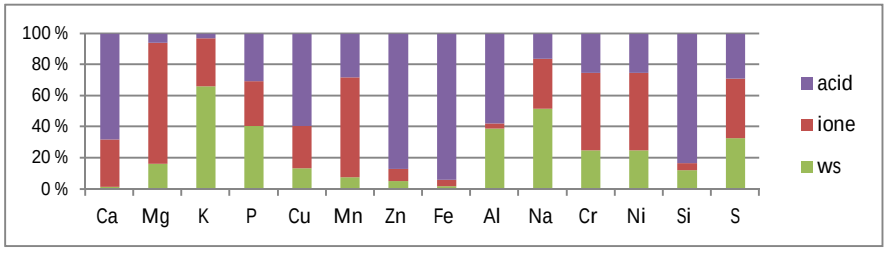

Kattilavesi

Figure 12. Chemical fractionation of the biomass samples as % distributions (ws=watersoluble, ione=ionexchangeable, acid=acid soluble).

Table 3. The share of watersoluble elements in the chars, % of the total in char, gasified to different conversion degrees (t=gasification time, Xt=total fuel conversion, char X=char conversion, ws=watersoluble, ione=ionexchangeable).

	Bark pellet Mönsterås						**Pine bark Koirasaari**			
t, s	60	60	60	150	150	300	60	60	400	800
Xt, %	78	78	79	86	87	95	74	74	87	95
Char X,%	0	0	0	42	42	80	0	0	53	79
	ws	ws	ione	ws	ws	ws	ws	ione	ws	ws
Ca	6.4	15.5	47.8	37.7	63.4	77.2	60.1	107.0	24.4	52.8
Mg	1.0	2.5	30.0	0.5	0.5	0.5	28.0	54.2	14.4	2.1
K	54.6	75.9	45.2	62.0	75.5	64.9	95.4	88.5	67.3	70.0
P	0.4	0.9	8.7	0.3	0.4	0.3	9.9	71.1	8.4	0.7
Cu	34.2	103.2	9.2	28.1	50.4	20.4	98.4	50.7	32.6	21.4
Mn	0.4	0.8	36.9	0.4	0.6	0.5	27.0	67.3	3.4	1.8
Zn	4.4	8.6	16.5	5.3	6.4	4.0	61.5	59.0	59.4	45.7
Fe	0.3	0.7	0.1	0.3	0.4	0.2	2.4	1.0	0.9	0.6
Al	0.9	1.8	0.9	6.2	8.9	9.5	15.1	8.4	29.2	43.1
Na	15.5	22.6	14.2	21.4	27.2	26.5	30.2	50.3	40.4	43.3
Cr	4.0	43.0	1.1	9.3	23.6	13.9	42.8	18.7	50.5	14.8
Ni	2.4	93.8	0.7	7.0	64.4	28.9	32.8	14.3	38.8	7.7
Si	1.2	1.1	0.4	2.6	2.7	3.2	0.8	0.8	1.8	10.9

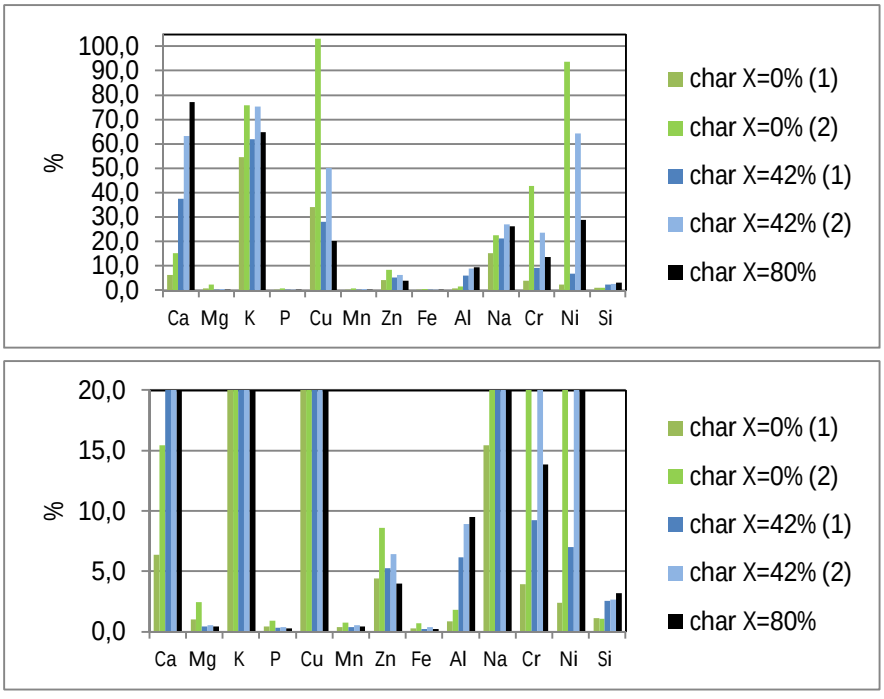

Figure 13. Share of watersolubles in the chars of bark pellet Mönsterås gasified to different conversions in 1 bar steam at 850 °C (the lower graph is rescaled, (1) and (2) indicated duplication analysis).

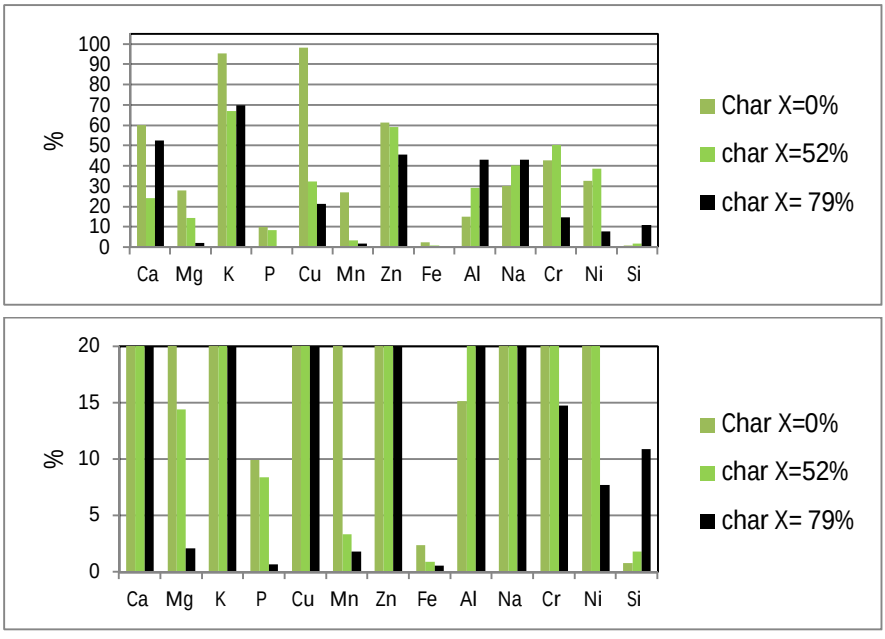

Figure 14. Share of watersolubles in the chars of pine bark Koirasaari gasified to different conversions in 1 bar steam at 850 °C (the lower graph is rescaled).

2.3 SEM

The ash formation as a function of char conversion was studied by microscopy (Scanning electron microscope (SEM) of VTT Expert Services Ltd (Gustafsson, Tom E.)). Details of the ash particles were analysed with energy dispersive X-ray analyse (EDS).

The char samples for SEM was prepared in TG by gasifying the biomass samples either in steam or in CO_2 to certain conversion degrees.

Bark pellet Mönsterås char samples were prepared for SEM analysis by gasifying them in 1 and 20 bar steam at 850 °C. In 1 bar gasification the times were 60, 150 and 330 s when they reached the conversion degrees of 78, 83 and 97% of the total fuel (Xt). These correspond char conversion values (Char X) of 0, 39, 87%, respectively. In 20 bar steam the bark pellet char samples gasified 200s (Xt=92% char X=67%) and 270s (Xt=99.5 and char X = 98%) were also included.

Pine bark Koirasaari samples were prepared for SEM analysis by gasifying them in 1 bar steam at 850 °C 60, 400 and 900s when they reached conversion degrees of 74, 87 and 95% of the total fuel (Xt). These correspond char conversion values of 0, 53 and 81%, respectively. Koirasaari bark sample gasified in 20 bar steam at 850 °C 550s (Xt=99, char X= 97%) was also included.

Char samples of wood pellet Glommersträsk gasified in 10 and 20 bar CO_2 at 850 °C were included in the SEM study. The gasification times were 500 and 700s

in 10 and 20 bar CO_2, respectively, and achieved conversions Xt=93, char X=61% in 10 bar and 94 and 66% in 20 bar, respectively.

The time of 60s was regarded as char conversion zero.

2.4 Results

2.4.1 Bark pellet Mönsterås

In bark pellet Mönsterås char, the ash particles appeared on the char surfaces with gasification reactions had a rectangular or cubic shape. According to the SEM-EDS analysis they consisted of calcium and small amounts of potassium. This indicates the presence of calcium and potassium carbonate. They could also be oxides or hydroxides. The equilibrium calculations carried out in this project (above) the presence of various Ca and K compounds for bark pellet Mönsterås but the rectangular particles only contain Ca (Figure 15) and small amounts K (Figure 17) indicate that they have not reacted to the predicted compounds (Appendix). The sizes of the ash particles such as shown in Figure 18 were less than 10 µm.

The SEM result are presented in Figures 15–21.

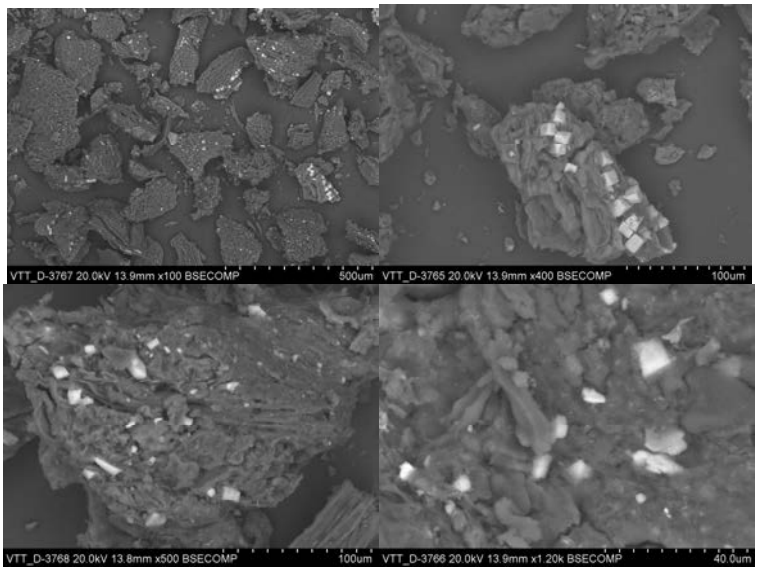

Figure 15. SEM micrographs on bark pellet Mönsterås char, gasified in 1bar H_2O at 850 °C 60s, Xt =78%, char X = 0%.

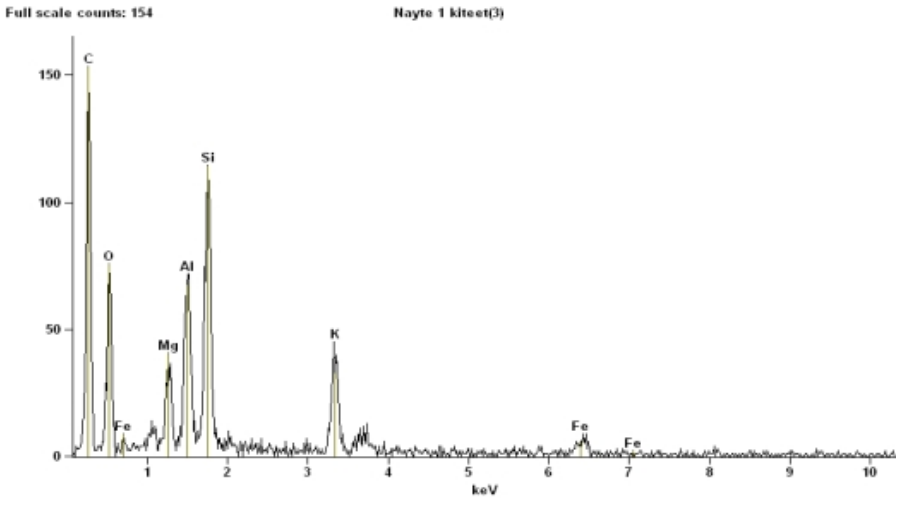

Figure 16. SEM-EDS analysis results on particles presented in Figure 15, mixed particles.

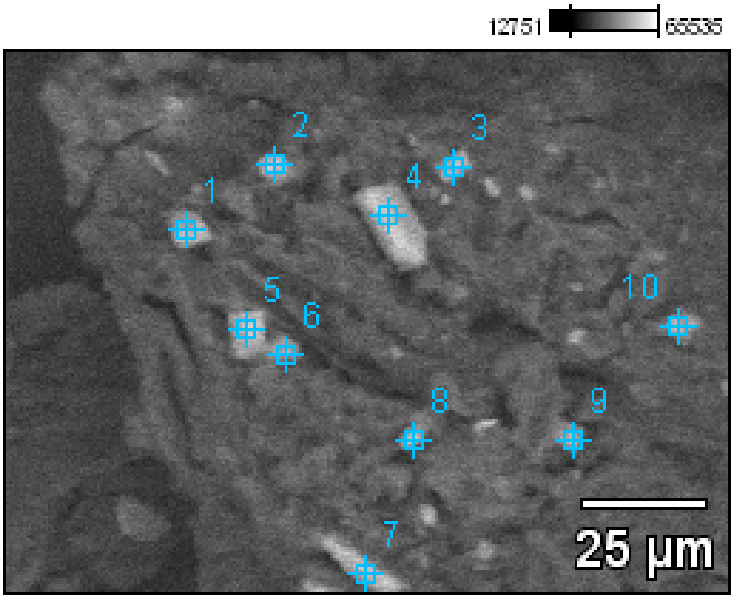

Figure 17. SEM-EDS particle analysis on ash particles in Bark pellet Mönsterås char gasified in 1 bar steam 60s (Xt=78%, char X=0%).

Figure 18. SEM micrographs on bark pellet Mönsterås char gasified 150s (Xt =83%, char X= 39%) in 1 bar steam at 850 °C

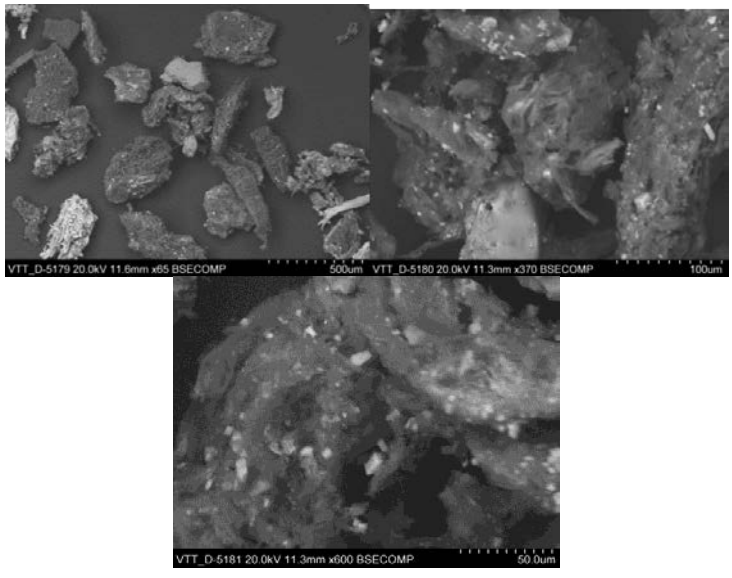

Figure 19. SEM micrographs on bark pellet Mönsterås gasified in 1 bar H_2O 330s (Xt=97% Char X=87%) at 850 °C.

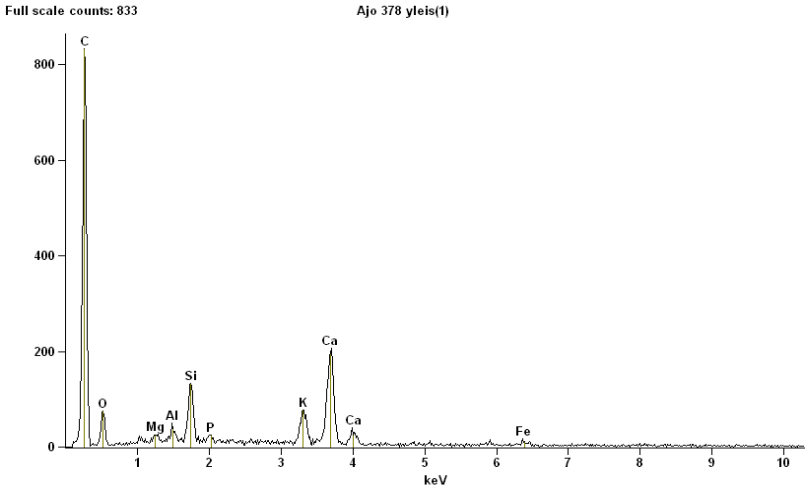

Figure 20. SEM-EDS on Bark pellet Mönsterås char shown in Figure 19.

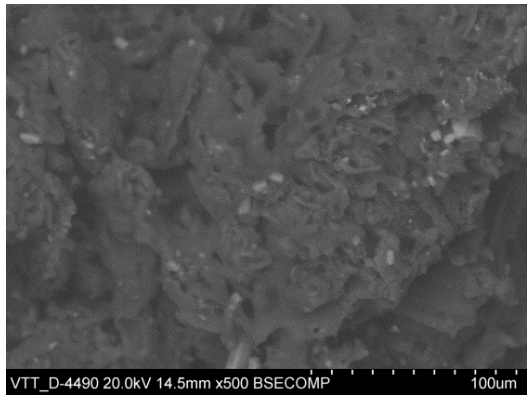

Figure 21. SEM micrograph on bark pellet Mönsterås char gasified in 20 bar H_2O 60s (Xt=77%, char X=0%) at 850 °C.

2.4.2 Pine bark Koirasaari

In pine bark Koirasaari char, the ash particles appeared on char surfaces had rectangular or plate shape. According to the SEM-EDS analysis they consisted mainly of calcium. This indicated the presence of calcium carbonate or oxide or hydroxides. The sizes of the ash particles of the pine bark Koirasaari char (Figure 24) were 20 µm (plate). They can be also in Ca rich agglomerates just after pyrolysis. In the pine bark Koirasaari sample, it can be seen in Figure 26 that the rectangular ash particles may break into small pieces having a size of few micrometers and these may react or mels with other components as shown in Figure 26 (lower).

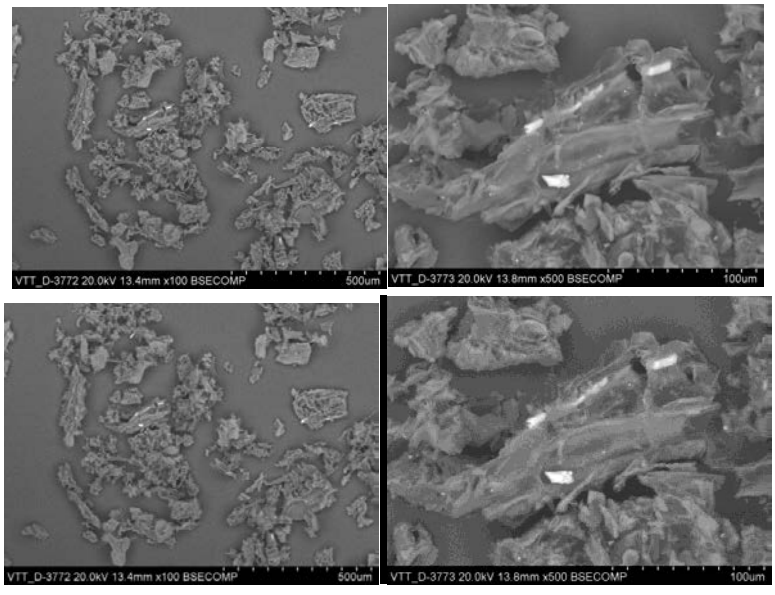

Figure 22. SEM micrograph on pine bark Koirasaari char gasified 60s in 1bar H_2O at 850 °C (Xt = 74%, char X = 0%).

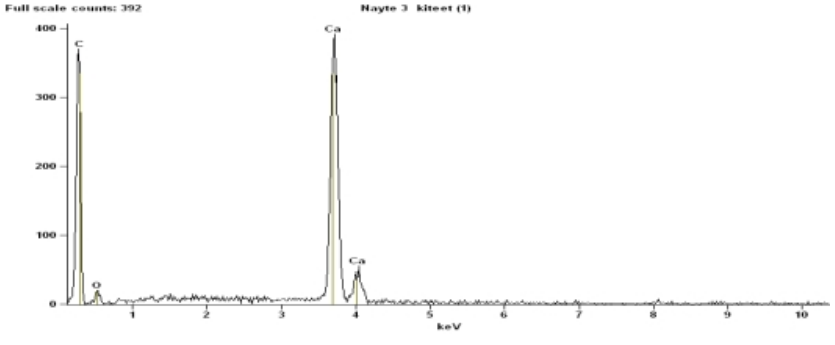

Figure 23. SEM-EDS on ash particles and the carbon matrix of the char shown in Figure 22.

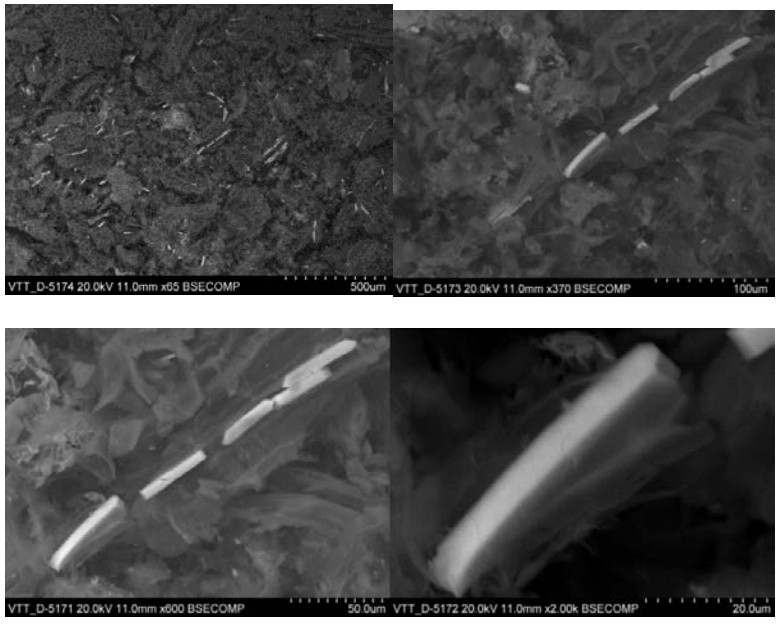

Figure 24. SEM micrographs on pine bark Koirasaari char gasified in 1 bar H_2O 900s at 850 °C (Xt=95%,Char X=81%).

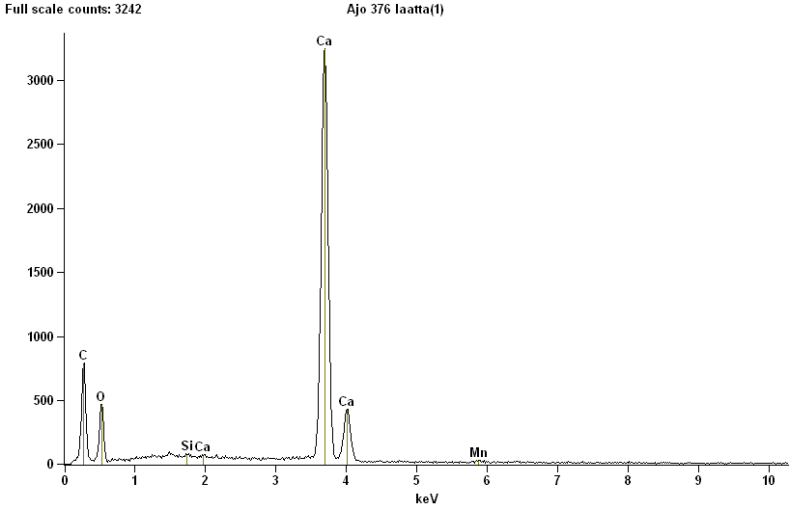

Figure 25. SEM-EDS analysis on the ash particles (plate shape) shown in Figure 24.

Figure 26. SEM micrographs on pine bark Koirasaari char gasified in 20 bar H_2O 550s at 850 °C (Xt=99%,Char X=97%).

2.4.2 Wood pellet Glommersträsk

In wood pellet Glommersträsk, ash particles on char surfaces were round and bubble form particles (size 5–10 µm, Figure 27), which contained calcium and potassium. This indicated the presence of calcium carbonate and potassium carbonates, since the sample was gasified in high CO_2 pressure. At the highest pressure the structures seemed to be a result of melting (Figure 27). According to the elemental composition (Figure 28), it could have been formed an eutectic calcium and potassium carbonate mixture, which has the melting point of 740 °C.

Some nickel and iron rich particles were found in wood pellet char, which were due a contamination caused by the metallic TG sample holder.

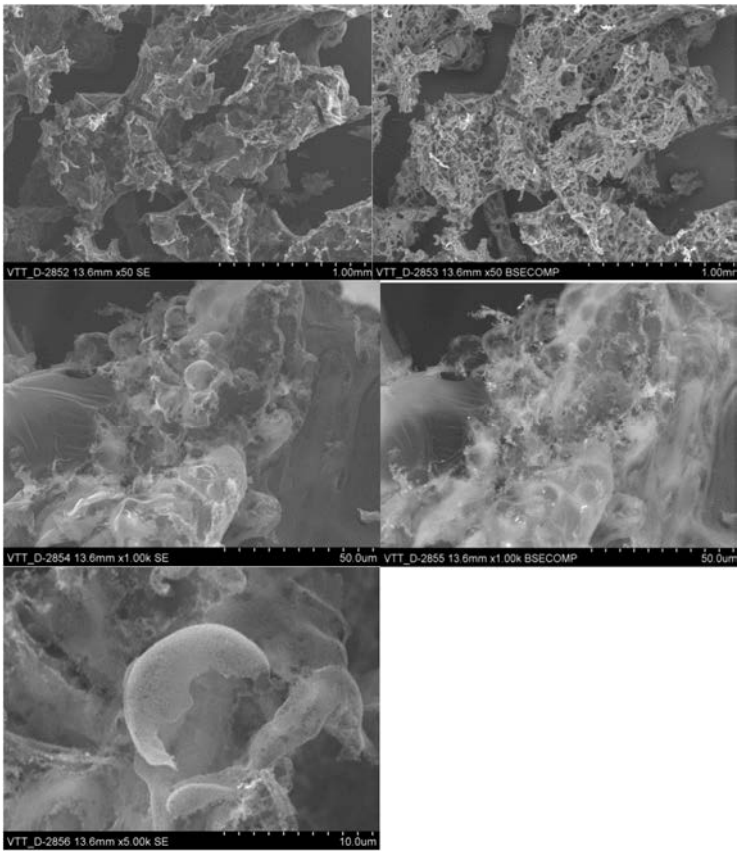

Figure 27. SEM micrograph on wood pellet Glommersträsk char gasified 700s in 20 bar CO_2 at 850 °C, (Xt=94% Char X=66%).

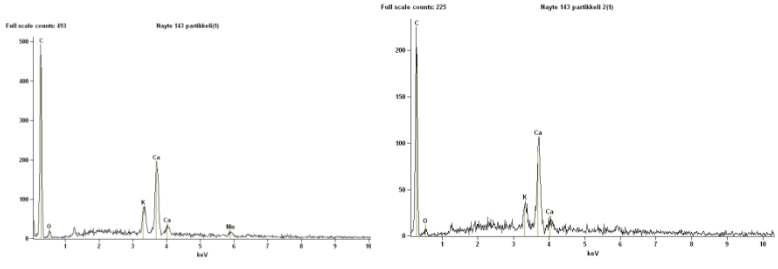

Figure 28. SEM-EDS analysis on the particles shown in Figure 27.

2.5 Fluidised bed tests

Bark pellet Mönsterås was gasified in the atmospheric fluidised bed (AFB) reactor of VTT for studying the behaviour of the ash components in gasification. For the

study hot filter dusts were collected at certain time intervals after the continuous feeding was stopped.

The tests were carried out at 800 °C with 100% steam, and the filtering temperature was 550°C. For the collected filter dust samples were analysed by chemical fractionation. Results are presented in Tables 4 and 5 as well as Figures 29–31.

Table 4. C, H, N and ash content (%) of the hot filter dusts collected in the AFB gasification of bark pellet Mönsterås at different times after the feed was stopped.

	2h	5h
C	67	61
H	0.6	0.6
N	0.2	0.2
Ash	25	-

Table 5. Chemical fractionation of the hot filter dusts collected in the AFB gasification of bark pellet Mönsterås at different times after the feed was stopped, mg/kg d.(ws=water soluble, rest=content of the residue remained after the leaching procedures).

	2h						5h					
	Total	**ws**	**ione**	**acid**	**rest**	**sum**	**total**	**ws**	**ione**	**acid**	**rest**	**sum**
Ca	80800	13500	59100	7800	3600	84000	107500	9400	91200	13600	1100	115300
Mg	6300	20	3700	2200	950	6850	9000	20	6700	2600	390	9690
K	10000	4400	810	1400	4000	10610	7400	3100	470	1300	3500	8370
P	4200	20	440	3400	670	4510	5700	20	530	5600	100	6230
S	400	20	65	65	550	680	180	20	36	52	440	528
Cu	36	1	2	30	13	43	23	1	2	24	4.6	28.6
Mn	4500	1	2900	1500	380	4780	6500	1	4700	2000	180	6880
Zn	420	1	63	300	170	533	260	1.7	50	160	140	351.7
Fe	5700	1	2	4700	1700	6400	4900	1	3.1	4600	1100	5703
Al	7100	32	19	3000	5000	8051	6900	120	16	4000	4500	8636
Na	2500	390	260	250	1700	2600	2300	520	390	220	1500	2630
Cr	490	1	2	86	520	606	170	1	2	30	220	250
Ni	220	1	9.2	200	38	247.2	95	1	11	85	18	114
Si	26600	290	850	2500	22500	26140	22200	490	1300	4500	21400	27690

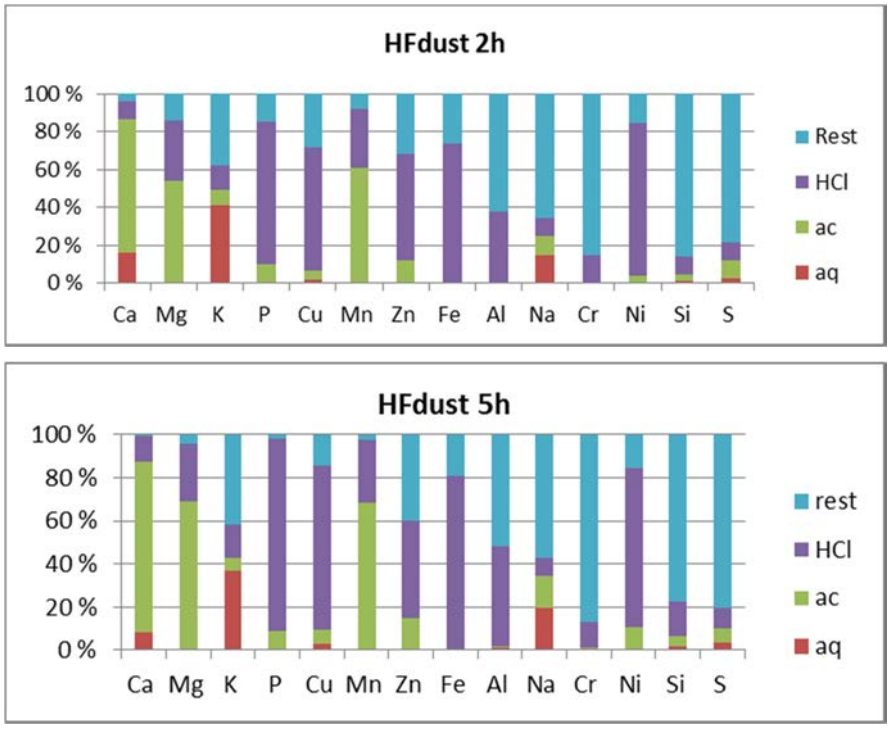

Figure 29. Distribution of the fractions from the chemical fractionation analysis of the hot filter dust ashes of bark pellet Mönsterås collected 2h and 5h after the feed stop (aq=water solubles, ac=ion exchangeables, HCl=acid solubles, rest=residue).

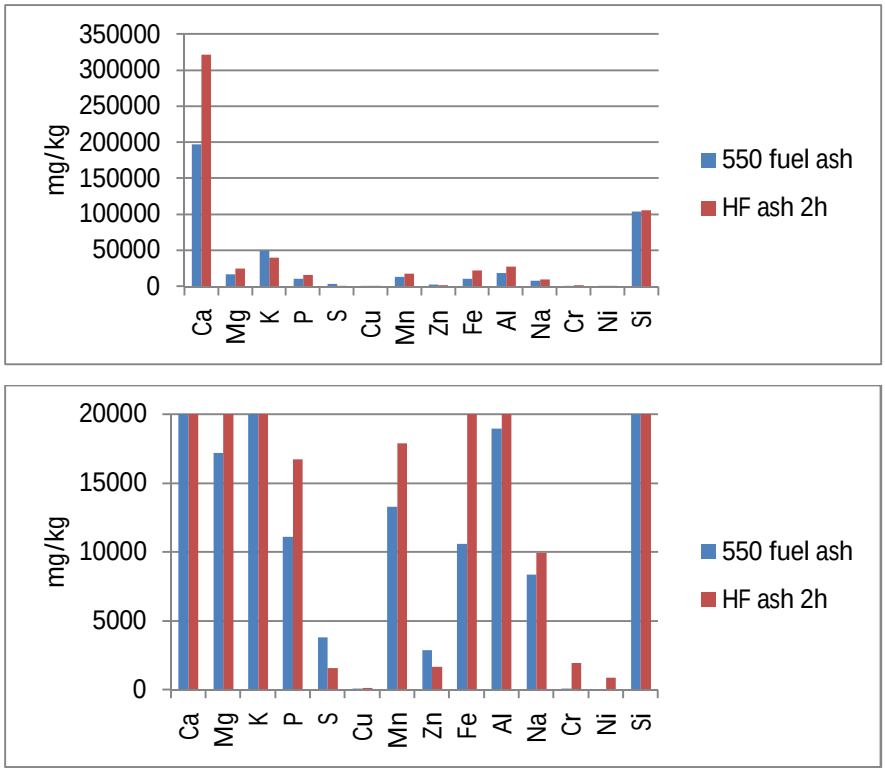

Figure 30. Comparison of chemical compositions of ash and hot filter dust ash of bark pellet Mönsterås collected 2h after the feed stop (lower graph rescaled for the small concentrations).

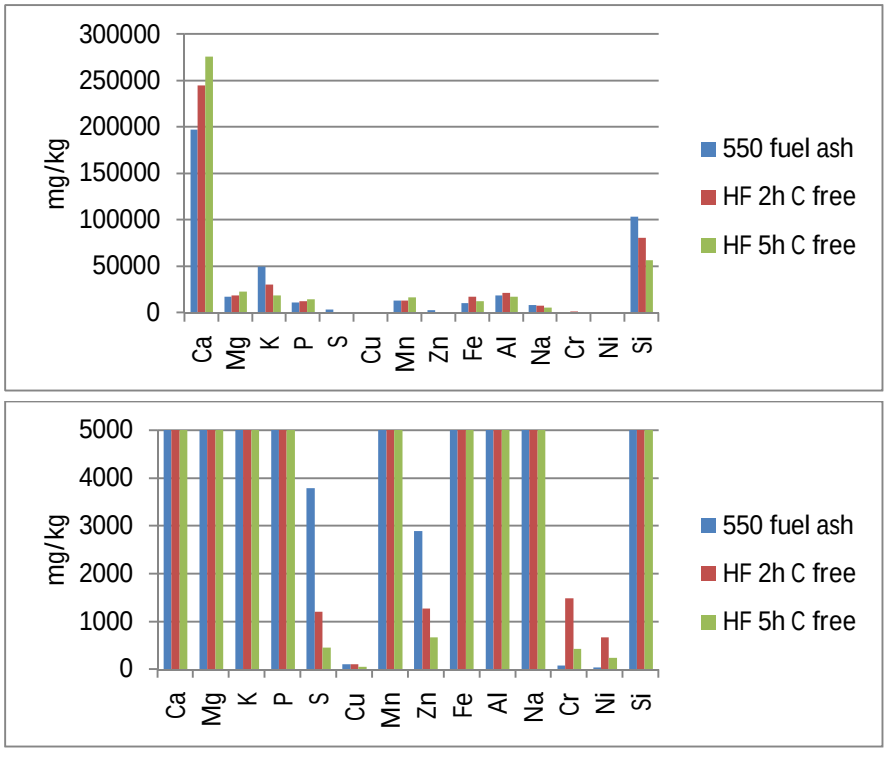

Figure 31. Comparison of chemical compositions of ash and hot filter dust (HF) calculated as carbon free (C free) of bark pellet Mönsterås collected 2 and 5 hours after the feed stop (lower graph rescaled for the small concentrations).

The chemical fractionation gave almost the same result for both of the hot filter ashes (Figure 31). The results showed that Ca, Mg, P, Mn, Fe, Al, Na, Cr and Ni were in higher concentrations in the filter dust than in biomass ash. Fe, Cr, Ni may come from the metal parts of the reactor. But K and Zn, which are regarded as volatile elements, did not show any accumulation in the hot filter dusts. Both of these elements were in large parts in insoluble form (Figure 29).

2.6 Equilibrium calculations

To study more the factors influencing the gasification reactivity, equilibrium calculations were done for the samples used in this project and using a set of 4 biomass samples from USA analysed in another VTT's project. Their ash chemical composition was analysed and possible compounds in different gasification conditions were determined using equilibrium calculations by Rainer Backmann in UMU. The results was published in /5/. The results of the calculations for the sample of this project are in Appendix of this report. If in the calculations, the silicon is not included and salt mixtures are only allowed in the calculations, the re-

sults seem to reflect better the analytical observations, this was especially the case of Glommersträsk wood pellets, were a salt liquid wa formed in addition to the slag liquid. It contains K_2CO_3 with smaller amounts of $CaCO_3$, Na_2CO_3 and K_2S.

2.7 Conclusions

The study of this task aimed at the behaviour of ash forming components like alkali metals and heavy metals in gasification. It contained chemical fractionation of the biomasses and chars, predictions of the ash composition in different parts of a biomass gasifier by means of the thermochemical model. In addition, also partly gasified char samples were studied under SEM (samples prepared in TG). Also some fluidised bed experiments were carried out. The results from the chemical fractionation showed that the bark samples (Mönsterås, pine barks Koirasaari and Kattilavesi) were rather similar deviating from that of wood pellet (Glommersträsk). In the amounts water solubles in char as a function conversion degree, for Mönsterås, the trend was that the share of water soluble calcium increased with conversion degree, but potassium seemed to be quite constant, for Mg and P no trend was seen and for Cu the trend seemed to be decreasing and the share of the water soluble copper could be quite high. For Mn and Zn the shares of water solubles were small, and no trend with conversion was observed. For Al, Na and Si an increasing trend was seen. Ni, Cr and Fe results were not relevant in the char analysis because of the contamination of these elements from the TG's sample holder. Pine bark Koirasaari had a different pattern in its watersolubles than Mönsterås. The levels of watersolubles in general were somewhat higher than those of Mönsterås.

The ash particles in the partly gasified char samples appeared in rectangular or cubic shapes. They consisted of calcium and potassium, most probably due to the presence of calcium and potassium carbonate. In wood pellet Glommersträsk, ash particles on char surfaces (from CO_2 gasification) were round and bubble form containing calcium and potassium. The bubble form indicated the presence of molten calcium and potassium carbonates, since the sample was gasified in high CO_2 pressure at 850 °C and melting could be due the eutectic of calcium and potassium carbonate mixture, which has the melting point of 740 °C.

According to the comparison of the equilibrium calculations and the measured ash characteristics if the silicon is not included and the results seem to reflect better the analytical observations. But no clear verification of the equilibrium results could not be seen in all cases.

Due to the uncertainties in the CF analysis, some of the results may not be reliable.

References

1. Moilanen, A. Thermogravimetric characterisations of biomass and waste for gasification processes. VTT Publications 607. Academic Dissertation Åbo Akademi. VTT, Espoo 2006. 103 p. + app. 97 p. http://www.vtt.fi/inf/pdf/publications/2006/P607.pdf

2. Moilanen, A., Nasrullah, M. Gasification reactivity and ash sintering behaviour of biomass feedstocks. VTT Publications 769. VTT, Espoo 2011. 39 p. + app. 96 p. http://www.vtt.fi/inf/pdf/publications/2011/P769.pdf

3. Cetin, E., Moghtaderi, B., Gupta, R., Wall, T.F. Biomass gasification kinetics: influences of pressure and char structure. Combust. Sci. and Tech. 177 (2005) 765–791.

4. Umeki, K., Moilanen, A., Alberto Gómez-Barea, A., Konttinen, J. A model of biomass char gasification describing the change in catalytic activity of ash. Chemical Engineering Journal 207–208 (2012) 616–624.

5. Moilanen, A., Backman, R., Umeki, K., Lehtinen, J., Hannula, I. Understanding gasification reactivity behaviour of four biomass samples from USA based on modelling and thermodynamic equilibrium calculations of ash components. CSChE2013 (63rd Canadian Chemical Engineering Conference) Fredericton, New Brunswick, Canada, October 20 to 23, 2013.

6. Moilanen, A., Wang, L., Lehtinen, J., Muhola, M. Comparison of TG for gasification reactivity of biomass chars. To be published 2015.

Chapter 2

Studies on entrained-flow gasification of black liquor and woody biomass

Henrik Wiinikka and Per Carlsson, ETC Energy Technology Centre, Sweden
Kentaro Umeki, Luleå University of Technology, Sweden

Contents

Studies on entrained-flow gasification of black liquor and woody biomass

1. Experimental and numerical simulations of black liquor gasification

1.1 Introduction

Since 2005 the technology vendor Chemrec has been operating a pressurized entrained flow high temperature black liquor gasification plant named DP-1. The plant, which now have an accumulated operating time of approximately 12 000 h, is adjacent to the Smurfit Kappa Kraftliner pulp and paper mill in Piteå, Sweden. Just recent, a catalytic plant was commissioned in conjunction with the gasification plant to produce Di-Methyl Ether (DME) which is a gaseous diesel substitute from the syngas produced by the gasification process. The DP-1 black liquor gasification plant is described schematically in Figure 1. The main parts are the refractory lined 3 MWth oxygen blown gasification reactor, the quench and the gas cooler. In the reactor, preheated (~140 °C) black liquor is injected through a centrally placed spray burner nozzle at the top of the gasifier, together with oxygen and a small portion of nitrogen (about 20 % of the oxygen mass flow rate). At elevated pressure (typical operating pressure ~27 bar (g)) and a temperature of about 1000 °C the black liquor is gasified to form H_2O, CO_2, CO, H_2, H_2S and CH_4 and a liquid ash. The ash in the black liquor which makes up approximately 30 % of the virgin fuel melts due to the high temperature in the gasification reactor and is commonly referred to as smelt. The smelt consists of inorganic cooking chemicals used in the pulp process and needs to be recovered. This recovery begins in the quench located downstream, directly underneath the gasification reactor. Here, the gas and the smelt are rapidly cooled by water spray nozzles and separated so that the smelt is dissolved in water in the bottom of the quench. This smelt water mixture is referred to as green liquor which may be returned to the pulp mill for further recovery treatment. Downstream the quench is the gas cooler, which is design to condense the water vapor in gas and at the same time remove carry-over particulates and condensable hydrocarbons that were not trapped in the quench. To remove the sulphur components in the syngas (mainly H_2S) both a common sulphur re-

moval technique and a novel method based on short time contactors have been used.

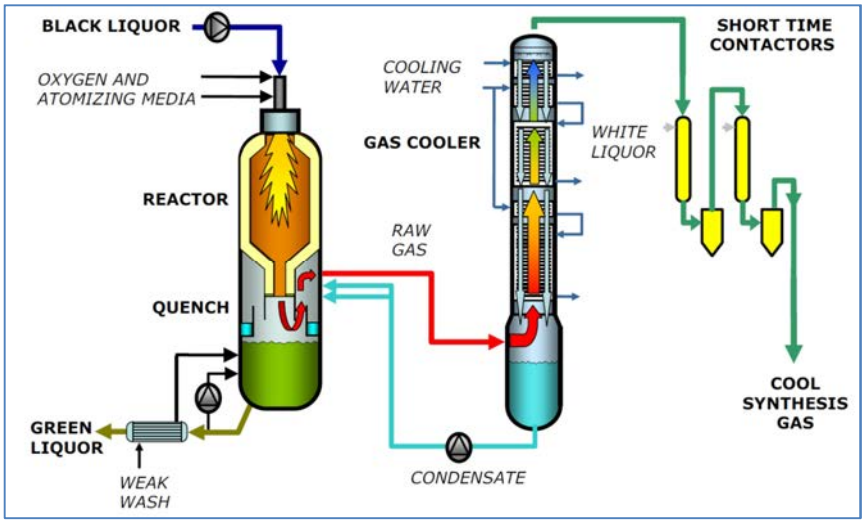

Figure 1. Schematic drawing of the main components making up the entrained flow black liquor gasifier.

In previous work gas samples were withdrawn from the hot gasification reactor using a water cooled sampling probe (Carlsson et al. 2010a). During the experimental campaign several operating conditions, such as temperature, residence time and pressure were varied. Furthermore, in a recent study (Carlsson et al. 2010b) these experimental results were compared to Computational Fluid Dynamics (CFD) predictions when the oxygen to black liquor equivalence ratio was varied. The results showed that methane could not be predicted at the outlet of the gasifier. The experiments showed a methane concentration ranging from 0.5% mol to about 2.5% mol whilst the model predicted 0%. In order to resolve (and investigate the influence of) this, CH_4 concentration had to be prescribed (by treating part of the CH_4 as inert) in order to get reasonable predictions for the main gas components. In this work the oxidation and reforming of methane is further explored. The global reaction mechanism used in the previous work is compared to a more comprehensive reaction mechanism in 1-D plug flow reactor simulations. Then, the influence of the pyrolysis gas composition on the gasifier outlet composition is evaluated using CFD. Finally the results from the updated CFD model are compared to experimental results where pressure, oxygen to black liquor equivalence ratio (from here on equivalence ratio) and residence time have been varied. The main goal has been to make the CFD reactor model less dependent of prescribed model parameters (prescribed methane concentration) and improve the predictions for a wider range of operating conditions while maintaining numerical stability and simplicity.

1.2 Experimental

The DP-1 gasification is approximately 2.3 meters in height and 0.6 meters in diameter. During the experimental campaign gas samples were collected in the lower part of the gasification reactor approximately 0.6 m above the outlet. The samples were obtained using a specially design water-cooled quench probe. The collected gas samples were analyzed with respect to CH_4, CO, CO_2, H_2, N_2, H_2S, COS, and O_2/Ar using a Varian CP-3800 gas chromatograph. During the experimental campaign several different process parameters were varied (see Table 1) this variation resulted in variations in operating conditions (pressure, temperature and residence time). The gasifier is typically operated at a pressure of 27 bar(g) at a temperature of about 1000 °C which for the liquor composition (showed in Table 2) used in the experiments corresponded to a oxygen to black liquor equivalence ratio (defined as $\lambda=(x_{O2}/x_{fuel})/(x_{O2,stoich}/x_{fuel,stoich})$, where x is mol fraction) of 0.434. As can be seen in Table 1 this base operating condition can found in the high pressure case (+P) and in the medium temperature case (0λ). The normalized gas residence time showed in Table 1 is based on a plug flow assumption, with the base operating conditions set to unity. In this case, high pressure in combination with low mass flow rates results in a long gas residence time and vice versa.

Table 1. Process parameters during the experimental campaign.

CAMPAIGN		Variations in pressure			Variations in temperature			Variations in residence time		
Variable	Unit	-P	0P	+P	-λ	0λ	+λ	-τ	0τ	+τ
Pressure	bar(g)	15	20	27	27	27	27	20	20	20
Black liquor mass flow rate	kg/h	487	645	870	870	870	870	1000	870	485
Black liquor pre-heat temperature	°C	140	140	140	140	140	140	140	140	140
O_2 mass flow rate	kg/h	151	196	254	232	254	265	295	257	144
N_2 mass flow rate	kg/h	47	47	47	47	47	47	47	47	47
O_2 / BL	-	0.310	0.304	0.292	0.267	0.292	0.305	0.295	0.295	0.297
λ	-	0.460	0.451	0.434	0.396	0.434	0.452	0.438	0.439	0.441
Normalized gas residence time	-	0.95	0.98	1	1.02	1	0.99	0.65	0.74	1.28

Table 2. Black liquor ultimate analysis used in the experiments.

ULTIMATE ANALYSIS (dry solids)	*%wt*	Relative uncertainty %	
C	31.3	2.0	
H	3.4	6.0	
O*	37.2	9.1	**
N	0.1	20.0	
S	5.6	13.0	
Na	20.1	8.0	
K	2.3	8.0	
Cl	0.1	13.0	
PROXIMATE ANALYSIS			
Moisture	24.8	2.0	
Volatiles	N/A		
Fixed carbon	N/A		
HHV MJ/kg	12.57	1.6	

** by difference, ** by difference from uncertainties in participating elements using extremes*

1.3 Numerical

1.3.1 The CFD model

The current CFD model and its material description have been extensively discussed by Marklund et al. (2008) and Carlsson et al. (2010b) and will therefore only be summarized here.

The reactor geometry was modeled as a 2D slice using periodic azimutal boundary conditions based on rotational symmetry. The wall heat losses were set to 90 kW evenly distributed along the refractory wall, based on previous estimates. The burner was modeled as a simplified spray burner with concentrical annular inlets where oxygen and discrete black liquor droplets enter the gasifier at a prescribed range of angles and velocities. The two-phase flow consisting of dispersed black liquor particles and gases were modeled using the Euler – Lagrange formulation. The black liquor spray was represented by 1003 discrete particles having a fitted Rosin Rammler distribution of power 2 and a characteristic size of 200 µm. Turbulence was modeled with the k-ε model using scalable wall functions together with a turbulent dispersion model to introduce turbulence effects on the black liquor particles. Radiative heat transfer was modeled using the Discrete Transfer radiation model by Lockwood and Shah (1981) treating the wall as optically smooth with a radiative emissivity of 0.5. The absorption coefficient for the gas was calculated as the mass weight average of the participating species. To ensure consistency between the experimental and modeled heating value, heat of reaction for pyrolysis in the model was taken as the difference between the modeled and experimental heating value. Drying, pyrolysis, char gasification and smelt

formation reactions were modeled as showed in Table 3 using the reaction mechanisms and coefficients described by Marklund (2006). The model was implemented in the commercial CFD software package Ansys CFX where the multiphase reactions were implemented in user defined FORTRAN subroutines.

Table 3. Reactions considered in the CFD-model, R: homogeneous reactions. MR: Heterogeneous reactions. The Jones mechanism is reaction R1-R4 the combustion mechanism is reaction R1, R3, R4 and R5.

	REACTION
R1	$CH_4 + ½O_2 \rightarrow CO + 2H_2$
R2	$CH_4 + H_2O \rightarrow CO + 3H_2$
R3	$H_2 + ½O_2 \rightarrow H_2O$
R4	$CO + H_2O \leftrightarrow CO_2 + H_2$
R5	$CO + O_2 \leftrightarrow CO_2$
MR1	$H_2O\ (l) \rightarrow H_2O\ (g)$
MR2	$Volatiles \rightarrow aH_2S+bCO+cCO_2+dH_2+eCH_4$ *
MR3	$C + H_2O \rightarrow CO+H_2$
MR4	$C + CO_2 \rightarrow 2CO$
MR5	$C + ½Na_2SO_4 \rightarrow ½Na_2S + CO_2$

**Coefficients a → e molar fractions derived from Tab. III, heat of reaction taken as the difference between the experimental and modeled heating value.*

1.3.2 PFR calculation

In order to select an appropriate gas phase reaction mechanism for the CFD model calculations where performed in the chemical kinetics program Cantera where GRI-Mech 3.0 was used as a reference mechanism. The mechanisms considered for the CFD model are the 4 step, 6 species global reaction mechanism developed by Jones and Lindstedt (1988). Reaction R1 to R4 showed in Table 3 is the Jones and Lindstedt mechanism and the kinetics used in the CFD model was also taken from the paper by Jones and Lindstedt. The oxidation mechanism is a combination of reaction R1 to R5 but omitting the steam methane reforming reaction (SMR, R2). In this case the kinetics where taken from Westbrook and Dryer (1981) for reaction R1 and R5 and from Jones and Lindstedt (1988) for reaction R3 and R4. The Jones and Lindstedts mechanism was compared to GRI-Mech (with respect to methane conversion) in Plug Flow Reactor (PFR) calculations performed at isothermal conditions with the following inlet molar gas composition: CH_4: 10%, CO_2: 20% CO: 20%, H_2O: 25%, H_2: 25%. The pressure was set to 27 bar(g) and the temperatures to: 1273, 1400 and 1650 K.

1.3.3 Influence from variation in CO/CO_2 and reaction mechanisms

The black liquor ultimate analysis was simplified and converted into species using the assumptions in Marklund et al. (2008) and the method described in Carlsson et al. (2010b). The resulting proximate analysis and species distribution can been seen in Table 4. The assumed CO/CO_2 molar ratio of the pyrolysis gas and fixed/gas carbon ratio is worth a special mentioning. As can be seen in Figure 2 both ratios influence the amount of methane that is released during pyrolysis. Consequently, this will have an effect on how much methane that appears in the syngas coming out from the reactor. The influence of this was investigated with CFD by calculating the outlet gas composition using three different CO/CO_2 ratios, 1, 8 and 16 (Table 4). The reaction mechanisms used in the calculations were the Jones et al. with an extinction temperatures (forces reaction rate to zero if temperature is below the preset value) set to 1273 and 1400 K on the steam methane reforming reaction (R2), and the oxidation mechanism described above. The results from these calculations where then compared to the experimental values for the base operating condition (0λ, see Table 1).

Table 4. Simplified ultimate analysis and proximate analysis used in the calculations.

SIMPLIFIED ULTIMATE ANALYSIS		*%wt*		
C		31.30		
H		3.40		
O		37.34		
N		0.00		
S		5.60		
Na		22.36		
K		0.00		
Cl		0.00		
PROXIMATE ANALYSIS	*Specie*	*CO/CO_2 mol ratio*		
		1	*8*	*16*
Moisture %wt	$H_2O(l)$	24.80	24.80	24.80
Volatiles %wt	$H_2S(g)$	1.51	1.51	1.51
	$CO(g)$	5.86	14.06	15.62
	$CO_2(g)$	9.20	2.76	1.53
	$H_2(g)$	1.22	1.81	1.92
	$CH_4(g)$	4.83	2.48	2.03
Fixed carbon %wt	$C(s)$	11.77	11.77	11.77
Ash %wt	$Na_2SO_4(l)$	11.00	11.00	11.00
	$Na_2S(l)$	0.76	0.76	0.76
	$Na_2CO_3(l)$	27.64	27.64	27.64
	$NaOH(l)$	1.42	1.42	1.42
HHV MJ/kg		12.60	13.08	13.18

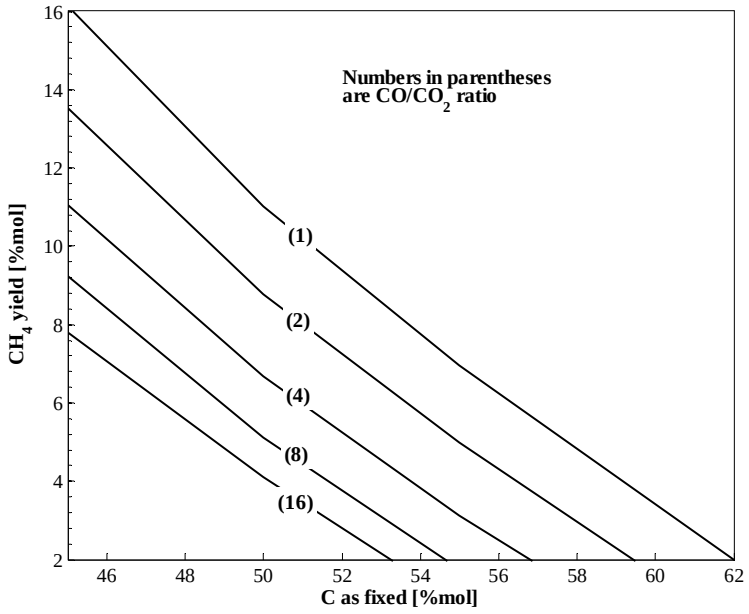

Figure 2. Influence from assumed CO/CO_2 and fixed carbon ratio on CH_4 yield during pyrolysis. CH_4 yield defined as the mol fraction of methane released during pyrolysis relative 1 mol of dry black liquor. The CO/ CO_2 ratio is constant along each line and marked with actual values in parentheses.

1.3.4 Influence from variations in process conditions

When the process conditions were varied the CO/CO_2 was set to unity and the carbon char/gas ratio to 50 %. The boundary conditions used in the CFD simulations were taken as the process values obtained from the DP-1 process monitoring system showed in Table 1. The Jones mechanism with the addition of an extinction temperature set to 1400 K on the steam methane reforming reaction was used as the homogeneous reaction mechanism. The Jones mechanism was implemented in CFD code where the water gas co-shift reaction (R4) was modeled using the Finite Rate Chemistry model (FRC) and the irreversible reactions using the combined eddy dissipation/FRC-model. Currently, the CFD model does not include a reaction mechanism for H_2S; instead it is treated as an inert. The concentration of H_2S at the outlet will be decided by the pyrolysis gas composition showed in Table 3 and to some extent dilution.

1.4 Results

1.4.1 PFR calculations

The PFR calculations were done in order to simulate regions in the gasification reactor where the temperature is still relatively high but all oxygen is depleted. The inlet gas composition was set to a typical syngas composition and the effects of temperature were investigated. In Figure 3 the evolution of methane is showed as function of residence time in an isothermal plug flow reactor and a total residence time of 5 s. For the GRI mechanism, methane starts to reform at about 1400 K were only 5% have been turned into other species (mainly CO and H_2). At 1550 K (not showed), about 60% have been reformed and at the highest temperature, 1650 K, almost all methane is reformed. The Jones mechanism shows a significantly higher reformation rate. At 1400 K, about 85 % of the methane has been reformed, which should be compared to 5% for GRI-Mech. The conversion of the methane has an immediate affect on the major gas components as can be seen in Figure 4. The results also show that the water gas CO shift reaction (R4) is significantly faster in the Jones and Lindstedt (1988) mechanism than the reactions determining the major gas components in GRI-Mech. However, for the highest temperature (1650 K) the agreement is much better both for methane prediction and for the main gas components. The pure oxidation mechanism does not include the reformation of methane and is therefore not showed.

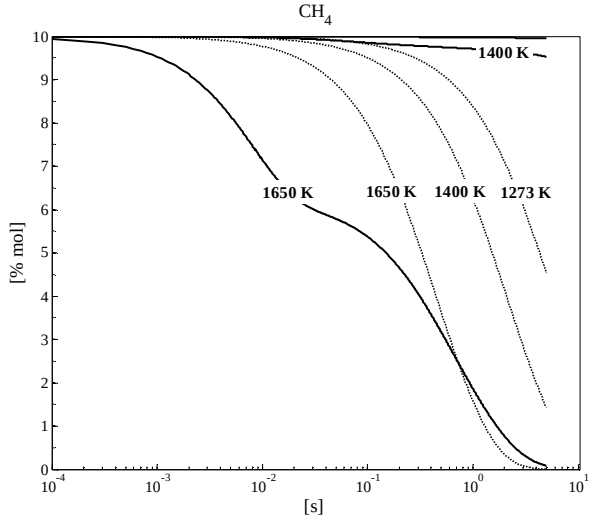

Figure 3. Profiles of CH_4 molar fraction vs. residence time at different temperatures in an isothermal plug flow reactor at 27 bar. Solid line: GRI-Mech. Dotted Line: Jones et al. The inlet molar gas composition was CH_4: 10%, CO_2: 20% CO: 20%, H_2O: 25%, H_2: 25%. The reactor temperatures were: 1273, 1400, and 1650 K for each respective case. Temperature is constant along each curve.

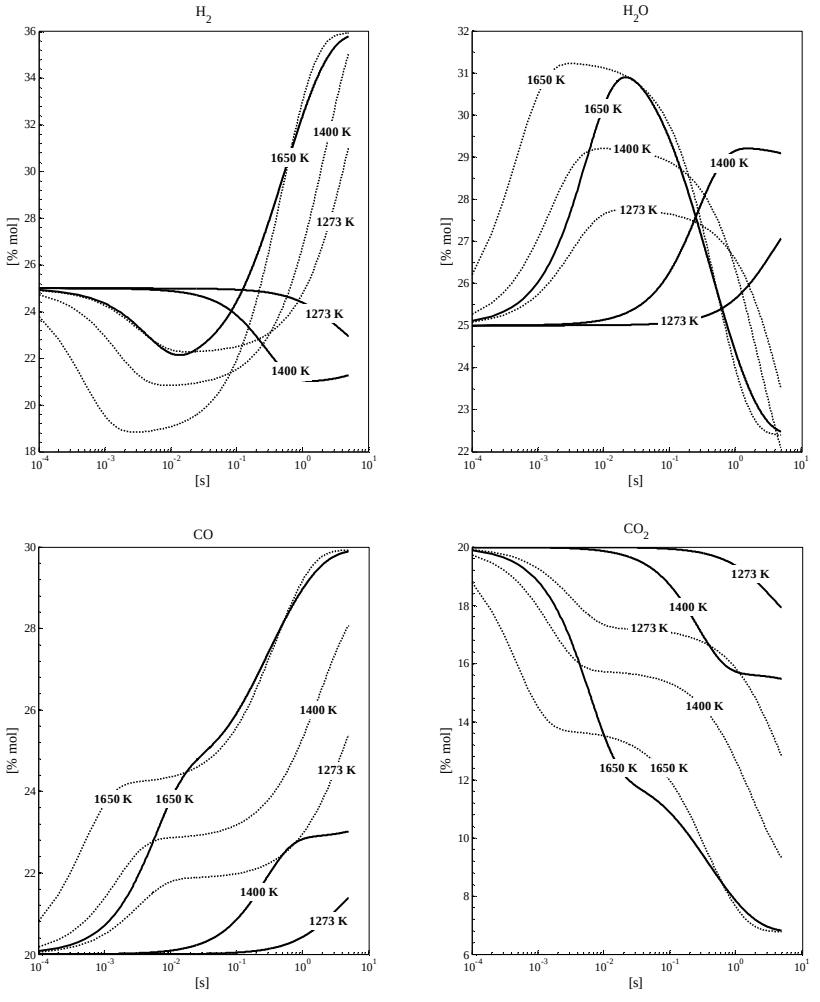

Figure 4. Profiles of H_2, H_2O, CO and CO_2 molar fraction vs. residence time (logarithmic scale) at different temperatures in an isothermal plug flow reactor at 27 bar (g). Solid line: GRI-Mech. Dotted Line: Jones et al. The inlet molar gas composition was CH_4: 10%, CO_2: 20% CO: 20%, H_2O: 25%, H_2: 25%. The reactor temperatures were: 1273, 1400, and 1650 K for each respective case. Temperature is constant along each curve.

1.4.2 Influence from variations in CO/CO_2 and reaction mechanisms

The reaction mechanisms were further investigated using CFD and the results are presented in Table 5. As can be seen in Table 5, there is a significant difference in the outlet methane concentration, ranging from 0 % mol to just above 5% mol depending on the CO/CO_2 ratio and the reaction mechanism. The values should

be compared to the experimentally obtained value of 1.40% mol on dry nitrogen free basis. The Jones mechanism with extinction temperature set to 1400 K and a CO/CO_2 ratio of 1 give similar predictions as the pure oxidation mechanism with the CO/CO_2 ratio set to 16. For the Jones mechanism, about 90 % of the methane (released during pyrolysis) is reformed and oxidized to main components. For the oxidation mechanism this value is about 60 %. Even thou the two reaction mechanism perform similar (be it though at different CO/CO_2 ratios) the Jones model with the SMR extinction temperature set to 1400 K and a CO/CO_2 ratio set to unity was used in the CFD calculation when process conditions were varied.

Table 5. Experimental and numerical results (CFD), units are % mol and MJ/kg. Influence from CO/CO_2 ratio and reaction mechanism on outlet gas composition. Mechanisms are the Jones and Lindstedt with extinction temperature set to 1273 K and 1400 K on the steam methane reforming reaction (R2 in Table 4) and the oxidation mechanism (R1, R3, R4, R5).

		CO_2		CO		H_2	
		34.3 ± 0.3 %		28.5 ± 0.2 %		34.1 ± 0.2 %	
MECHANISM	CO/CO_2	Num.	Rel. error	Num.	Rel. error	Num.	Rel. error
Jones and Lindstedt	1	31.5%	-8.8%	30.6%	6.9%	36.2%	5.8%
SMR exti. temp 1273 K	8	33.8%	-1.4%	28.2%	-1.1%	36.2%	5.9%
Jones and Lindstedt	1	35.1%	2.3%	27.2%	-4.9%	34.8%	2.2%
SMR exti. temp 1400 K	8	34.5%	0.5%	27.9%	-2.4%	35.4%	3.7%
Oxidation of CH_4 CO	1	39.1%	12.2%	25.3%	-13.0%	28.7%	-18.8%
and H_2 with water gas	8	37.2%	7.7%	25.5%	-11.8%	33.2%	-2.5%
shift	16	35.5%	3.2%	27.2%	-5.0%	33.8%	-0.8%

		CH_4		H_2S		LHV	
		1.40 ± 0.07 %		1.64 ± 0.04 %		7.31 MJ/Kg	
MECHANISM	CO/CO_2	Num.	Rel. error	Num.	Rel. error	Num.	Rel. error
Jones and Lindstedt	1	0.00%	-	1.63%	-0.6%	7.80	6.3%
SMR exti. temp 1273 K	8	7.12%	-	1.69%	2.8%	7.34	0.4%
Jones and Lindstedt	1	1.15%	-22.4%	1.71%	3.9%	7.31	0.0%
SMR exti. temp 1400 K	8	5.48%	-156.1%	1.71%	4.1%	7.30	-0.1%
Oxidation of CH_4 CO	1	5.15%	72.8%	1.83%	10.2%	7.29	-0.3%
and H_2 with water gas	8	2.27%	38.3%	1.76%	6.8%	7.16	-2.1%
shift	16	1.81%	22.6%	1.72%	4.6%	7.36	0.7%

1.4.3 Influence from variations in process conditions

The results from the process conditions variation are showed in Table 6 (with relative error, as number) and Figure 5 (showing trends in graphs). Starting with the pressure variation experiments, the prediction for the main gas components

are within a relative error of approximately 5 %. However, the trends are not predicted for CO and CO_2. The experimentally obtained values show a clear decrease in CO_2 when pressure is increased, for CO the trend is the opposite an increase when the pressure is increased and this is not captured by the model. The trend in CH_4 also shows that the middle pressure point (0P 20 bar (g)) is the operating condition that deviate from the trend. The relative error in CH_4 is similar for the low and high pressure case but is about two times as large for the medium pressure case which to some degree may explains the deviation for CO and CO_2. The trend in H_2 concentration is predicted i.e. an increase in concentration with an increase of pressure. H_2S show the second largest relative error at about 25 %. H_2S is treated as an inert in the model and hence will not be influenced by operating conditions. The outlet concentration is instead dictated by the initial release of H_2S (Table 3) and to some extent dilution effects. The char conversion and temperature is the highest at the medium pressure point at 98.8 % and about 1245 K at the outlet respectively (Figure 6).

Table 6. Experimental and numerical results (CFD), units are % mol and MJ/kg. Boundary conditions are according to Table 1.

		CO_2 STD ±0.3			CO STD ±0.2			H_2 STD ±0.2		
CAMPAIGN	Case	Exp.	Num.	Rel. error	Exp.	Num.	Rel. error	Exp.	Num.	Rel. error
Variations in pressure	-P	37.1	36.1	-2.7%	27.4	28.6	4.2%	33.0	32.7	-0.8%
	0P	35.5	34.5	-2.8%	28.4	29.3	3.1%	33.3	33.7	1.3%
	+P	34.0	35.1	3.3%	28.7	27.2	-5.3%	34.2	34.8	1.8%
Variations in temperature	-λ	34.1	34.7	1.8%	25.6	26.2	2.4%	35.6	35.5	-0.2%
	0λ	34.3	35.1	2.3%	28.5	27.2	-4.7%	34.1	34.8	2.2%
	+λ	34.8	34.5	-1.0%	29.5	29.1	-1.3%	33.4	34.0	1.8%
Variations in residence time	-τ	35.0	33.4	-4.5%	27.4	29.9	9.0%	34.6	34.2	-1.1%
	0τ	34.9	34.0	-2.7%	28.6	29.3	2.5%	33.5	34.2	2.1%
	+τ	37.1	37.3	0.4%	27.5	26.0	-5.4%	32.6	33.6	3.0%

		CH_4 STD ±0.07			H_2S STD ±0.04			LHV		
CAMPAIGN	Case	Exp.	Num.	Rel. error	Exp.	Num.	Rel. error	Exp.	Num.	Rel. error
Variations in pressure	-P	1.09	0.89	-18.8%	1.39	1.75	25.8%	6.85	6.98	1.8%
	0P	1.25	0.78	-37.4%	1.51	1.70	12.6%	7.17	7.26	1.3%
	+P	1.42	1.15	-19.3%	1.59	1.71	7.4%	7.51	7.31	-2.7%
Variations in temperature	-λ	2.72	1.76	-35.2%	1.95	1.76	-9.9%	7.95	7.58	-4.6%
	0λ	1.40	1.15	-18.3%	1.64	1.71	4.1%	7.31	7.31	0.0%
	+λ	0.76	0.72	-5.3%	1.55	1.69	8.8%	7.17	7.27	1.4%
Variations in residence time	-τ	1.44	0.78	-45.6%	1.55	1.70	9.9%	7.38	7.47	1.2%
	0τ	1.49	0.85	-43.2%	1.47	1.71	16.8%	7.33	7.39	0.8%
	+τ	1.15	1.37	19.2%	1.62	1.78	10.1%	6.86	6.96	1.4%

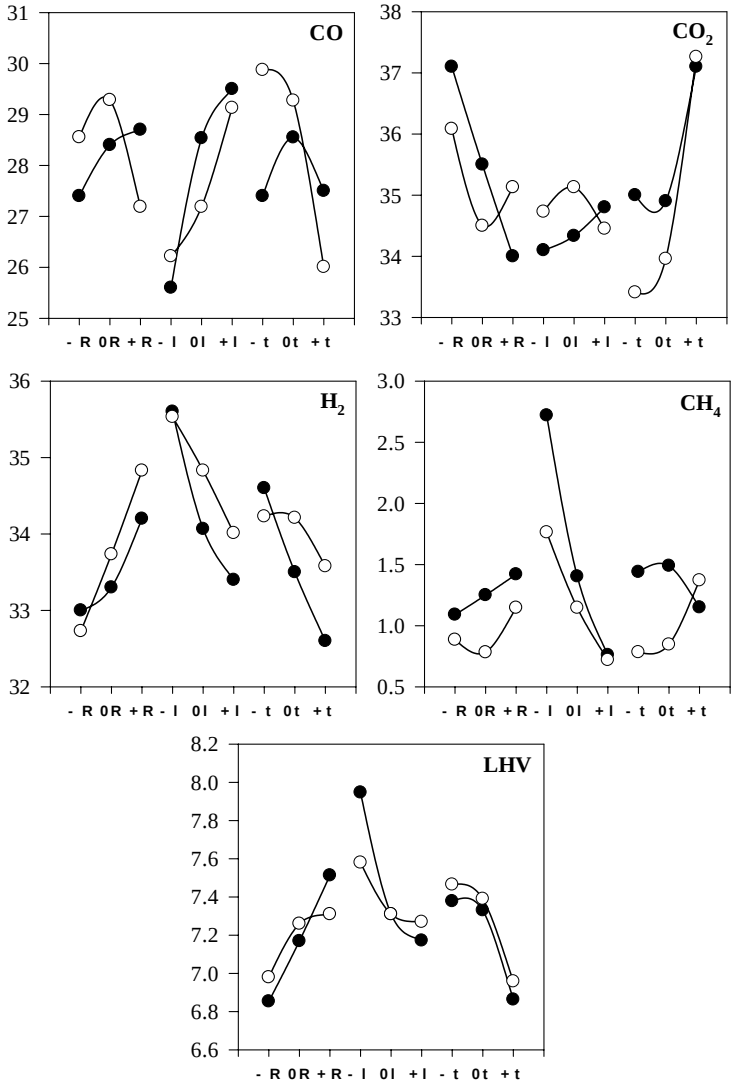

Figure 5. Numerical (obtained with CFD, empty circles) and experimental results (filled), units are % mol and MJ/kg (LHV, Lower heating value). Boundary conditions can be found in Table 1.

When the equivalence ratio is varied the predictions are encouraging. The increase in CO with increased equivalence ratio is captured as well as the decrease in H_2. In the experiments an increase in CO_2 was observed, this is not captured by the model. However, the increase in CO_2 observed in the experiments is relatively small, about 0.7% which corresponds to approximately two standard deviations. The largest relative error can be found for methane in the low temperature case

but encouragingly is significantly smaller at higher equivalence ratio. The trend in CH_4 is predicted with a significant increase at low temperature and a significant decrease at high temperature. The char conversion (Figure 6) show that an increase in equivalence ratio leads to an increase in char conversion and the difference is about 10 percentage points for the high temperature i.e. high equivalence ratio compared to the low temperature. The mean, outlet and probe position temperature all increase when the equivalence ratio is increased.

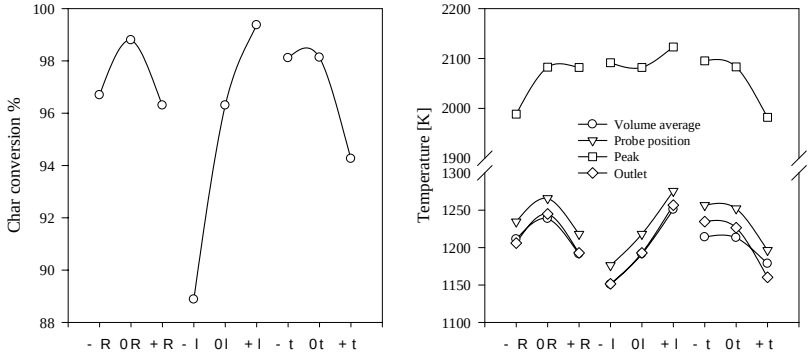

Figure 6. Char conversion (left) and temperature (right) obtained from the CFD simulations.

The residence time experiments were conducted at a constant pressure, that is, an increase in residence time was achieved by decreasing the black liquor mass flow rate and vice versa. Since the thermal power is also changed when the black liquor mass flow rate is varied the influence of the wall heat losses will be greater at long residence time/low black liquor mass flow rate. However, during the experiments the temperature inside the reactor was kept at around 1000 °C by changing the equivalence ratio. Given that the temperature was kept at about 1000 °C it was assumed that the wall heat losses will be relatively constant (since ΔT is constant cross the reactor wall) regardless of black liquor mass flow rate. The wall heat losses will however, be a greater portion of the thermal throughput. The experimental values for the short and medium residence time have almost equal equivalence ratio (see Table 1), and the methane concentration is almost constant when the process conditions are varied. The model predicts this fairly well. However, at the longest residence time the trend is lost. The predicted methane also has the largest relative error for the residence time experiments at around 45 %. This error is also reflected in the prediction of CO with a relative error of 9% which is the largest error for the main components in the entire set of simulations. Because of this, the trend predictions for the main gas components are not as clear. The trend in CO_2 is somewhat captured with fairly constant values at the short and medium residence time and an increase at the longer residence time. For CO and H_2 there is no clear trend from the model. The char conversion decrease at the longer residence time compared to the shortest as do all the temperatures. The lower

heating value is predicted very well for all the cases with the worst being the low temperature (-λ) case at -4.6%. The average relative error (for the heating value) for all the cases is about 1.7%.

1.5 Discussion

The initial PFR calculations performed in this work confirmed that the reformation of methane is significantly over-predicted when using the Jones mechanism in this temperature range. This comes as no surprise since the Jones mechanism was developed for combustion. In fact, Jones and Lindstedt (1988) shows that it performs very well for combustion; in a supplementary study (not presented in the report) where the Jones mechanism was compared to GRI-Mech in a counter flow oxygen methane jet flame it was confirmed that it performs fairly well given its simplicity. Additional PFR calculations were performed at different inlet gas composition with similar results (not presented in the paper); the Jones model showed significantly higher reformation rate of methane then GRI-Mech when looking at gasification conditions in the medium temperature range (1150 K< T < 1500 K). This probably explains why in our previous work (Carlsson et al. 2010b) we were not able to predict the methane concentration accurately in the DP-1 black liquor gasifier. The conversion of methane in a plug flow reactor with representative gas composition have been experimentally investigated by Valin et al. (2009) which obtained about 18 % conversion at a residence time of 2.1 s and a temperature of 1400 K. In the CFD-simulations 1400 K was set as the extinction temperature for the SMR reaction in order to get a reasonable prediction which is slightly higher than the value obtained by Valin et al. (2009). It is possible that an even higher extinction temperature would result in improved predictions of the CH_4 concentrations. However, 1400 K was considered as a reasonable value considering the results from the PFR calculations and the experimental results obtained by Valin et al. (2009). In an early stage of the present work a more comprehensive scheme was considered for the CFD model calculations. However, this approach turned out to be computationally too expensive and difficult to control regarding numerical stability. Hence, the current extinction temperature approach was chosen instead even if there are some uncertainties around the considered reaction mechanisms regarding the conversion of methane. Furthermore, there are catalytic effects present and uncertainties in the pyrolysis gas composition, which in the real case involves several hydrocarbon species that will affect the outlet gas composition. Thus, even if a more comprehensive scheme had been applied in the present case there is no guaranty that the outlet gas composition would have been predicted more accurately.

As can be seen in Table 5 the main gas components can be predicted within a relative error of about 5% when using the Jones model and the extinction temperature set to 1400 K and the SMR. Similar results were obtained from the oxidation model with CO/CO_2=16. The combined total error i.e. the sum of all the relative errors for each case and the considered species and heating value presented

in Table 5 is also similar for the two models (about 35%) with a slight advantage for the Jones model. The two reaction mechanisms are both of first order, i.e. the conversion of methane will be more or less constant at any initial concentration of methane. The presented results showed that the conversion of methane was about 60% for the oxidation mechanism and circa 90% for the Jones mechanism with SMR extinction temperature set 1400 K. This was regardless of CO/CO_2 ratio and hence the initial release of methane. The Jones model was chosen for the process condition variation calculations because it contains the SMR (which may have a strong influence on the results when the process conditions are varied) and that the Jones mechanism predicts the flame reasonable.

When the process conditions are varied the largest error for the main gas components can be found in the short residence time experiment (see Table 6 and Figure 5). The absolute error for CO is 2.5% which corresponds to 9% on a relative basis. For the same case, the methane prediction also shows the largest relative error of about 45 %. Regarding the char and CH_4 conversions, as can be seen in Figure 7 they both increase with increased temperature However, since the wall heat losses will influence the temperature in the reactor, the trend is not as clear when the same results are plotted against the equivalence ratio (right parts in Figure 7). The discrepancies that can be seen for the CH_4 prediction (particularly for the cases 0P, -λ +τ and 0τ) may be associated with the wall heat loss. In the simulations the heat loss was assumed constant at 90 kW (uniformly distributed at the wall) for all the cases. However, the temperature is measured with wall mounted thermocouples which may not measure a representative temperature, rather a mix of radiation from the flame, the walls, the gas and convection from the gas. That the wall heat loss can be assumed constant was based on the fact that a constant wall temperature would yield a constant ΔT cross the refractory and hence a constant heat flux but this may not be the case (since the temperature measurement may be wrong). In future work it may be more appropriate to include the refractory in the simulations (and use a fixed temperature boundary condition at the outside of the refractory) to see how it will influence the results, particularly the heat distribution and heat loss. The experimental results imply that the heat loss is smaller at reduced thermal power/black liquor flow rate. If the heat loss is smaller this would result in higher reactor temperature and hence reduced methane concentration in the outlet gas. In Figure 7 where CH_4 is plotted as function of equivalence ratio it may appear that the predictions are better at increased equivalence ratios. However, this effect is small; the absolute error decreases but the relative error is of same order.

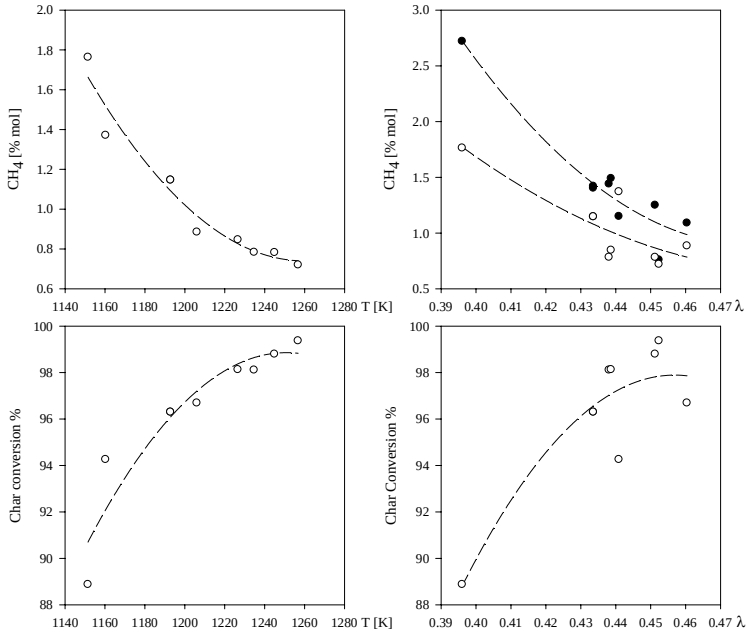

Figure 7. Upper: Simulated CH_4 outlet concentration as function of outlet temperature (left) and CH_4 as function of equivalence ratio (right) obtained from the simulations and from experiments (filled circles). Lower: Char conversion obtained from the simulation as function of outlet temperature (left) and equivalence ratio (right).

The H_2S released during pyrolysis was constant in all calculations (see Table 3) this will influence the results not just for the H_2S concentration. Marklund et al. (2007) showed that an increase of H_2S in the gas will effectively lead to a reduced reactor temperature and thus char conversion since more of the char is converted through the gasification reactions (MR3 and MR4) then by the sulphate reduction reaction (MR5).

The char conversion in the DP-1 black liquor gasifier is very close to unity since very little char is found in the green liquor or the green liquor dregs. The char conversion for the base case (0λ, +P) predicted by the model is about 96%, which results in the same order of relative error as for the main gas components. The low conversion of char for the low temperature case (-λ) is not representative for the DP-1 black liquor gasifier. However, the predictions may aid in the development of larger gasifiers. The low char conversion is most likely associated with the low temperature (Figure 7) and may be used as an analog for unconverted hydrocarbons. Hence, even if the predicted char conversion is lower then in the DP-1 gasifier the predictions still provide useful information when finding “safe” operating conditions for a larger gasifier or for optimization.

The simulations carried out in this work were done at operating conditions where data points were available. It is possible that additional simulations both between these points and at extremes could provided additional information about; at which operating conditions the model seems reliable.

In general the model predicts most of the trends and in some cases even the actual values from the experiments. The main goal was to make the CFD reactor model less dependent of prescribed model parameters and improve the predictions for a wider range of operating conditions while maintaining numerical stability and simplicity. This was achieved by using the extinction temperature approach described previously. A comparison with experiments have showed that the model is reliable and can be used for optimization or scale up as long as the pressure, equivalence ratio and residence time are kept within the boundaries studied. This however, does not limit the models validity for higher thermal powers i.e. reactor sizes.

1.6 Conclusions and future work

In this work, a global reaction mechanism developed by Jones and Lindstedt (1988) was compared to GRI-Mech in a 1-D plug flow reactor. The Jones model was then compared to a global oxidation mechanism using CFD and the influence of the reaction mechanism and initial release of CH_4 was studied. Finally the CFD model was compared to experimental values obtained from an entrained flow high temperature black liquor gasifier. From the results obtained the following conclusions can be drawn.

PFR calculations

- The agreement between the Jones model and GRI-Mech in a plug flow reactor is generally good if the temperature is above 1650 K.
- The Jones model over predicts the reformation of CH_4 if the temperature is kept below 1650 K.

Influence from variations in CO/CO_2 and reaction mechanism

- The CO/CO2 ratio and the gas/char carbon ratio will have a large influence on the amount of methane that is released during modeled pyrolysis.
- The reaction mechanism will have a large influence on how much methane that is reformed.
- It is possible to use an extinction temperature to separate the flame from the post flame region.

Influence from variations in process conditions

- When pressure is varied from 15 bar (g) to 27 bar (g) the main gas components (H_2, CO and CO_2) can be predicted within a relative error of 5.3%, the CH_4 within a relative error of 37.4% and the heating value of the gas within a relative error of 2.7%.

- When equivalence ratio is varied from 0.396 to 0.452 the main gas components (H_2, CO and CO_2) can be predicted within a relative error of 4.7%, the CH_4 within a relative error of 35.2% and the heating value of the gas within a relative error of 4.6%.
- When residence time (normalized) is varied from 0.65 to 1.28 the main gas components (H_2, CO and CO_2) can be predicted within a relative error of 9.0%, the CH_4 within a relative error of 45.6% and the heating value of the gas within a relative error of 1.4%.
- The resulting char conversion obtained with the CFD model increase with increased temperature.
- The resulting CH_4 conversion obtained with the CFD model increase with increased temperature.
- Most of the trends are predicted by the CFD model.

Future work

- Develop a model for the distribution of sulphur between the particle and gas system.
- Include the refractory lining and pressure vessel so a constant temperature boundary condition can be used at the walls instead of the current constant heat flux.

2. Numerical simulation of entrained-flow gasification of biomass with OpenFOAM

2.1 Introduction

Energy technology center in Piteå has since 2002 been working with simulation of combustion and gasification. The work has been carried out in the commercial code Ansys CFX. Different fuels (fuel oil, gas, coal and biomass) have been used in the simulations depending on the research topic or the customer requirements. Early on, the limiting factor on the size of the simulation, or rather, its complexity, was the computational performance and the accompanying cost of computational hardware. However in later years this has changed. Computers that have sufficient performance for Computational Fluid Dynamics (CFD) simulations have become relatively cheap. At least if the most complex models (such as detailed chemistry, large eddy simulations, direct numerical simulations) are avoided. So, now, the cost to increase the complexity does not lie in the hardware, it lies in the licensees that are required from commercial vendors of CFD software. These licenses are often core based, i.e. more CPUs equal higher cost. Hence, there are incentives to investigate free, open source CFD-software that can be used under General Public License. The benefits with these are, that the cost can be limited to just optional support agreements, hardware, and that the software is open source i.e. that it can be customized by the user to suit its needs. The drawback is mainly, less user friendly interface (often terminal based) which requires higher knowledge from the user, both on basics such as fundamental fluid dynamics and numerics but also programing. Nonetheless, for an experienced user the cost saving benefits and the customization benefits weighs heavy compared to a graphical user interface (GUI).

There are a number of different open source CFD software available, these are codes that have been developed both in the industry, by research institutions and by academia. Arguably the most common open source CFD software is OpenFOAM. Open source Field Operation and Manipulation (OpenFOAM) is a C++ based software for solving and processing continuum mechanics problem. The code was originally developed by Imperial College in the late 1980s and was released as open source in 2004. OpenFOAM include several different solvers that are tailored for specific problems; turbulent/laminar, compressible/incompressible,

particle tracking, combustion and so on. Hence it differs from commercial software such as Ansys CFX and Ansys Fluent which often use one solver for all problems, be it with some modification (which is not obvious from the user's standpoint). This work was initiated with the intention to investigate the capabilities of OpenFOAM to simulate biomass combustion and gasification. Hence the goal is to obtain a proof of concept using OpenFOAM to simulate gasification and combustion of biomass without a direct focus on comparison with experiments or model validity.

2.2 Models compared to precious work

This chapter focuses on previous work with commercial software and how that work was used to develop a model with similar structure and sub-models in OpenFOAM. Emphasis is on differences, potential areas of improvement and similarities.

In previous work the calculations were performed in Ansys CFX with a fairly, for the field standardized mathematical description. The pulverized biomass and the gas phase were described with an Euler-Lagrangian formulation. By this meaning that the gas phase was treated as a continuum with the accompanying averaged decomposed Navier-Stokes equations, and the particles as discrete source terms tracked through the domain with their motion governed by Newton's second law. There is a coupling between the discrete phase and the continuum phase so that drag, pressure and buoyancy forces can be taken into consideration. In addition, a stochastic random walk model was used to simulate the effects of turbulence in the continuous flow on the discrete particles. The particles were specified with a predetermined composition and particle size distribution. Turbulence was modelled with the k-ε model using scalable wall functions and radiation was modelled using the Discrete Transfer radiation model by Lockwood and Shah (1981). To ensure consistency between the experimental and modelled heating value, heat of reaction for pyrolysis in the model was taken as the difference between the modeled and experimental heating value.

In the simulation the biomass particle undergoes three conversions stages; drying, pyrolysis/devolatilization and finally char gasification/oxidation. The ash was treated as an inert in the simulations except when black liquor was simulated. In the black liquor case, the char carbon reacted with the sodium sulphate in the smelt/ash. Drying, devolatilization, char gasification and ash reactions where implemented in individual FORTRAN subroutines. For the gas phase, the global four step reaction scheme for methane by Jones and Lindstedt (1988) was used. The effect of turbulent mixing on reaction rates was taken into consideration with the Eddy Dissipation Model (EDM) together with Finite Rate Chemistry (FRC). The EDM-FRC model calculates the turbulent mixing rate and kinetic reaction rate and uses the minimum (i.e. slowest) of the two. A rotationally symmetrical geometry, which had a conventional entrained flow gasifier dimensions i.e. circular cross section and roughly 5 diameters long with a burner centrally mounted at the top was used in the simulations. Taking advantage of the rotational symmetry the

geometry was treated as a 2D wedge with periodic azimuthal boundary conditions. All calculations were done assuming steady state conditions with a steady state solver.

In OpenFOAM not quite the same implementation can be used. The software does not support discrete particle tracking in 2D wedge geometries (typically 5 degree wedges). However, cyclic boundary conditions can be applied and thus utilization of rotational symmetries is possible, as long as the simulated geometry have three dimensions. Of course also full 3D geometries are supported. OpenFOAM has some support for steady state particle tracking (as used in previous work). However, these are currently being described as “on prototype stage” and have not been considered in the current work, instead a full transient solver have been used. Hence, the computations in OpenFOAM are more computationally expensive compared to the commercial counterpart since larger computational meshes have to be used (3D instead of 2D) and a transient numerical scheme has to be utilized. The particle tracking can be made in a similar (except a transient scheme is used) way as in previous work, i.e. a coupled Euler-Lagrange formulation with a stochastic contribution on the particle path to account for turbulence. The same type of turbulence model was used as in the previous work in Ansys CFX. The combustion model and implementation of reaction kinetics is worth a special mentioning. In Ansys CFX the only practical combustion model for these types of flow problem is the species transport based EDM together with finite rate chemistry. The drawbacks and potential source for error from this type of model have been discussed in the literature (Brink et al. 2000). In the simulations in OpenFOAM the PaSR model developed by Golovitchev et al. (2000) was used. This model does not suffer from the same drawbacks as the EDM/FRC model does, and hence is a significant improvement. Also the implementation of reaction kinetics is significantly superior in OpenFOAM compared to CFX. In CFX each reaction has to be implemented separately, either using the GUI or the terminal on a specific CFX format. Hence reaction mechanisms on more common formats such as Chemkin cannot be applied directly. OpenFOAM has a Chemkin reader which can interpret Chemkin format directly, so both reaction mechanisms and thermodynamic data can be change by just pointing the reader to another file. Similar radiation models are available in OpenFOAM as in CFX. In this work the P1 radiation was used, mainly to speed up computational time but the finite volume discrete ordinate method is available which share some similarities with the Discrete Transfer model that was used in the CFX implementation. Drying and pyrolysis together with char oxidation are available as ready compiled sub-models for the discrete phase in OpenFOAM. However, char gasification is not available as a ready sub-model. Modification to the char oxidation model can be made to include char gasification but was not considered in this work.

2.3 Drop tube furnace and reactor modelling

Two different geometries were used to investigate the suitability of OpenFOAM to be used to simulate gasification and combustion of biomass. The first geometry was ETC's drop tube furnace or DTF. The second, a generic entrained flow reactor with the burner centrally position at the top.

The DTF consists of an injection system for gas and particles, a vertically mounted 2100 mm long ceramic reaction tube (50 mm inner diameter) and a sampling probe (Figure 8). The temperature in the reaction tube can be controlled by a custom made furnace (1998 mm in length) built by Entech AB (Sweden) and the atmosphere can be controlled using mass flow controllers which maintain a constant laminar flow of gas downwards through the reactor tube. The furnace consists of 5 heating zones, each 334 mm long and separated by 20 mm thick sheets of ceramic fiber. Each heating zone contains 4 SiC rods with a combined power of 2 kW. The injection system was mounted to the top cap and is comprised of; an air pre-heater mounted at an angle and a particle feeder connected to a vertical particle injection tube (6 mm inner diameter, 8 mm outer diameter). The particle injection tube was incased in a water cooled jacket and was inserted through the top cap into the ceramic reaction tube. The particle injection tube was inserted long enough to enable the first heating zone to act as a gas pre-heater.

The dimensions used in the CFD calculations were taken as specified earlier and the temperature was set to 1200 °C for the first heating zone. The temperature for the rest of the heating zones was set to 1000 °C. The feeder temperature was set to 80 °C and the fuel temperature to 20 °C. The gas mass flow rate was set to 0.15 kg/h in the fuel feeding line and to 1.5kg/h at the gas inlet. The fuel mass flow rate was set to 6 g/h. In these simulations nitrogen was used as carrier gas and surrounding atmosphere in the drop tube. Hence, the gas phase reactions were switched off to save computational time. Pyrolysis and drying of the biomass particles were on the other hand included. Drying was implemented as a heat transfer limited reaction, and pyrolysis as a kinetically limited reaction. Each pyrolysis specie can have its own kinetic rate but in this work, for demonstration, the same kinetics was used for all considered pyrolysis compounds (CH_4, H_2, CO_2). The computational mesh consisted of 800 000 hexahedral elements.

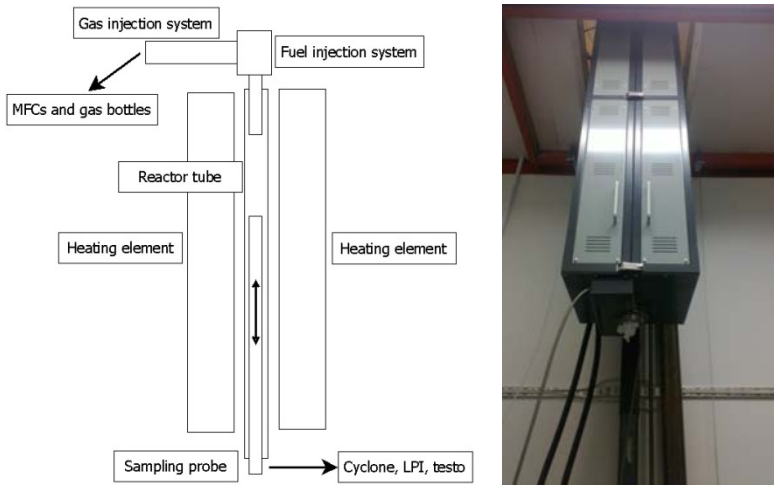

Figure 8. Left: Schematic drawing of the drop tube furnace. Right: Drop tube furnace as in installed.

OpenFOAM is very sensitive when periodic boundaries are used as in the reactor case. Whereas CFX has built in functions to determine neighboring cells on opposing periodic boundaries OpenFOAM will not find those if not special care is taken when the computational mesh is create. However, if the mesh is setup correctly and periodicity is defined when the mesh is created, OpenFOAM will find neighboring cells without problem. Hence, more care needs to be taken when creating a mesh for OpenFOAM compared to CFX. Initially, the modeled geometry had sharp transitions, i.e. the inner diameter changed like chamfers instead of smooth radiuses. However, this resulted in secondary flow which made the solution very time consuming and instead smoother transitions in the inner diameter was introduced (see Figure 9). In the reactor model, the global four step reaction mechanism for methane combustion was also introduced as was done in the CFX model. Oxy-combustion was simulated with a fifty-fifty mix of nitrogen and oxygen on mass basis at 700 kW with a calculated oxygen excess of 2% in the flue gas. 25 000 hexahedral elements was used in the mesh. A spherical source term was used as an igniter by injecting energy (for about one thousands of a second) thereby increasing the temperature sufficiently to get the reactor going.

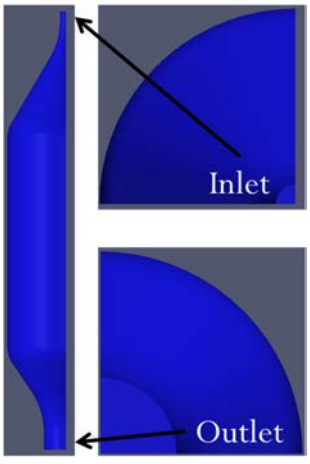

Figure 9. Reactor geometry.

2.4 Results and discussions

Now, the reader is reminded of the intention with this work. The intention with this work was to investigate the suitability of OpenFOAM to simulate biomass combustion and gasification. The work has also been conducted in this way. The focus has not been on tweaking model parameters, finding more suitable pyrolysis models, testing different radiation models, comparison with experimental data and so on. The focus has been to use existing OpenFOAM implementations that, with only minor modification can be used to simulate gasification and combustion of biomass and get a reasonable behavior without comparing with experimental data. The results should also be interpreted with this in mind.

2.4.1 Drop tube furnace

The drop tube furnace simulations were conducted so that fairly simple conditions could be applied, i.e. laminar flow, smaller influence of gas phase reactions because of the nitrogen environment and so forth. Also, coupling simulations of the drop tube furnace together with experiments could, in the future, be an excellent combination when comparing sub-models with experimental data. Here, the transient calculations also shine in comparison to their steady state counterpart. Since a transient solver is used, small fluctuations are not averaged out in the same degree as in a steady state solver and could, perhaps, aid in the interpretation of experimental data when in-situ experimental methods (such as spectroscopic) are applied. The results presented in Figure 10 and Figure 11 are separated about 0.04 seconds in time. The spacing was selected so that the reader should have some reference, but still demonstrate that even at this spacing a significant difference can be observed. Interestingly, at this computational grid resolution the pyrolysis envelope surrounding each parcel is clearly visible, particularly for the

smaller particles. At combustion conditions these envelopes are clearly visibly also in the experiments and are surprisingly large (see Figure 12).

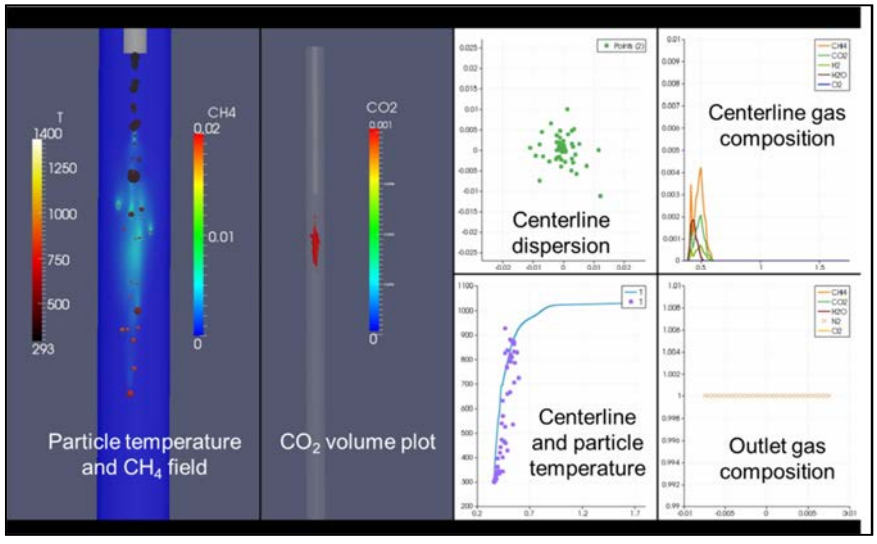

Figure 10. Drop tube furnace simulation, results at t= 0.126s. Particle temperature is on the black to white color bar.

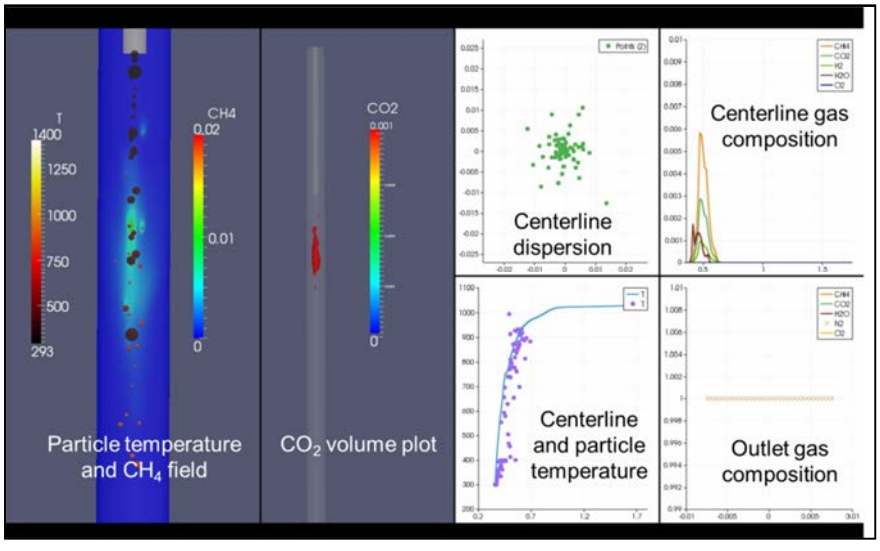

Figure 11. Drop tube furnace simulation, results at t= 0.166s. Particle temperature is on the black to white color bar.

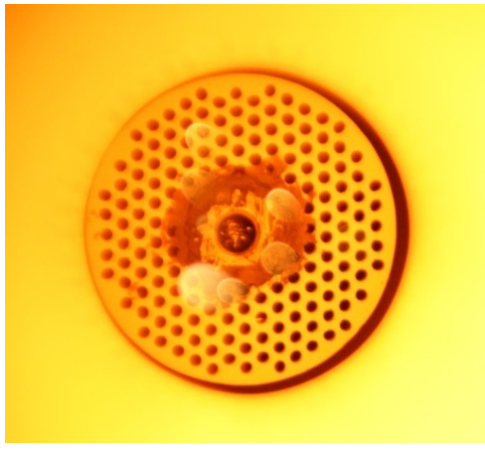

Figure 12. Photo of the DTF fuel inlet during combustion conditions. Notice the flame envelope surrounding individual biomass particles.

These initial calculations show great potential with an obvious room for improvement. Nonetheless, it's the author's opinion that; if this type of model in OpenFOAM is developed side by side with experiments in the DTF the boundaries can be pushed further compared to if a commercial code was used, or rather if a code that was not open source (which all commercial codes are).

1.1.1 Reactor

The reactor simulations were conducted to expand the model, and include more complexity. The global four-step reaction mechanism for methane by Jones and Lindstedt (1988) was included together with the PaSR-combustion model. A periodic mesh was created to determine which difficulties that would be encountered when using periodic meshes. A source term was introduced to ignite the reactor. All these add to the complexity and introduce additional steps that have to be taken into consideration both during the simulation and before. Initially a mesh with roughly the same number of mesh-elements where used in the reactor simulation as in the DTF simulation (around 800 000). However, this number had to be reduced significantly (to around 25 000) in order to get similar solution times (with respect to time steps per wall clock time). Hence the mesh used in these calculations is very course compared to the DTF calculations. The increase in solution time is caused by the gas phase reactions. It was found that the fastest reactions are the limiting factor, i.e. faster reactions require shorter time steps. In OpenFOAM the "chemistry time step" i.e. the time step required to accurately resolve the chemistry is not directly coupled to the time step used for the gas dynamics. However, there is a limit on how many chemical time steps that can be taken within one gas dynamics time step. If this limit is exceeded the code will throw an error of "to many iterations"- type. This can be resolved by decreasing the global,

gas dynamics time step, but as a consequent the solver time will increase. There may be possibilities to improve the performance by changing coefficients used by the chemistry solver but this was not investigated by the author.

In this work the Semi-Implicit method developed by Bulirsch and Stoer (1966) which is implemented in OpenFOAM was used with default coefficients. It appears that the largest problems with very short chemical time scales are at the beginning or early in the simulation before the flame has stabilized. The source term used to ignite the reactor can result in a little bit of an explosion behavior with multiple flame fronts with very high temperature and consequently very short time step. Some time was spent to modify the kinetics, and coefficients in the combustion model to slow down the reaction rate in the earlier stages of the simulation and then when the flame was stable change them back to their correct or default values. Although this work, the gas composition and temperature distribution in the reactor will basically be wrong after this treatment so a lot of time is needed to convect all gas out from the reactor so that the heat and energy balance is valid. This may even take longer than the initial time saving during flame stabilization.

The results presented in Figure 13 are snapshots of the solution at different time (denoted t in Figure 13). The source term is activated early in the simulation to prevent that oxygen spreads throughout the entire domain. This can be seen as a small temperature increase close to the inlet at t=0.1s in Figure 13. The flame then stabilizes fairly rapidly in the burner quarl. At this point it is difficult to judge the influence of the periodic boundary condition. The periodic boundary condition is forcing symmetry which may results in a more stable flame. The influence of this should be investigated in future simulations using full 3D geometries. After about two seconds the flame stabilizes with a distinctive shape in the burner quarl. The shape is probably caused by the course mesh spacing and the mesh should be refined in this region to get higher resolution in future simulations. The high oxygen content in the outlet stream is a result of poor particle conversion, i.e. particles leaving the reactor still have coal in them. Carbon oxidation (diffusion controlled) is included in the model but gasification with CO_2 and H_2O is not. Implementation of gasification reactions together with other coefficients for the char oxidation model may be the correct remedy to get better char carbon conversion. Even though this evaluation is in its beginning, and that the results only have been evaluated on a “reasonability-basis” it appears that OpenFOAM can be used, with good results to simulate biomass gasification and combustion and do offer some significant benefits compared to commercial codes.

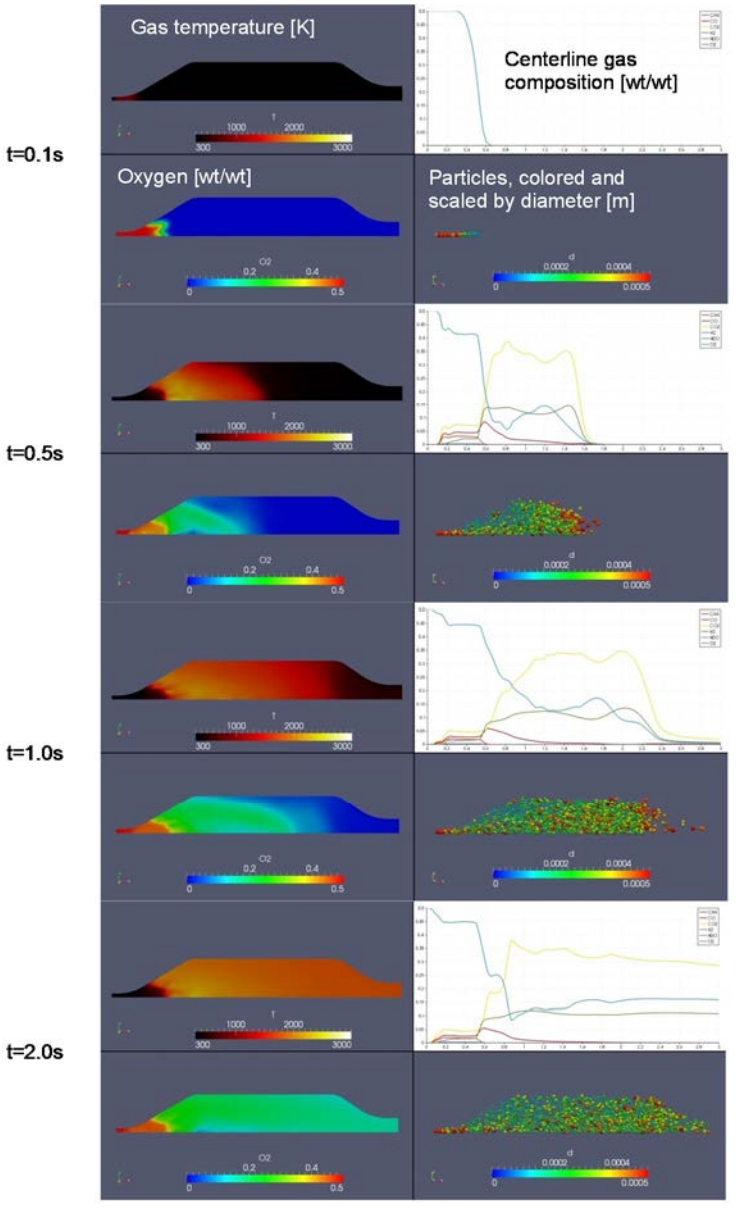

Figure 13. Reactor simulations solutions at different time.

2.5 Conclusions and future work

This report has focused on the feasibility of OpenFOAM to be used to simulate gasification and combustion of biomass. Some comparison has also been made

with commercial code, specifically Ansys CFX mainly to highlight differences, similarities drawbacks and so on. The main conclusions discovered during this work together with future work are itemized below.

- OpenFOAM appears to be at least as capable as Ansys CFX in simulating biomass gasification or combustion.
- In OpenFOAM the majority of the computational cost lies in solving the gas phase reactions.
- OpenFOAM solvers are much more sensitive to mesh setup (periodicity, face matching etc.) than Ansys CFX.
- Although not covered in the report decomposition and parallelization can be controlled and works without issues in OpenFOAM.
- More multiphase reactions can be added to OpenFOAM by modifying existing sub-models.
- Detailed energy and mass balance post processing should be developed in future work with OpenFOAM.
- Improved post processing for the particles should be developed in future work.
- In future work full 3D geometries should be compared to geometries where rotational symmetry is utilized.

3. Characterisation of submicron particles produced during entrained flow gasification of biomass

Particulate matter in the syngas from high temperature biomass entrained flow gasification is of interests since it could lead to clogging of downstream components or catalyst deactivation.

To our knowledge, no results regarding particle formation in larger scale oxygen blown entrained flow gasification where the gasification process is auto-thermal, is available in the literature. The results from this work may be used (i) to increase the knowledge of the various stages in particle formation (ii) as a reference case for development of well-controlled laboratory reactors for studies of various stages in the particle formation process during entrained flow gasification of biomass and (iii) to assess the particle load for the synthesis plant located downstream of the gasifier. The aim with this work is therefore characterise the particle produced during oxygen blown entrained flow gasification of biomass.

3.1 Experimental

3.1.1 Pressurised entrained flow gasifier

The Pressurised Entrained flow Biomass Gasification (PEBG) pilot plant was designed to operate in slagging mode with process temperatures ranging between 1200–1500 °C. A detailed description of the plant can be found elsewhere (Weiland et al. 2013) and therefore only a brief description is given here. The PEBG gasifier consists of a refractory lined reactor (0.52 m in inner diameter and 1.67 m in vertical reactor length) followed by a bubbling 2-level water sprayed quench for syngas cooling and smelt/particle separation. Five thermocouples (Type S, shielded with protective ceramic encapsulation) measured the process temperatures at different locations inside the reactor. One thermocouple was mounted in the upper part of the reactor, 0.46 m from the burner. Three thermocouples were mounted at the reactor middle circumference (1.05 m from the burner) and one thermocouple was mounted at the lower part of the reactor (1.66 m from the burner).The burner where the pulverised fuel and oxidant are injected is installed in the top of the reactor. The oxidant is a mixture of oxygen and nitrogen.

The raw syngas and other products from the reactor (i.e. gases, particles and ash/char) were cooled to temperatures below 100 °C by water sprays in the quench. Separated particles in the quench (i.e. ash or possible char and soot particles) either settled at the bottom of the quench or in the sedimentation vessel downstream the quench water outlet. The process pressure was controlled by a regulating valve on the syngas outlet pipe. Slip streams of the cooled syngas could be sampled from the outlet syngas pipe to measure both gas and particle concentrations. Finally, the produced syngas was flared on the top of the building.

1.1.2 Fuels and operating conditions

Measurement of the particle mass size distribution in the raw syngas was performed during five days in January and February 2012. To investigate the influence of fuel type, three different fuels were studied in this work. Commercially available stem wood pellets produced from sawdust of pine and spruce were tested during three separate days. Pure spruce bark pellets delivered from Södra Cell (pulp mill in Mönsterås, Sweden) and a bark mixture (spruce, pine and birch) separated from the pulp wood in Smurfit Kappa Kraftliner (pulp and paper mill in Piteå, Sweden) debarking drum were also used as fuels for one day each. For each fuel several measurements were performed to investigate the variation in particle concentration and particle size distribution. The fuel and its ash compositions (analysed by ICP) can be found in Table 7. The main difference between the three fuels is the significantly higher ash content of the two bark fuels than that of the fuel from wood powder. Furthermore, there was a large variation in ash composition of the bark mixture. The fuels were milled to powders using a granulator (Rapid Granulator 15 Series) and a hammer mill (MAFA EU-4B) connected in series. The resulting particle size distributions after milling were determined by sieving in a vibratory sieve shaker (Fritsch Analysette 3). Three representative samples from each fuel were sieved and the average particle size distributions were calculated.

Table 7. Physical, proximate and ultimate analysis of the fuels.

Fuel	Stem wood	Spruce bark	Bark mix
Particle size distribution			
d50 (µm)	100	100	160
d90 (µm)	310	220	340
Proximate analysis (wt% as received)			
Volatile	81.1	-	-
Fixed carbon	14.2	-	-
Moisture	4.3	7.1	4.5
Ash	0.4±0.02	4.3±0.4	4.5±2.0
Ultimate analysis (wt% dry)			
Carbon	50.9	52.2	52.6
Hydrogen	6.3	5.6	6.4
Nitrogen	0.10	0.41	0.38
Chlorine	<0.01	0.02	-
Sulfur	0.006	0.037	0.026
Oxygen (by difference)	42.4	37.5	38.3
Lower Heating Value (MJ/kg dry)	19.6	19.6	20.8
Major ash components (mg/kg)			
Si	79±54	4808±803	7010±5285
Al	26±10	1106±30	1728±1287
Ca	736±165	8719±303	6237±389
Fe	28±3	710±35	855±579
K	357±102	2034±82	2169±855
Mg	187±18	790±43	691±73
Mn	116±15	538±24	412±18
Na	15±8	431±1	690±457
P	48±9	460±22	396±36
Zn	9±1	97±6	121±2

The experimental conditions of the gasifier are summarized in Table 8. The gasifier was pressurized to 0.95 bars above atmospheric pressure. The mass flow of fuel to the gasifier corresponded to a thermal power of approximately 200 kW for all fuels. The oxygen equivalence ratio λ was varied between 0.44 and 0.49 and was selected to give a sufficiently high process temperature (~1100–1300°C) in the reactor. The residence time of the gas inside the reactor at these process conditions estimated from a plug flow assumption was in the order of 8 s. The resulting process temperatures in different locations of the gasifier and the gas composition are also given in Table 8. The process temperature in this work were defined as the measured temperatures of the thermocouples and this temperature differs from the real gas temperature inside the reactor due to radiative heat transfer between the thermocouples, the flame, and the surrounding walls. Compared to a possible full scale commercial gasifier (~100 MW_{th}, 30 bar), the reactor in the PEBG pilot plant has higher heat losses (~9% of the thermal energy of the fuel) since it is smaller and operates at lower pressure. Therefore, we have to run the experiment at slightly higher λ compared to a full scale gasifier in order to get the same process temperature in the reactor.

Table 8. Operating conditions, process temperatures and gas composition during the experiments.

	Wood				Spruce bark			Bark mixture				
Run	1	2	3	4	1	2	3	1	2	3	4	5
Sampling time, min	10	15	50	26	15	31	30	21	22	27	35	19
Pressure (barA)	1.95	1.95	1.95	1.95	1.95	1.95	1.95	1.95	1.95	1.95	1.95	1.95
Fuel feed, kg/h	40.0	40.0	40.0	40.0	40.0	40.0	40.0	40.0	40.0	40.0	40.0	40.0
O_2 feed, kg/h	24.5	24.5	27.0	27.0	24.0	24.0	24.0	30.0	26.0	26.0	26.0	26.0
O_2 concentration in burner, mol %	90	90	83	86	89	89	85	73	82	82	84	83
N_2 feed, kg/h	13.0	12.9	15.6	17.4	13.3	13.3	13.4	29.3	14.1	14.0	14.1	14.1
λ	0.44	0.44	0.49	0.49	0.45	0.45	0.45	0.49	0.44	0.44	0.44	0.44
Quench water level, %	33	33	35	35	30	30	30	30	30	30	30	30
T, top, °C	1192	1202	1240	1273	1087	1108	1118	1167	1181	1200	1178	1215
T, middle, °C	1183	1197	1179	1277	1099	1118	1125	1190	1197	1211	1207	1221
T, bottom, °C	1121	1136	1103	1221	1047	1066	1072	1144	1155	1166	1162	1179
T, quench, °C	81	81	60	79	78	79	78	86	83	83	83	84
T, raw gas, °C	41	41	30	40	33	37	37	39	43	43	42	44
N_2, %	18.4	18.3	21.9	17.9	18.9	15.7	18.3	32.3	17.1	17.0	17.3	16.9
CO_2, %	17.4	16.8	17.9	18.6	17.3	16.0	15.3	16.9	14.4	14.0	13.7	13.5
H_2, %	22.4	22.7	20.8	21.3	21.5	23.4	22.7	16.2	23.1	23.5	23.6	23.8
CO, %	39.3	39.6	36.7	39.7	38.6	41.3	39.9	31.8	42.4	42.7	42.7	43.1
CH_4, %	2.0	2.0	1.8	1.2	2.0	2.0	1.9	1.2	1.7	1.6	1.6	1.4
C_2H_2, %	0.23	0.23	0.19	0.17	0.14	0.11	0.11	0.14	0.14	0.12	0.13	0.11
C_2H_4, %	0.12	0.13	0.09	0.07	0.12	0.09	0.08	0.03	0.06	0.04	0.04	0.03

1.1.3 Particle and gas sampling

A schematic of the particle sampling system used in this work is presented in Figure 14. The insulated sampling line between the syngas pipe and the impactor was relatively long (4.5 m) because the impactor was installed in a separate room next to the gasifier for safety reasons. Particle samples were withdrawn from the centreline of the syngas pipe by a rapid dilution probe. The dilution probe was installed just after the pressure regulating valve that controlled the system pressure in the gasifier. The pressure in the syngas pipe just after the valve was close to atmospheric pressure and the temperature of the raw gas was about 40 °C.

In high temperature aerosol sampling systems (hot gas–cold dilution gas), the aim with a dilution probe sampling system is to size separate nuclei formed from inorganic vapour during quenching from pre-existing particles and prevent coagulation of particles in the sampling line. Since the raw syngas in this case was already cold most of the aerosol forming process that could affect the composition of the particles had already occured up-stream the sampling position. Instead in this work, hot dilution gas heated with an electrical heater to about 300°C was used to dry and dilute the raw syngas after the dilution zone in the sampling probe. The

temperature of the heated nitrogen just before the sampling probe is measured with a 1.5 mm K-Type thermocouple and the temperature at that position was approximately 210 °C. The temperatures directly after the heater and after mixing with the sample flow were determined with type K thermocouples. The temperature after the dilution zone was about 100°C. The flow rate of nitrogen to the dilution probe was controlled with a needle valve (NV1) to obtain a dilution ratio of about 100 times. The dilution ratio was defined as the ratio between CO measured in the dilute gas and the CO concentration measured in the syngas. The dilution ratio was selected in order to reduce the CO concentration in the diluted gas to <5000 ppm, since the instrument (Testo 350 XL) that measures the dilution ratio has a measurement range of CO between 0–5000 ppm. Furthermore, valves were also installed to enable flushing of the sample probe system before sampling in order to blow away any deposited particles from surfaces in the sampling system.

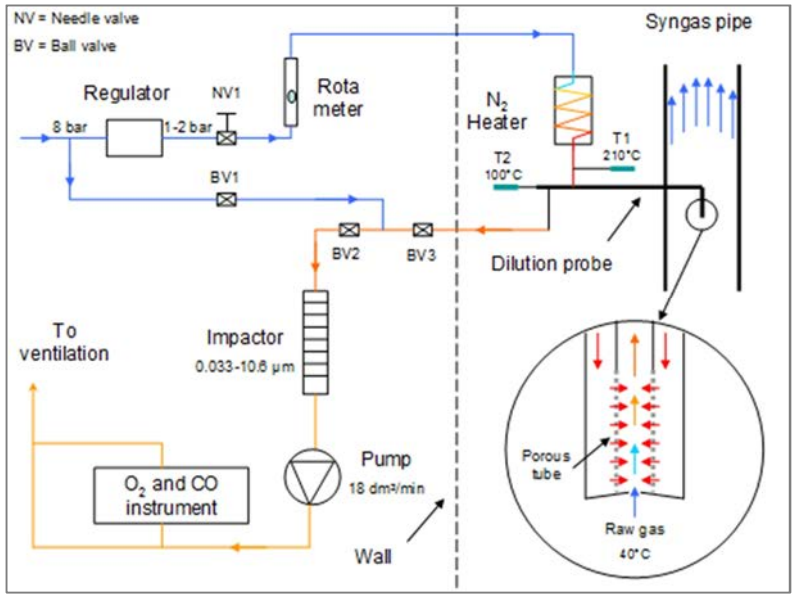

Figure 14. Schematic sketch of the particle sampling system.

The dry and diluted syngas was thereafter sent to a 13-stage low-pressure cascade impactor (LPI) from Dekati that analyses the aerodynamic particle mass size distribution within the range of 0.03–10 µm. The temperature of the LPI system was ~40 °C during the experiments. Non-greased aluminium foils were used as impactor substrates except for stage 13, which was the first stage after the inlet to the impactor. That stage was greased with Apiezon L (DS-515, Dekati) which is a high vacuum grease to increase the collection efficiency of any large particles. The impactor plates were analysed gravimetrically before and after each experiment with an analytical balance (±1 µg). The CO and O_2 after the pump were measured

continuously with chemical cells using a Testo 350 XL (Nordtec Instrument) to check the overall dilution ratio of the system.

Sampling of the produced gas was also performed continuously under the experiments by withdrawing a slip stream of the produced gas through a particulate removal equipment and a water condenser. A micro-GC measured the H_2, N_2, O_2, CO, CO_2, CH_4, C_2H_4, and C_2H_2 concentrations in the dry syngas every 4 minutes.

3.1.2 Chemical and physical analysis of particulate matter

Particle matter on impactor plate 1 with a particle diameter for 50% collection efficiency (d_{50}) of 0.033 µm, plate 6 (d_{50} = 0.411 µm), and plate 8 (d_{50} = 1.038 µm) was analyzed for morphology with a scanning electron microscope (JEOL JSM-6460) equipped with an X-ray energy dispersive detector (Oxford Instruments) for chemical analysis of both the inorganic and the carbon content of the particulate matter (SEM/EDS). Particles collected on plate 1, plate 6 and plate 8 represents the beginning, mode and the end of the particle size distribution and therefore these plates were chosen for SEM/EDS analysis. For each impactor plate 3 to 5 area analyses were performed on the particle sample stacks. The particles were examined without any coating.

Particle matter on plate 1 and 6 for each fuel was further analysed with a combination of high-resolution transmission electron microscopy (HRTEM), energy-disperse X-ray spectroscopy (EDS) and in some case also selected area electron diffraction (SAED). SAED is a crystallographic experimental technique that is performed inside a TEM microscope for investigation of the structure (crystal, polycrystalline, and amorphous) of a material similar to X-ray diffraction (XRD), but unique since very small areas (nanometer scale) can be examined. For a single crystal a clear diffraction pattern is created were each spot in the diffraction pattern corresponds to a specific position in the unit cell of the crystal. For polycrystalline materials a ring pattern is created and finally for amorphous materials only a broad spot is created in the centre of the diffraction pattern. Particles collected on plate 8 was not analysed with HRTEM since they may become too thick for proper analysis with HRTEM. Particle matter from each impactor plate was mechanically transferred to the TEM grid. The particles have thereby in the sample preparation not been exposed for any type of fluid that may affect the morphology of the particles. The samples were thereafter examined in a JEOL JEM-2100F instrument equipped with an EDS detector. The particles on the TEM grid were also examined without any coating.

3.1.3 Penetration of elements through the gasifier

The amount of ingoing elements with the fuel, η_i that finally ends up in the particles in the produced gas after the quench has been estimated according to equation 1

$$\eta_i = \frac{Q_{gas} PM_{gas} C_{particle,i}}{m_{fuel} C_{fuel,i}} \qquad \text{i = C, S, Cl, K, and Zn} \qquad (1)$$

where Q_{gas} (Nm^3/h) is the flow of produced gas, PM_{gas} (kg/Nm^3) is the particle concentration in the produced gas, $C_{particle}$ (wt-%) is the concentration of element *i* in the particles, m_{fuel} (kg/h) is the mass flow of fuel and finally C_{fuel} (wt-%) is the concentration of element *i* in the fuel. The η_i in this work has been estimated from the particle concentration measured with the DLPI and the elemental composition of the particles collected on impactor plate 6 from that specific experiment. The study was limited to carbon, sulphur, chlorine, potassium and zinc since it were these elements that gave a significant contribution to the elemental composition of the collected particles. Plate 6 was assumed to represent the whole elemental composition of the particles since it represents the particle mode diameter in the particle size distribution. This is a good assumption since particle collected on plate 6 represents more then 80 wt-% of the analysed particle mass.

1.2 Results, observations and discussions

1.2.1 Stem wood

Figure 15 presents a summary of the particle mass size distribution, the bulk elemental composition (detected by SEM/EDS) and morphology (detected by TEM) of the particulate matter from plate 1 and 6 when stem wood was used as raw material in the gasifier. The particle concentration in the produced gas varied between 86 to 289 mg/Nm^3 in the different experiments. Particle mass size distribution was dominated by particles with an aerodynamic diameter <1 µm (submicron particles). The particle mode diameter was approximately 0.5 µm for all experiments. The elemental composition was totally dominated by carbon (>95 wt-%) for all particle sizes with a small amount of potassium (0.6–1.9 wt-%). For the smallest particles, it was also possible to detect traces of oxygen and refractory elements.

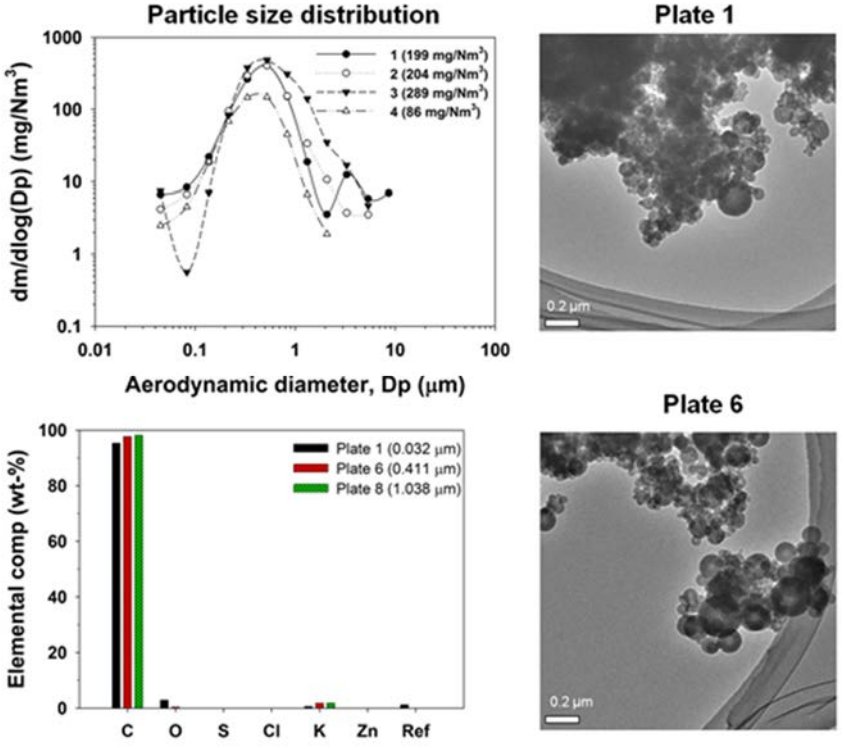

Figure 15. Particle size distribution, particle concentration, elemental bulk composition of selected particle sizes (SEM/EDS) and morphology of particles (TEM) during gasification of stem wood. Ref = refractory elements (e.g. Si, Ca, Fe, and Mg).

Two different types of primary particles could be detected, small spherical particles with a primary particle diameter of ~30–50 nm. This type of particles is hereafter referred to as fine primary soot particles. The second type of particles were also spherical but with a significantly larger diameter, ~0.1–0.3 µm. This type of particle is hereafter referred to as large primary soot particles in the text.

Figure 16 presents typical HRTEM images of both the fine and large primary soot particles. The fine primary soot particles consisted of monolayers of carbon atoms, graphene that grows perpendicular to the centre of the particle in the direction of the surface forming a particle with concentrically stacked graphitic layers. Both the size of the primary particle and its microstructure is typical for soot particles, and have been reported previously for soot generated during combustion in diesel engines and pulverized coal flames. The microstructure of the large primary soot particles can also be seen in Figure 16. Generally, the large primary soot particles consists of two parts, a centre and one or more shells depending on the size of the particle. The size of the centre is ~50–100 nm. Unfortunately, due to the particles thickness it was impossible to get a clear picture of the microstructure

of the centre. However, the SAED pattern of the centre of the large primary soot particle indicates the lack of ordered structure since only one clear diffraction point was observed. The size and microstructure of the shell can clearly be seen in Figure 16. The thickness of the shell is ~40 nm and the microstructure of the shell is similar to the microstructure of a small primary soot particle. The SAED pattern of the outer layer also shows an orientation of the microstructure since arc where observed in the diffraction pattern. For the largest soot particles identified in the TEM image, it was possible to identify multiple shells around the centre of the particle where the size of the individual shell where ~40 nm.

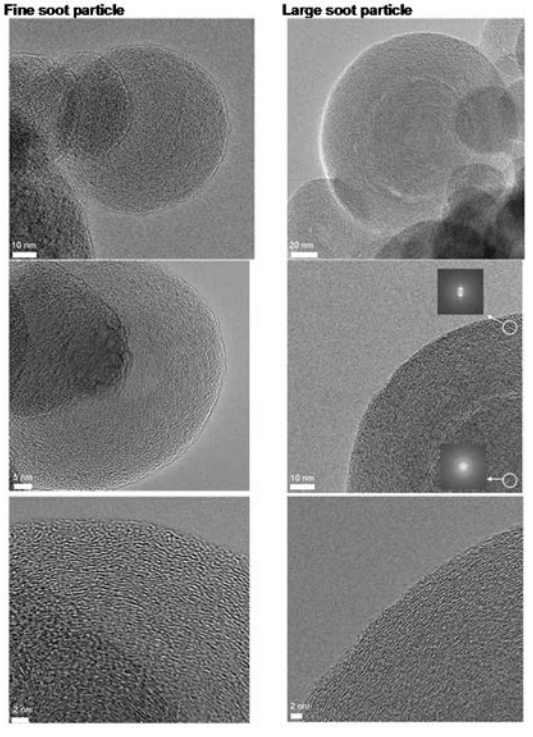

Figure 16. HRTEM images of typical fine and large soot particles during gasification of stem wood.

The formation mechanism of both the fine primary soot particle and the large primary soot particle are most likely the same. The structure between the two was similar and the shell of the large primary soot particle may have been created around the centre of a fine soot particle. The surface growth from fine primary soot particle to large primary soot particles may be caused by recirculation of fine primary soot particle to the flame. The flow pattern in the reactor created by the central flame and the geometry of the reactor actually allows pre-existing soot particles to pass through the flame again several times after it has been formed. This is

caused by the reverse flow (down flow in the centre and up flow against the wall) in the reactor. Practically, the formation of large primary soot particles is not optimal for complete carbon conversion, since oxidation with CO_2 and H_2O of large primary soot particles are most likely longer compared to oxidation of fine primary soot particles due to its larger mass.

The presence of large primary soot particles is not so commonly described in the combustion literature as for the fine primary soot particles. However, Chen et al. (2005a) could identify similar particles during pulverized coal combustion in a laboratory furnace. The structure of the large primary soot particles seems also to be similar to commercially available pristine carbon nano spheres (diameter100 and 200 nm) that are used in the electrical industry. Septien et al. (2012) also identified large particles from SEM images during their high temperature pyrolysis experiments in a drop tube furnace. No HRTEM image of the microstructure of large particles was available in that paper, but the presence of large particles indicates that the formation of large primary soot particles is a common phenomenon during entrained flow gasification of biomass. Probably the residence time in a reduced region that allows a significant soot surface growth is much larger in a gasifier flame (reduced environment downstream the flame) compared to traditional flames (oxidised environment downstream the flame).

1.2.2 Spruce bark and bark mixture

Figure 17 and 18 present a summary of the particle mass size distribution, bulk elemental composition (detected by SEM/EDS) and morphology (detected by TEM) of the particulate matter from impactor plate 1 and 6 when the spruce bark and the bark mixture were used as raw material in the gasifier, respectively. The particle concentration in the produced gas varies between 70–88 mg/Nm^3 for the spruce bark (Figure 17) and between 46–130 mg/Nm^3 for the bark mixture (Figure 18). The particle concentration in the raw gas was in general slightly lower compared to when pure stem wood was used as raw material. Again, for both of the bark based fuels, the particle concentration was totally dominated by submicron particles with a mode diameter of ~0.4 µm which is slightly smaller compared with the stem wood mode diameter (~0.5 µm, see Figure 15).

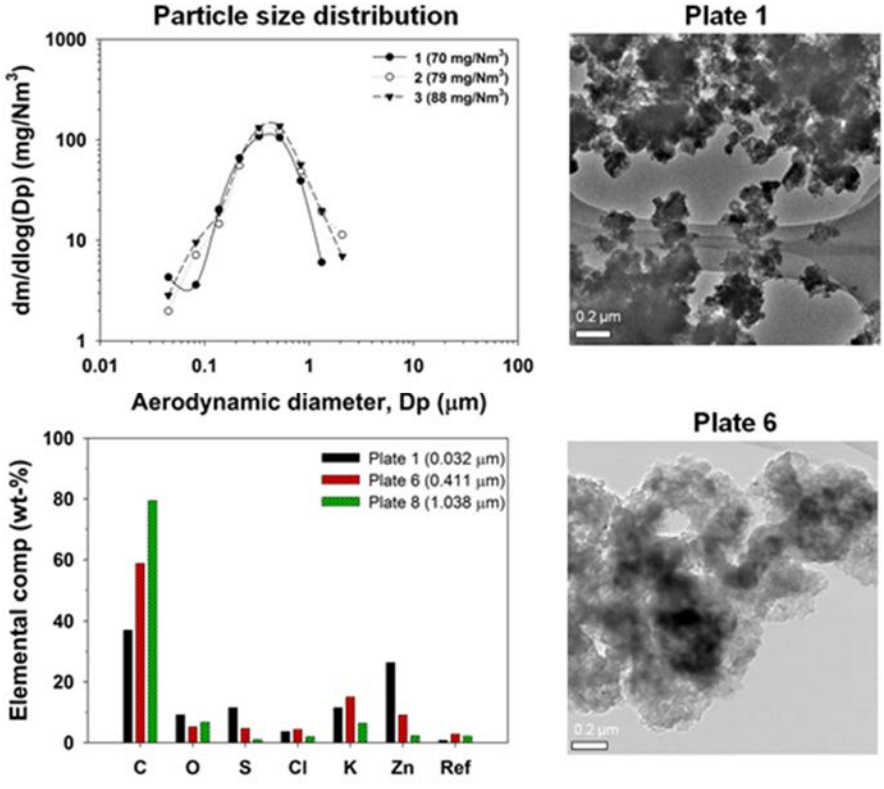

Figure 17. Particle size distribution, particle concentration, elemental bulk composition of selected particle sizes (SEM/EDS) and morphology of particles (TEM) during gasification of spruce bark. Ref = refractory elements (e.g. Si, Ca, Fe, and Mg).

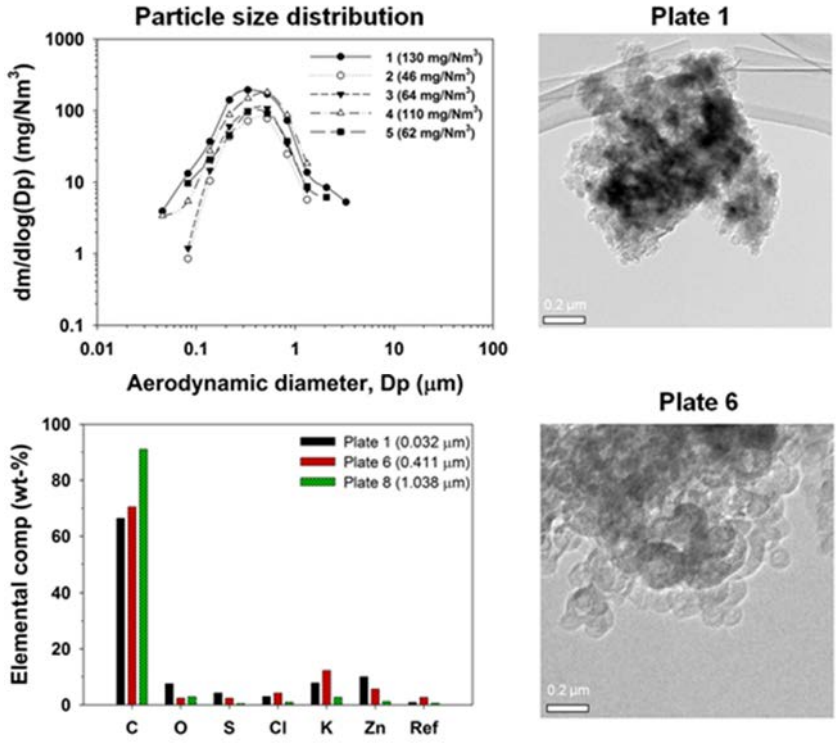

Figure 18. Particle size distribution, particle concentration, elemental bulk composition of selected particle sizes (SEM/EDS) and morphology of particles (TEM) during gasification of spruce bark. Ref = refractory elements (e.g. Si, Ca, Fe, and Mg).

There were significant morphological differences between particles generated from spruce bark gasification compared with those from stem wood gasification. The shape of the particles from spruce bark were in general irregular (see Figure 17) compared to the spherical particles from stem wood (see Figure 15). Furthermore, it was not possible to identify any larger primary particles with a diameter >0.1 µm in the impactor samples as it was for the stem wood. However, for the bark mixture (see Figure 18), the generated particles were more similar to the particles generated during gasification of pure stem wood. The particles were round and it was again possible to identify large primary particles with a diameter of ~0.2 µm from impactor plate 6.

The bulk elemental compositions of the particles from the two bark-based fuels were significantly different from that of pure stem wood. In addition to carbon, the particulate matter also consist of significant amounts of oxygen, easily volatile ash elements (potassium, zinc, sulphur and chlorine) and a small amount of different refractory elements (silicon, calcium, manganese, and iron). The amount of carbon in the particle matter also increases significantly when the aerodynamic diameter

of the particle increased, as indicated by the elemental composition for the impactor plates presented in Figures 17 and 18. Interestingly, for each particle size distribution, the particle composition with respect to zinc and sulphur shows the same trend, see Figure 17 and 18. This could indicate that zinc and sulphur were bound to each other in a chemical compound such as ZnS. Similary, potassium and chlorine have the same trends (see Figure 4 and 5) which could indicate KCl.

Compared with combustion of biomass, the same ash forming elements were found in the submicron particles during entrained flow gasification. One significant difference could however be found regarding the oxygen content of the particle matter between combustion and gasification of biomass since it is much lower during gasification compared to combustion. This indicates that the ash forming elements should form chemical compounds with a more reduced form during entrained flow gasification compared to combustion. For example, potassium and sulphur will most likely form K_2S in reduced atmospheres (gasification) and not K_2SO_4 as it is the situation in an oxidised environment (combustion). The cations K+ and Zn2+ will be bound with possible anions of O2-, S2-, Cl-, OH-, and $CO_3$2- forming fly ash particles of K_2S, KOH, K_2CO3, ZnO, ZnS, and $ZnCl_2$ in a reduced atmosphere or be presented in its metallic form.

Table 9 shows the fraction of carbon, chlorine, sulphur, potassium, and zinc in the fuel that ended up in particles in the cold synthesis gas after the quench. Only a very small fraction of the carbon that was added to the gasifier through the fuel ended up in the submicron particles after the quench (maximum 0.1 wt-%). For the inorganic elements, however, the fraction that ended up as submicron particles was significantly higher, especially for zinc where about 10 % of the zinc that enters the gasifier with the fuel ends up as submicron particles in the raw gas after the quench.

Table 9. Fractions of elements contained in the exit submicron particles compared to the elemental inlet flow with the fuel.

Element (wt-%)	Wood	Spruce bark	Bark mixture
C	0.1	0.02	0.04
Cl	-	3.2	-
S	-	1.8	2.0
K	2.6	1.1	1.2
Zn	-	13.7	10.0

During gasification of the more ash-rich, bark-based fuel, several different types of individual particles could be detected by the HRTEM investigation of the particulate matter where the shape and microstructure seemed to follow the concentration of carbon and ash forming elements in the individual particle. When the carbon content was >90 wt-%, the shape of the particles was spherical and generally showed a microstructure with staged graphite layers (see Figure 19) similar to the soot particles identified for pure stem wood. However, there were small differences regarding the microstructure of the particles as shown in the different HRTEM images presented in Figure 19. One general characteristic for the primary

soot particle generated during gasification of the bark-based fuels, was that the soot particles seemed to be more mature due to higher structural order and longer fringe length compared to the primary soot particle generated during gasification of stem wood (see Figure 16).

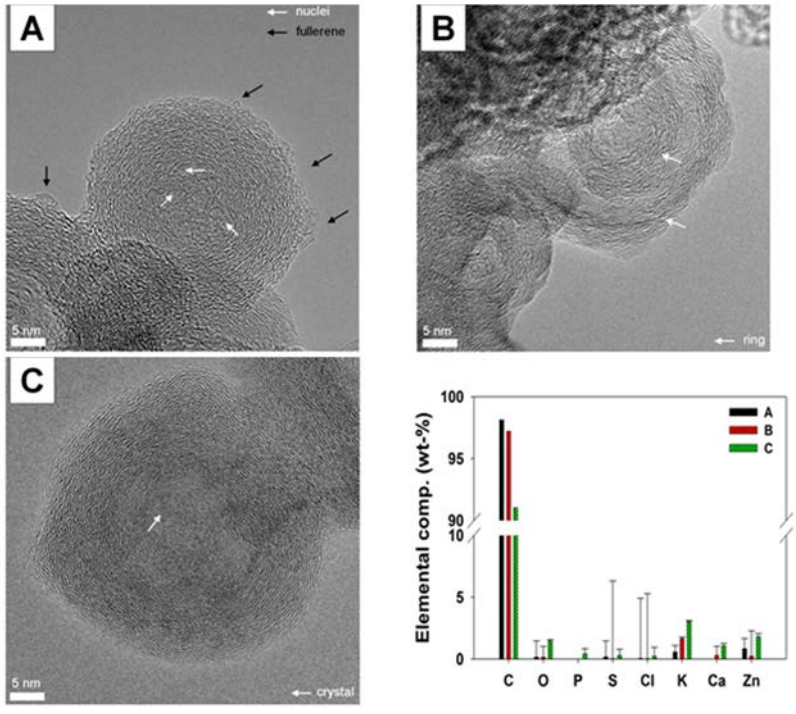

Figure 19. HRTEM images of soot particles during gasification of the bark mixture. The elemental compositions of the investigated particles are also presented in the last plate. Large error bars in the EDS analysis indicate that the identified element is trace elements.

It was also often possible to identify multiple nuclei with a diameter of ~2 nm in the centre of the particle (see Figure 19a, white arrows) in a similar way as first was observed by Ishiguro et al. (1997) for diesel soot particles. These multiple nuclei were also recently observed during studies of soot particles from pulverized coal combustion. It was also often possible to identify small particles with a typical size of ~1 nm attached to the surface of the particle (see Figure 19a, black arrows). Similar particles produced during pulverized coal combustion attached to the surface of a soot particle have previously been identified as fullerene nanocarbon particles. As shown by white arrows in Figure 19b, the ring structure of the soot particles is more dominant for some particles. Chen et al. (2005b) suggest that the graphitic structure can be a result of catalytic activity by the metal environment resulting in a more ordered structure of the graphite layers. For pure soot particles it has also been shown that heating of a soot particle to temperatures >2500 °C,

either with a pulsed laser or an un-known technique could result in partial graphitization of the shell of the soot particle. The microstructure of the particle presented in Figure 19b could therefore be a result of catalytic graphitisation in combination with a rapid heating of the particle in the hot gasifier flame. For the particle shown in Figure 19c, which also consists of a non-graphitic centre and a partial graphitic shell, it was also possible to identify crystals of ash forming elements in the centre of the nanocarbon particle (see the white arrow, Figure 19c). Apart from carbon, the particles consisted of a significant amount of potassium and zinc, and in some case also oxygen and calcium. In the EDS spectrum it was also possible to identify traces of phosphorus, sulphur and chlorine in these particles. The EDS spectrum also indicated that zinc and potassium are mainly present in their metallic form since the concentration of sulphur and chlorine was very low compared to the concentration of zinc and potassium. Furthermore, the EDS spectra for the particle presented in Figure 19c indicate the presence of CaO in that particle since both the concentration of calcium and oxygen was significant.

When the carbon content in the particles was below 90 wt-%, the shape and the microstructure of the particles significantly change as shown in Figure 20. Instead of spherical particles with a clear staged graphite microstructure, the particle shape now looks like irregular flakes and even at relatively high magnification in the microscope it is not possible to identify any characteristic microstructure (see Figure 20c) in a similar way as for the soot particles. This indicates that the particles have an amorphous microstructure. Apart from carbon the particles consisted of a significant amount of zinc, potassium, sulphur and oxygen. The particles also consisted of a smaller amounts or traces of magnesium, silicon, phosphorous, chlorine and calcium. The consequence of having carbon rich particles which includes ash forming elements (i.e., particles in Figure 19 and 20) is connected to the functionality of the quench scrubbing system of the gasifier. The separation of carbon rich particles (insoluble in water) from the gas is most likely ineffective compared to separation of fly ash particles. The fly ash particle consists of easily volatile ash forming elements which are water soluble and therefore are easier to separate from the gas in a quench scrubbing system. Practically, this means that ash forming elements can penetrates to a larger extent through the quench if they are present within a carbon rich particle instead of a fly ash particle. This is not preferable since catalysts can be very sensitive to poisoning from ash forming elements.

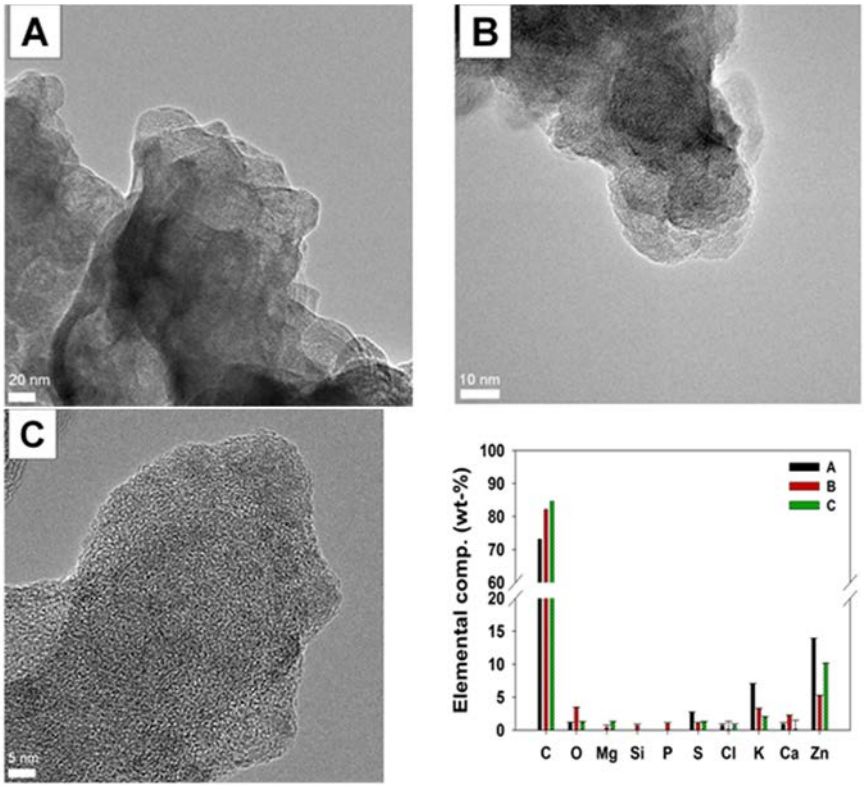

Figure 20. HRTEM images of “graphite plates” during gasification of spruce bark (plate A and C) and bark mixture (plate B). The elemental compositions of the investigated particles are also presented in the last plate. Large error bars in the EDS analysis indicate that the identified element is trace elements.

When the ash forming elements start to dominate the individual particle composition the microstructure of the particle starts to show a polycrystalline structure as shown in Figure 21. From the HRTEM image of the centre in Figure 21, it is possible to identify small single crystal regions (grains) where the size of the crystal is in the order of 1 nm. The SAED pattern also indicates a polycrystalline pattern since a ring forming structure was observed. Regarding the ash forming elements, the particle start to be dominated by zinc with a minor amount of the other inorganic species that have been observed in the previous particle types.

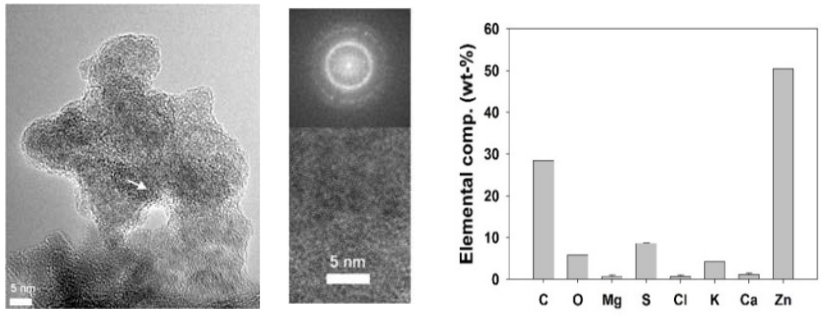

Figure 21. HRTEM images of an ash forming element dominated particle produced during gasification of spruce bark. The elemental compositions of the investigated particles are also presented in the last plate. Large error bars in the EDS analysis indicate that the identified element is trace elements.

It was also possible to identify a large number of particles that were totally dominated by zinc (see Figure 22 and 23). These particles have an irregular grain-like shape with a characteristic size of about 50 nm (see Figure 22a). An EDS analysis of the particle composition in Figure 22a shows that the elemental composition of zinc was about 80 wt-%. The particles also consist of carbon and the other ash forming elements that have previously been identified in the other particulate types. At higher magnification it was also possible to identify almost pure zinc particles (95 wt-% of zinc) with a polycrystalline microstructure in the HRTEM images (Figure 22b). Other elements found in those particles were carbon, oxygen and sulphur. Compared to the particle presented in Figure 21, much larger single crystal particle size (~5 nm) could be identified within in the polycrystalline structure. The SAED pattern of the particle also indicates a more ordered and crystalline structure since diffraction points could be observed.

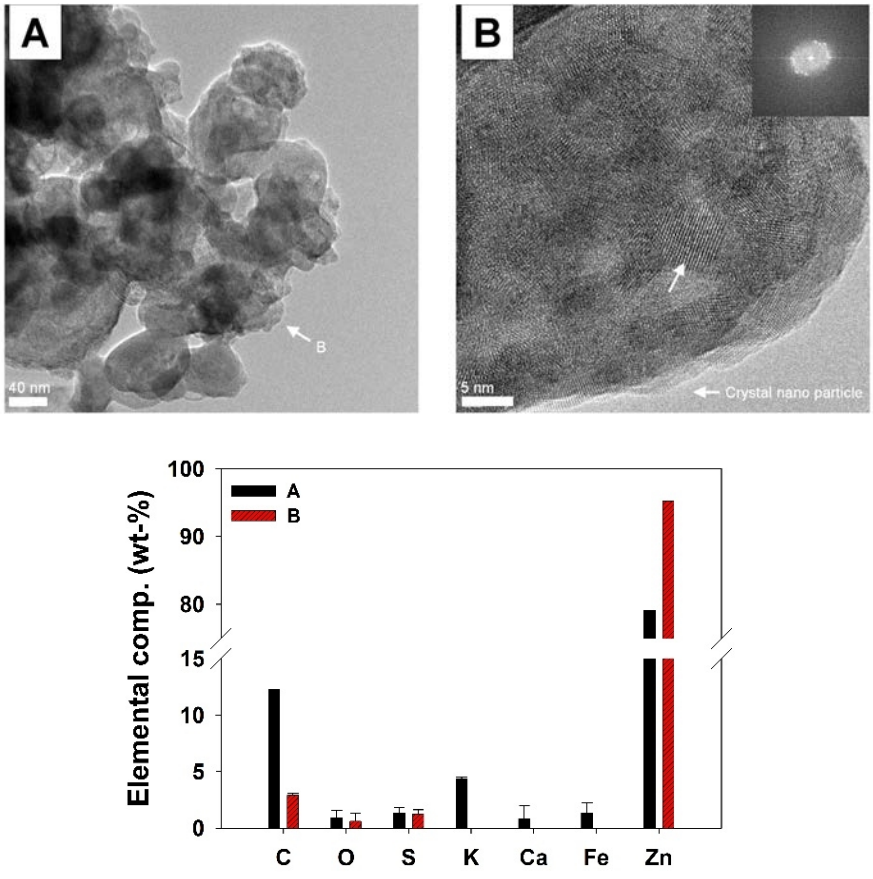

Figure 22. HRTEM images of zinc dominated particles during gasification of spruce bark. The elemental compositions of the investigated particles are also presented in the last plate. Large error bars in the EDS analysis indicate that the identified element is trace elements.

As shown in Figure 23 it was also possible to identify single zinc rich crystals attached to the surface of larger particles. Those particles had a spherical shape and the diameter of the particles was also in the order of 4–5 nm. The spacing between the lattice fringes in the particles is about ~0.25 nm, as indicated in Figure 23b. Metallic zinc has a hexagonal closed packed unit cell structure with cell lattice parameter a and b in the unit cell of 0.2665 nm and 0.4947 nm respectively. The identified distance (~0.25 nm) in figure 23b was thereby very close to the lattice parameter a, which indicates that the particles in Figure 23b are pure metallic zinc crystals. Other possible zinc compound crystals such as ZnO (lattice parameter a 0.3250 nm) and ZnS (lattice parameter a 0.3821 nm) have much larger lattice parameters than ~0.25 nm.

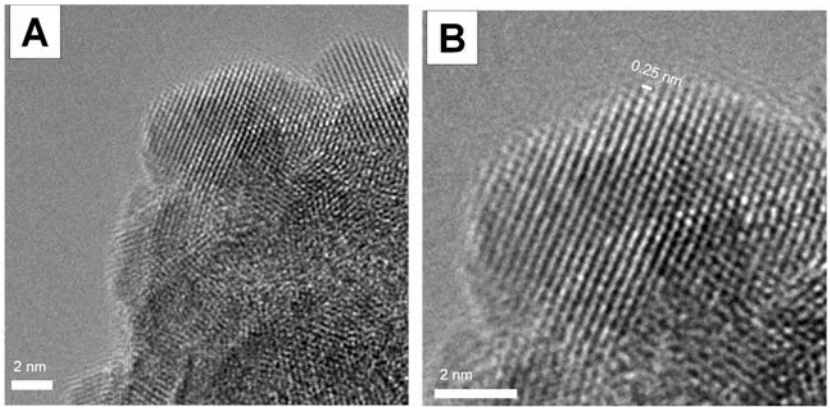

Figure 23. HRTEM images of zinc rich crystals attached to the surface of larger particles produced during gasification of bark mixture (plate A). The distance between the planes in the crystal is indicated in plate B.

1.3 Conclusions

Based on the measurements of the particle mass size distribution with the impactor and subsequent analysis of the particulate matter on the impactor plates with SEM/EDS the following overall conclusions can be drawn;

- Particles with an aerodynamic diameter < 1 µm (submicron particles) dominate the particle size distribution in the syngas after the quench during entrained flow gasification of biomass. Practically this means that an advanced gas cleaning technology (filter or electrostatic precipitator) need to be installed downstream the quench if the particle concentration needs to be reduced further.
- The elemental composition of the submicron particles are dominated by carbon with smaller amounts of easily volatile ash forming elements (K, S, Cl, and Zn) and traces of refractory elements (Si, Ca, Mg, and Fe).
- The amount of ash forming elements in the submicron particles is significant dependent on the parent fuel ash composition and increases with increasing ash content of the parent fuels. Therefore, the concentration of ash forming elements in the submicron particles was higher for bark compared to stem wood.
- Smaller particle sizes in the particle mass size distribution have a higher concentration of ash forming elements compared to larger particle sizes.
- Submicron particles could penetrate through the quench scrubber system to some extent. The resulting particle concentration in the raw syngas after the quench varied between 46–289 mg/Nm^3 in this work. Practically this means that the particle concentration needs to be reduced several order of magnitudes before it for example can be used in a catalytic process for production of liquid fuels.

- A significantly larger fraction of the zinc introduced to the gasifier with the fuel ends up in the submicron fraction compared to the other easily volatile ash elements (potassium, chlorine and sulphur).

Based on analysis of the collected particles with HRTEM/EDS/SAED techniques the following additional conclusions can be drawn;

- Two types of classic soot particles are formed during gasification of low ash content stem wood, fine soot particles with a primary particle size between 30–50 nm and large soot particles with a primary particle size between 100-300 nm. In addition to carbon, traces of metallic potassium could also be found in these particles.
- The concentration of ash forming elements significantly influences the type of individual particles formed during entrained flow gasification of biomass and both the shape and the microstructure of the individual particle was connected to its carbon and ash content.
- During gasification of high ash content bark, several types of particles could be identified following its concentration of carbon and ash forming elements, i.e., soot particles, graphite flakes, ash forming element dominated particles, zinc dominated particles and finally pure zinc particles.
- The results also indicates that zinc interacts in the formation of the soot particle creating a particle with a form and microstructure significant different from a classic soot particle.

References

Brink, A., Mueller, C., Kilpinen, P., and Hupa, M. 2000. Combustion and Flame, 123, pp. 275–279.

Bulirsch, R., and Stoer, J. 1966. Numerische Mathematik, 8, pp. 1–13.

Carlsson, P., Wiinikka, H., Marklund, M., Grönberg, C., Pettersson, E., Lidman, M., and Gebart, R. 2010a. Fuel, 89, pp. 4025–4034.

Carlsson, P., Marklund, M., Furusjö, E., Wiinikka, H., and Gebart, R. 2010b. TAPPI Journal, September, pp. 13–22.

Chen, Y., Shah, N., Huggins, F.E., and Huffman, G.P. 2005a. Environmental Science and Technology, 39, pp. 1144–1151.

Chen, Y., Shah, N., Huggins, F.E., Huffman, G.P. 2005b. Energy and Fuels, 19, pp. 1644–1651.

Golovitchev, V.I., Nordin, N., Jarnicki, R., and Chomiak, J. 2000. SAE Technical paper series, International spring fuels & lubricant meeting & exposition, January 2000.

Ishiguro, T., Takatori, Y., and Akihama, K. 1997. Combustion and Flame, 108, pp. 231–234.

Jones W.P., and Lindstedt, R.P. 1988. Combustion and Flame, 73, pp. 233-249.

Lockwood, F.C., and Shah, N.G. 1981. Proceedings of the Combustion Institute, 19, pp. 1405–1414.

Marklund, M. 2006. Pressurized Entrained-flow High Temperature Black Liquor Gasification. Ph.D Thesis. Luleå University of Technology.

Marklund, M., Tegman, R., and Gebart, R. 2007. Fuel, 86, pp. 1918–1926.

Marklund, M., Tegman, R., and Gebart, R. 2008. IFRF Combustion Journal, no. 200801.

Septien, S., Valin, S., Dupont, C., Peyrot, M., and Salvador, S. 2012. Fuel, pp. 202–210.

Valin, S., Cances, J., Castelli, P., and Thirey, S. 2009. Fuel, 88, pp. 834-842.

Weiland, F., Hedman, H., Marklund, M., Wiinikka, H., Öhrman, R., and Gebart, R. 2013. Energy and Fuels, 27, pp. 932–941.

Westbrook, C.K., and Dryer, F.L. 1981. Combustion Science and Technology, 1981, pp. 31–43.

4. Fuel particle conversion of pulverized biomass during pyrolysis in an entrained flow reactor

Entrained-flow gasification has several advantages, e.g. generation of syngas with negligible amount of tar content due to high operating temperature and it is easy to scale-up [1, 2]. Since biomass particles go through extremely high heating rate, gasification behaviour might be significantly different from that in other types of reactors. In addition, it is interesting to investigate how large biomass particle sizes can be in order to minimize the energy penalty due to milling fuel particles.

We investigated the effect of particle size on the yield of solid residue and morphological changes during the pyrolysis of biomass in an entrained flow reactor (LEFR). Experiments and particle simulation were employed for this purpose. With the particle simulation, the guideline of pyrolysis reactor design to achieve complete conversion for pyrolysis was provided for various reaction conditions.

4.1 Experimental methods

4.1.1 Sample

Sawdust of Norwegian spruce (stem wood) grown in Sweden was used as fuel. The sample was ground and sieved to three particle size ranges: 125–250μm, 250–500μm and 500–1000μm.

4.1.2 Experimental procedure

A laminar entrained flow reactor (LEFR) with an inner diameter of 50 mm and the length of 2 m was used to investigate the yield of permanent gases and solid residue by the pyrolysis of biomass particles at high heating rate. The LEFR was controlled at certain temperature (1073 and 1273 K) under atmospheric pressure. Around 10 g of biomass was fed by a bowl feeder at feeding rate of 0.1–0.6 g/min entrained with a primary N_2 flow rate of 1.0 L/min at a standard state. Secondary N_2 was also supplied from the top of the reactor with a flow rate of 4.0 L/min at a standard state. Reynolds number of the gas flow inside the reactor was 50–60. Biomass was pyrolyzed when it fell down through the reactor. Two different water-

cooled sample injectors were used to change the length of reaction zone inside the reactor to 650 and 1885 mm. Residence time of fuel particles were calculated numerically by considering density change during pyrolysis. At the bottom of the reactor, solid residue was collected by a flask and a thimble filter quenched by dry ice. The mass of collected solid residue was measured to determine its yield. The morphology of the solid residues was examined by a scanning electron microscope (SEM). The detail of the experimental methods by the L-EFR can be found elsewhere [3].

4.2 Particle model

4.2.1 Particle motion

In this study, the reaction conditions inside the LEFR were under the laminar flow regime according to the regimes presented in reference [4]. To calculate the slip velocity (difference between solid and gas flow speed) as well as residence time of particle, particle velocity and position was calculated along the axial direction by Eq. (1).

$$\frac{\pi}{6} D_p^3 \rho_p \frac{du_p}{dt} = \frac{\pi}{8} C_D \rho_g D_p^2 |u_g - u_p| (u_g - u_p) + \frac{\pi}{6} D_p^3 (\rho_p - \rho_g) g \quad (1)$$

Here, Schiller and Naumann's expression (applicable for Re_p<1000) was used for drag coefficient as shown Eq. (2).

$$C_D = \frac{24}{Re_p} (1 + 0.15 Re_p^{0.687}) \quad (2)$$

Carrier gas flow was assumed to be plug flow. The effect of pyrolysis gas on the gas flow rate and the effect of drag on the gas flow field were assumed to be negligible because of low particle density. Particles were assumed to be injected to the reaction area with the terminal velocity that was calculated from Eq. (1) under the sample injector's condition.

4.2.2 Heat transfer

Based on the assumption of local thermal equilibrium, energy balance inside the biomass particle at position r and time t can be written as shown in Eq. (3).

$$\rho C_p \frac{\partial T_p}{\partial t} = \lambda \left[\frac{\partial^2 T_p}{\partial r^2} + \frac{b-1}{r} \frac{\partial T_p}{\partial r} \right] + q_{pyro} \left(- \frac{d\rho}{dt} \right) \quad (3)$$

Mass conservation equation of gas phase inside the particle was ignored for the simplicity in this study. The initial conditions (0≤r≤R) were: Tp=300 K; ρ_b=ρ_{b0}; ρ_c=0. The boundary condition of the particle center (t≥0) is shown in Eq. (4).

$$\lambda \frac{\partial T_p}{\partial r} = 0 \tag{4}$$

The boundary condition on the surface ($t \geq 0$) was given by Eq. (5).

$$\lambda \frac{\partial T_s}{\partial r} = h\left(T_g - T_s\right) + \sigma\varepsilon\left(T_g^4 - T_s^4\right) \tag{5}$$

The density, specific heat and conductivities were calculated by the following interpolation equations.

$$\rho = \rho_b + \rho_c \tag{6}$$

$$C_p = \left(\rho_b C_{p,b} + \rho_c C_{p,c}\right)/\rho \tag{7}$$

$$\lambda = \left(\rho_b \lambda_b + \rho_c \lambda_c\right)/\rho \tag{8}$$

Heat transfer coefficient was calculated by Nusselt number (Nu=hD_p/λ) that was given by Eq. (9).

4.2.3 Pyrolysis kinetics

The total mass loss during pyrolysis of biomass at high heating rate can be expressed by a single first-order reaction model. The mass conservation of biomass and char can be expressed by Eqs. 10–12.

$$-\frac{d\rho_b}{dt} = -k\rho_b \tag{10}$$

$$\frac{d\rho_c}{dt} = \upsilon_c k\rho_b \tag{11}$$

$$k = Aexp(-E/RT) \tag{12}$$

The kinetic data of biomass pyrolysis was applied from the literature [5], which was obtained from the experiment with a wire mesh reactor at the heating rate of 200–10000 K/s with holding time at peak temperature of 0–1 s. Application of this literature data is appropriate because our particle model predicted that the local heating rate varies from 800 K/s to 10000 K/s.

4.2.4 Numerical solution

Differential equations were discretized by finite volume method and numerically solved by Crank-Nicolson method. The size of each cell was set as 1/100 of the particle radius, and time interval was 0.1 ms to minimize the numerical error. The physical and chemical properties used in the simulation are shown in Table 10.

Table 10. Physical and chemical properties used in the particle model.

Properties	Values	Sources
ρ_b (kg m^{-3})	440	[6]
ρ_c (kg m^{-3})	$\rho_b \times v_c$	-
$C_{p,b}$ (J kg^{-1} K^{-1})	1500+T	[7]
$C_{p,c}$ (J kg^{-1} K^{-1})	$420+2.09+6.85\times10^{-4}T^2$	[7]
λ_b (W m^{-1} K^{-1})	0.1256	[8]
λ_c (W m^{-1} K^{-1})	0.0837	[8]
v_c (-)	0.084	[5]
A (-)	1.1×10^4	[5]
E (kJ mol^{-1})	59.5	[5]

4.3 Results and discussion

4.3.1 Morphological change of fuel particles

In this section, the morphological change of fuel particles during pyrolysis is discussed. Fig. 24 shows the photograph of collected solid residues at the reaction temperature of 1273 K, 650 mm of the length of reaction zone and the initial particle size of 500–1000 μm. There was a variety in the degree of fuel conversion: unconverted, partially converted at the edge and fully converted. Here, the term, char, is used only for the fuel particles (solid residue) that completed pyrolysis, i.e. visually black. Other particles are called “fuel residue” to distinguish them from char. Fuel residues were slightly larger than the initial particles. It means that the biomass went through thermal expansion while heating. On the other hand, char particles were same size or smaller than initial particles. Some char particles were much smaller than the initial particle sizes due to the primary fragmentation as shown in the circle of Fig. 24. The detail of the primary fragmentation mechanism is discussed later.

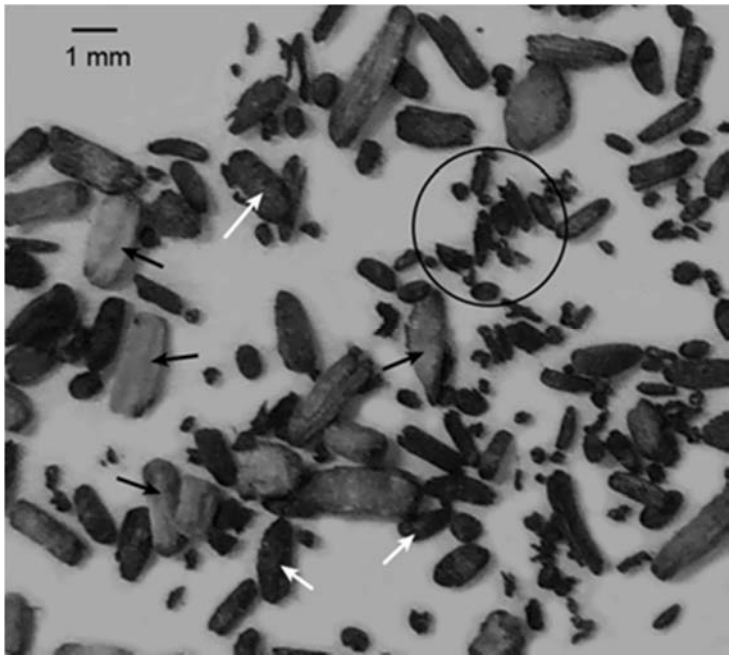

Figure 24. Photographs of solid residue (initial sample size: 500–1000 μm; reactor temperature: 1273 K; the length of reaction zone: 650 mm). Particles with black arrows are the examples of partially converted and unconverted particles. Particles with white arrows are the examples of fully converted particles.

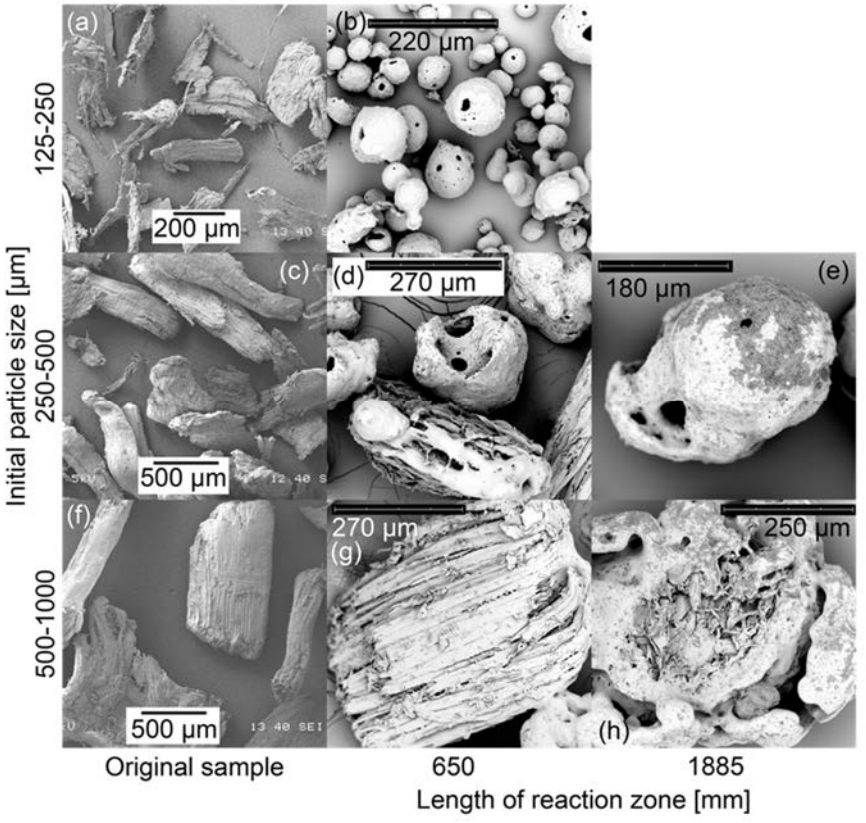

Figure 25. SEM images of original biomass particles and char particles at various reaction conditions.

Fig. 25 shows the SEM images of char particles obtained at the reaction temperature of 1273 K and original samples to examine their morphological transformation. Char generated from the initial particle size of 125–250 µm did not retain the initial structure of wood fibers even with short reaction time (Fig. 25(a)-(b)). It has nearly spherical shape (cenosphere) with a few large holes (~10–20 µm) and a lot of small holes (<10 µm). The transformation of char morphology into cenosphere particles have also been observed during the devolatilization of coking coals as a result of the plastic stage during which char particles behave as a Newtonian fluid [9]. Magnified image (Fig. 26a) shows that the small holes are located on the top of balloon-like bubbles, which means that the volatile vapors generated the holes when they were transferred from inside char particles to the gas phase [9, 10]. Some char particles were much smaller than the initial biomass (~50 µm) while others had comparable particle size with original fuel particles. Such small particles can be formed by the primary fragmentation of char particles. The primary fragmentation might have occurred by the shear stress from the gas flow or high

devolatilization rate during the plastic stage. Most of the char generated from the initial particle size of 500–1000 μm, on the other hand, retained the initial wood structure for the short reaction time (see Fig. 25(f)–(g)). The particle size of char was the same range with its initial size. Char generated with a short reaction time from the initial size of 250–500 μm consisted of three types of morphology: particles with initial wood structure; particles with cenosphere shape; and particles with partially smoothed wood fiber structure. When the residence time of particles increased, the particle morphology approached to those of smaller particles observed at shorter residence time as shown in Figs. 25 (e) and (h). Fig. 25(h) also shows that the outer shell of partially plasticized char particle was about to be torn off from non-plastic core, which indicates the progress of primary fragmentation.

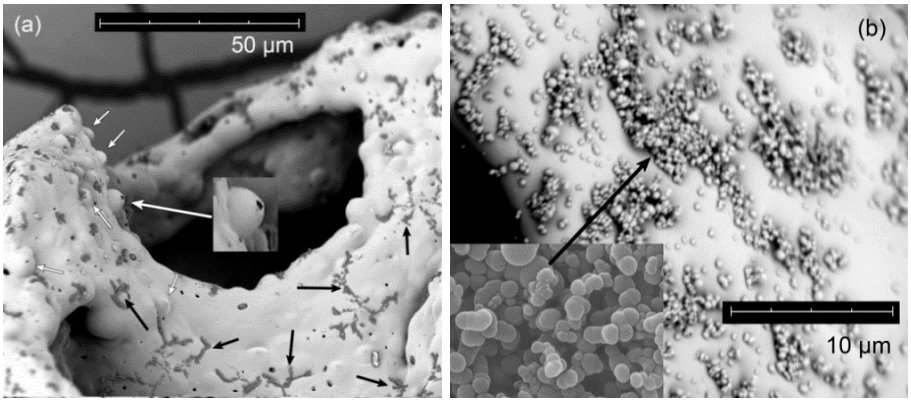

Figure 26. Magnified SEM images of char particles. (a) White arrows show the balloon-like bubbles (~10 μm) with small holes (~1 μm). Black arrows show the ash particles (K and Ca) deposited on the char surface with dendritic structure. (b) Spherical ash particles adsorbed on the char surface (Mg, Fe, K, Ca, Pt and S).

Two types of small grains were observed on the surface of char as shown in Fig. 26. Fig. 26(a) shows the dendritic structure observed on the surface of particle located center of Fig. 25(d), which SEM/EDX analyses showed mainly consist of K and Ca. Fig. 26(b) shows the spherical grains grown on the surface of char only at the reaction temperature of 1273 K and the reactor length of 1885 mm (Fig. 25 (e) and (h)). Spherical grains had the diameter of 0.1–1.0 μm. SEM/EDX analyses showed that the grains consist of mostly minerals such as Mg, Fe, K and Ca considering Pt as the coating material. This result indicates that the vaporized minerals were adsorbed on the surface of char particles because of the difference between solid and gas velocities.

From the observation above, we can conclude that biomass first swelled by thermal expansion, and then shrank during initial stage of pyrolysis. While char experienced the plastic stage during pyrolysis, volatiles that existed inside char particles were released outside the char particles due to its high internal pressure. At the same time, primary fragmentation of char particles occurred by the force

from the gas flow. The evidence of this primary fragmentation can be seen in Fig. 25 (h) in which the outer shell of partially plasticized char particle was about to be torn off from non-plastic core. This primary fragmentation was also reported on coal pyrolysis recently [11]. It seems ash forming elements released from the char particles to the gas-phase during or after this plastic stage. Because of the velocity difference between char particles and gas flow, these mineral elements were adsorbed on the surface of char later.

4.3.2 Fuel conversion

The effect of particle size on the fuel conversion is presented as the yield of solid residue from both experimental and simulation data in Fig. 27. The vertical lines show the screen sizes of sieves that were used for particle classification. For the particle size below 500 µm, there was no significant variation, and the experimental data and the prediction showed good agreement. For the particle size of 500–1000 µm, the yield of solid residue was considerably higher especially with short reactor length. At the same time, particle simulation showed the significant increase in the yield of solid residue. It means that there should be a large variability in fuel conversion in this range of particle size. In fact, variety of fuel conversion under this experimental condition was observed as shown in the photograph of collected solid residues (see Fig. 24). There is a tendency that bigger particle remained either as raw biomass or partial conversion such like torrefaction. The mean value of the prediction for the particle size of 500–1000 μm was calculated by Eq. 13 to compare with the experimental data. The mean value of the prediction showed good agreement with the experimental data, which enhances the validity of the particle simulation results. An important observation from Fig. 27 is the transition from complete to incomplete conversion when the particle size was increased.

$$\alpha_{mean} = \int_{500}^{1000} \alpha(D_p) \cdot f(D_p) dD_p \quad (13)$$

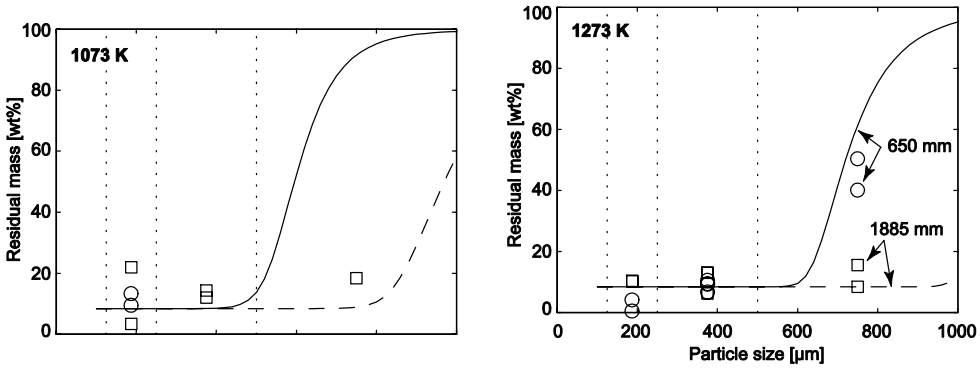

Figure 27. Particle size vs. residual mass ratio from biomass pyrolysis. Symbols represent experimental data from the entrained flow reactor and lines express the prediction by particle simulation. The vertical lines show the screen sizes of sieves that were used for particle classification.

Figure 28 shows the comparison of particle residence time in the reactor with the time required for 99% conversion (conversion time). Large particles need long conversion time but had short residence time compared with small particles. The cross-point of residence time and conversion time coincided with the maximum particle size to achieve high fuel conversion (see Fig. 27). As shown in Fig. 28, this critical particle size shifted to slightly larger when the reaction temperature increased from 1073 K to 1273 K due to shorter conversion time. However, it was affected more significantly by the length of reaction zone due to the residence time. Fuel conversion of biomass pyrolysis in an entrained flow reactor was eventually determined by the competition between the residence time and conversion time. Therefore, it is important to include the particle trajectory to predict the fuel conversion of biomass in an entrained flow reactor.

It is important to grind biomass particles small enough to be converted effectively. In practice, however, there will be an energy penalty to grind biomass particles to the efficiency of the whole biomass utilization process. Hence, to enhance the residence time by changing the reactor length in vertical direction is another option to improve the fuel conversion while keeping biomass particle size relatively large. Therefore, it is important for the design of thermochemical conversion process of pulverized biomass to consider the variation of biomass particle size and the reactor length to optimize the overall efficiency, investment and operation cost. The quantitative data of the effect of particle size on fuel conversion presented in this study is essential information for the design of reactors, choice of particle size distribution of the biomass feedstock, and optimization studies of the whole system by process integration technique and techno-economic analysis.

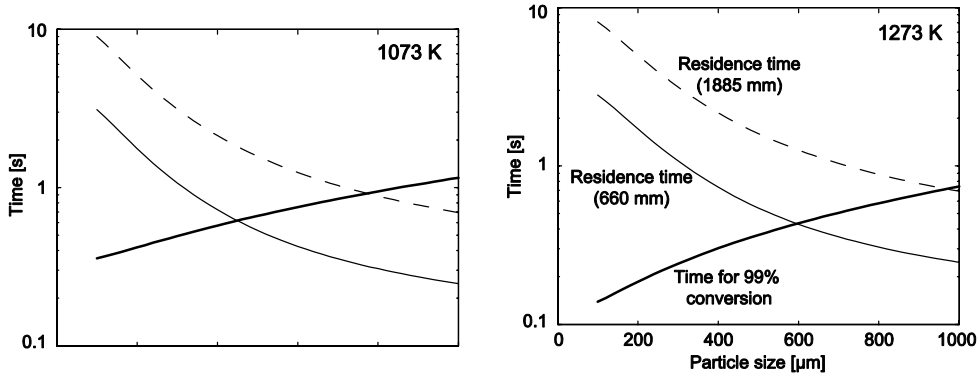

Figure 28. Comparison of residence time to time for 99% conversion during pyrolysis at various reaction temperature and particle size.

Fig. 29 shows the fuel conversion and the travel distance of particles from the sample injection position as functions of time. When the reactor temperature was increased, the fuel conversion was accelerated. However, it hardly affected the particle trajectory of large particles (1.0 mm of diameter) before fuel conversion while the particle velocity of small particle was slightly accelerated by increasing temperature. When the gas velocity was increased, the particle velocity was increased while fuel conversion was not affected. Particle size affected both fuel conversion and trajectory. The smaller particles were, the faster it was converted and the slower it fell down inside the reactor.

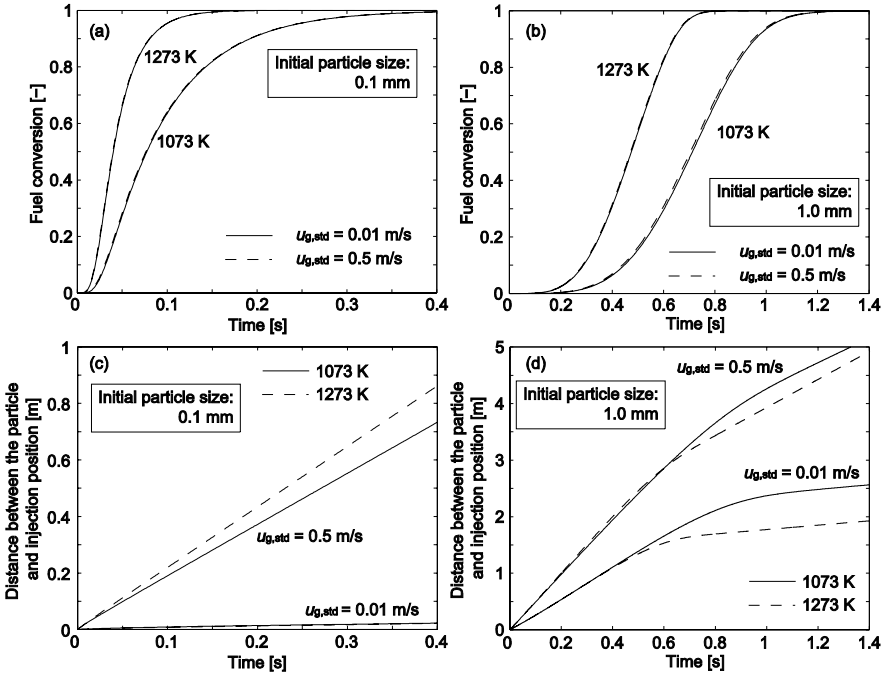

Figure 29. Fuel conversion and travel distance of particles from the sample injection position as a function of time. (a) and (c) Initial particle size of 0.1 mm. (b) and (d) Initial particle size of 1.0 mm.

Although we investigated the intra-particle heat transfer effect, all the state-of-the-art computational fluid dynamics (CFD) simulation models have ignored intra-particle transport phenomena (mass/heat transfer) to our knowledge. To clarify the importance of intra-particle heat transfer, we also carried out the particle simulation under the assumption of isothermal particle as shown in Eq. 14, and compared with the particle model described in section 4.2. Fig. 30 shows shows how much errors are imposed for the prediction of overall conversion by using isothermal particle assumption instead of non-isothermal particles. This result shows that the isothermal particle assumption, commonly applied in the CFD simulation, is valid only for small particle size (typically up to 150–250 μm in diameter).

$$\rho_p V_p c_p \frac{dT_p}{dt} = hA_p\left(T_g - T_p\right) + \left(-\frac{d\rho_p}{dt}\right) V_p H_{dev} \tag{14}$$

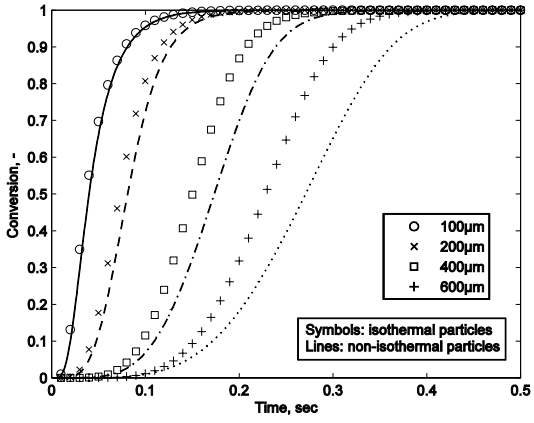

Figure 30. The effect of fuel size on devolatilization (free-falling biomass at T=1273 K with 1bar of N_2). Isothermal particle model (symboles; Eq. 14) was compared with non-isothermal models (lines; section 4.2) for particle conversion vs. time.

4.4 Conclusions

During pyrolysis, biomass first swelled by thermal expansion, and then shrank during initial stage of pyrolysis. While char experienced the plastic stage during pyrolysis, volatiles that existed inside char particles were released outside the char particles due to its high internal pressure. At the same time, primary fragmentation of char particles occurred by the force from the gas flow. Ash forming elements was first released from the char particles to the gas-phase, and then adsorbed on the surface of char.

Incomplete pyrolysis conversion of biomass was observed for the particle size of 500–1000 µm with the short reaction zone (650 mm). The particle simulation successfully predicted transition of high fuel conversion of biomass particle to low conversion quantitatively. Particle simulation showed that the fuel conversion in an entrained flow reactor depended on the competition between residence time and the time required for the pyrolysis.

Finally, the significance of intra-particle heat transfer effect on the overall fuel conversion was investigated. Fuel conversion can be successfully predicted without considering intra-particle heat transfer for the particle size below 200 µm.

References

[1] Higman, C.; van der Burgt, M. Gasification. Elsevier Science, Amsterdam 2003.

[2] Zhang, Y.; Kajitani, S.; Ashizawa, M.; Oki, Y. Tar destruction and coke formation during rapid pyrolysis and gasification of biomass in a drop-tube furnace. Fuel 2010, 89, 302–309.

[3] Zhang, L.; Binner, E.; Chen, L.; Qiao, Y.; Li, C.-Z.; Bhattacharya, S.; Ninomiya, Y. Experimental Investigation of the Combustion of Bituminous Coal in Air and O_2 /CO_2 Mixtures: 1. Particle Imaging of the Combustion of Coal and Char. Energy Fuels 2010, 24, 4803–4811.

[4] Flaxman, R.J.; Hallett, W.L.H. Flow and particle heating in an entrained flow reactor. Fuel 1987, 66, 607–611

[5] Stubington, J.F.; Aiman, S. Pyrolysis Kinetics of Bagasse at High Heating Rates. Fuel 1994, 194–203.

[6] Francescato, V.; Antonini, E.; Bergomi, L.Z. Wood Fuels Handbook. Italian Agriforestry Energy Association, Legnaro 2008.

[7] Bellais, M.; Davidsson, K.O.; Liliedahl, T.; Sjöström, K.; Pettersson, J.B.C. Pyrolysis of large wood particles: a study of shrinkage importance in simulations. Fuel 2003, 82, 1541–1548.

[8] Pyle, D.L.; Zaror, C.A. Heat transfer and kinetics in the low temperature pyrolysis of solids. Chem. Eng. Sci. 1984, 39, 147–158.

[9] Yu, J.; Lucas, J.A.; Wall, T.F. Formation of the structure of chars during devolatilization of pulverized coal and its thermoproperties: A review. Prog. Energ. Comb. Sci. 2007, 33, 135–170.

[10] Jarvis, M.W.; Haas, T.J.; Donohoe, B.S.; Daily, J.W.; Gaston, K.R.; Frederick, W.J.; Nimlos, M.R. Elucidation of Biomass Pyrolysis Products Using a

Laminar Entrained Flow Reactor and Char Particle Imaging. Energy Fuels 2010, 24, 324–336.

[11] Senneca, O.; Urciuolo, M.; Chirone, R.; Cumbo, D. An experimental study of fragmentation of coals during fast pyrolysis at high temperature and pressure. Fuel 2011, 90, 2931–2938.

5. Fuel conversion characteristics of black liquor and pyrolysis oil mixture for efficient catalytic gasification

Char gasification often represents rate limiting step, and important to understand kinetics properly. Investigation was carried out to elaborate the possibility of scaling up black liquor gasification by mixing with pyrolysis oil. As part of technological feasibility assessment, char gasification reactivity of black liquor and pyrolysis oil mixture at various mixing ratio was measured in an isothermal thermogravimetric analyser, and compared with that of pure black liquor.

5.1 Methods

5.1.1 Experimental setup

Both char preparation (pyrolysis) and char gasification experiments were carried out with an isothermal thermogravimetric analyser (iTGA) as shown in Figure 31. The iTGA is a vertical cylindrical reactor with a diameter of 100 mm. The length of the electrically heated reaction zone is 450 mm. Biomass/char sample can be kept in the reaction zone hanging from a precision scale with a nickel-chromium wire. The atmosphere of the reaction zone can be controlled by a continuous gas flow from the bottom of the reactor. Biomass sample can be kept in a cooling zone with nitrogen flow after the experiment to avoid further oxidation.

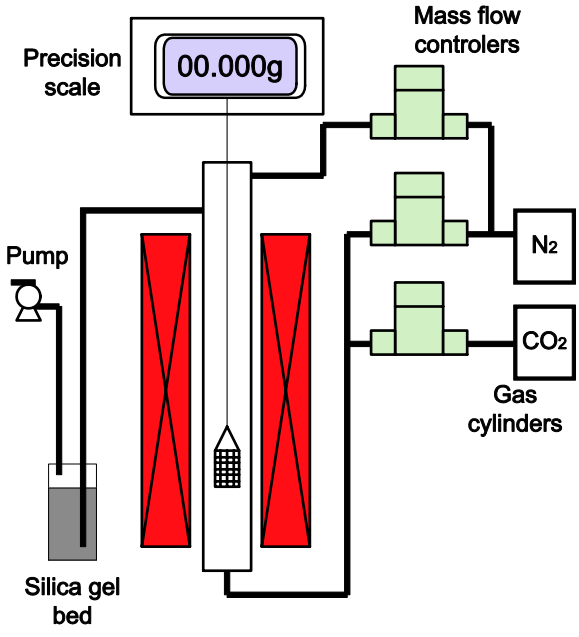

Figure 31. Schematic diagram of isothermal TGA.

5.1.2 Sample preparation

We used black liquor (BL), pyrolysis oil (PO) and their mixtures (with PO accounting for 20% and 30% on weight basis), denoted BP20 and BP30. BL and PO samples were used as received from the Smurfit Kappa Kraftliner mill (Piteå, Sweden) and the VTT pyrolysis pilot plant (Espoo, Finland), respectively. BP20 and BP30 were prepared in a beaker on a heated plate (363 K) for 10 minutes with a liquid mixer. Table 11 shows the properties of the black liquor and pyrolysis oil. BL contains about a third of ash while PO contains negligible amounts of ash.

Our preliminary experiments showed higher reactivity of char particles when samples were pyrolyzed with CO_2 flow instead of N_2. However, CO_2 atmosphere may result in partial char conversion at high temperature, so a moderately low pyrolysis temperature (813 K) was chosen. Liquid samples (ca 1 g) were held in an alumina crucible and pyrolyzed. The product from pyrolysis was a char cenosphere with a diameter larger than 10 mm. To minimize the effect of mass transfer on the apparent char reactivity, we prepared char samples prior to the gasification tests and ground them followed by sieving to isolate a fraction with particle size from 200 to 300 µm.

Although these conditions do not fully mimic the gasification of biomass particles in entrained-flow gasifiers, char reactivity obtained in this study may represent the qualitative behaviour of char gasification. The fact that considerable experience is available from pilot scale gasification of BL makes it possible to use BL as

a reference to which the behaviour of the other samples is compared. However, the quantitative values of char reactivity in realistic condition of industrial gasifiers (higher temperature, higher heating rate, different gas composition and in-situ char gasification) might be higher than those obtained in this study.

Char morphology and alkali distribution were investigated by scanning electron microscope (SEM), model: JSM-6460LV by JEOL, with energy-dispersive X-ray spectroscopy (EDS), model: 7574 by Oxford Instruments.

Table 11. Fuel properties of raw samples. BL: black liquor; PO: pyrolysis *oil. n.a.: not analysed*

	PO	**BL**
Moisture, wt.% , w.b.	26.3	27.2
Combustible, wt.% , w.b.	n.a.	33.3
Ash content, wt.% , w.b.	n.a.	39.5
HHV, MJ/kg, w.b.	16.7	9.23
C, wt.%, d.b.	39.7	30.6
H, wt.%, d.b.	7.70	3.40
N, wt.%, d.b.	0.10	0.08
S, wt.%, d.b.	<0.01	5.10
Cl, wt.%, d.b.	<50 ppm	0.16
K, wt.%, d.b.	n.a.	3.24
Na, wt.%, d.b.	n.a.	21.6
O (diff.), wt%, d.b.	52.5	35.8

5.1.3 Experimental procedures and data treatment

Prior to the experiments, the reaction zone was heated to the desired temperature (993–1133K) and filled with reaction atmosphere (from 10 to 100 vol.% of CO_2 with N_2 balance at total pressure of 1 bar). Char sample (~100 mg) was held in a platinum wire-mesh basket with a diameter of 15 mm, and kept in the cooling zone. The sample basket was then moved to the reaction zone by lowering the wire. Temporal mass of the sample basket was recorded in a PC every two seconds during the experiments. After the sample stopped losing its mass (i.e. sample completed char gasification), the sample basket was extracted from the reaction zone and then quenched in the cooling zone. Each experiment was repeated between 2 and 5 times in order to estimate reproducibility.

First, noise in the recorded mass signal was removed by a lowpass digital Butterworth filter. Thereafter, each mass loss curve was standardized to char conversion according to Equation 1

$$X = \frac{m_0 - m}{m_0 - m*} \quad (1)$$

Here, m, m_0 and m_* represent temporal, initial and final mass of sample. Reproducibility of the experiments was evaluated by the standard deviation of parameters estimated from repeated experiments. A pooled variance s_p involving all experimental conditions was calculated by Equation 2. For char conversion, we assumed constant absolute variability while constant relative variability was used for conversion rate and kinetic parameters. Hence, s_i in Equation 2 can represent either a relative or an absolute standard deviation.

$$s_p^2 = \frac{\sum(n_i-1)s_i^2}{\sum(n_i-1)} \quad (2)$$

5.2 Results and discussion

5.2.1 Char morphology

Figure 32 shows the char morphology of the examined samples. The scale at the bottom of each SEM image is 10 µm. It is apparent that PO char had a smooth surface while other chars (i.e. BL, BP20 and BP30) had many small particles on the char surfaces. SEM/EDX analyses showed that these small particles were finely dispersed Na salts particles. The fine catalyst dispersion suggests high char gasification reactivity of BP20 and BP30, which was experimentally confirmed later.

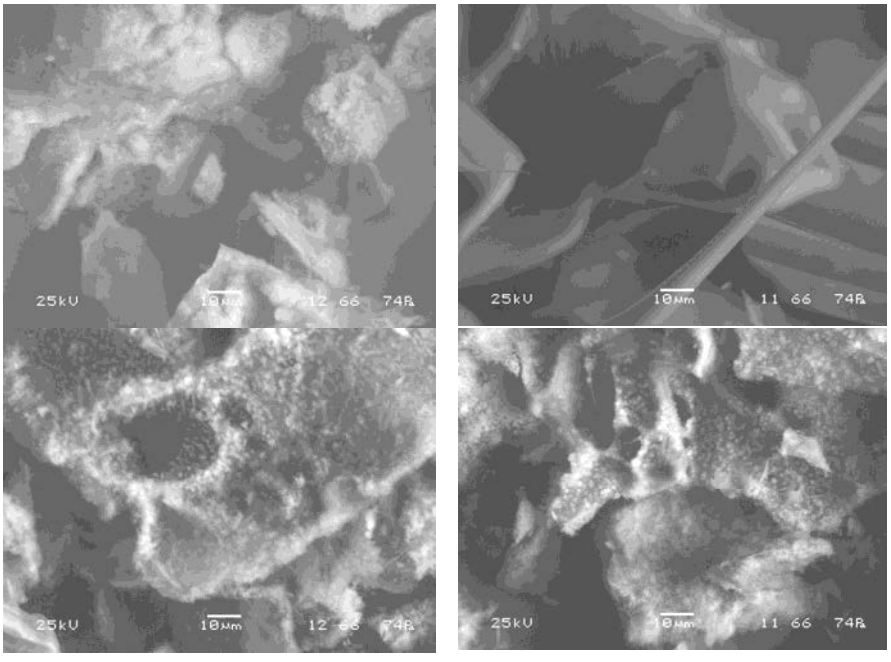

Figure 32. SEM images of char: (top-left) black liquor (BL); (top-right) pyrolysis oil (PO); (down-left) BP20; (down-right) BP30.

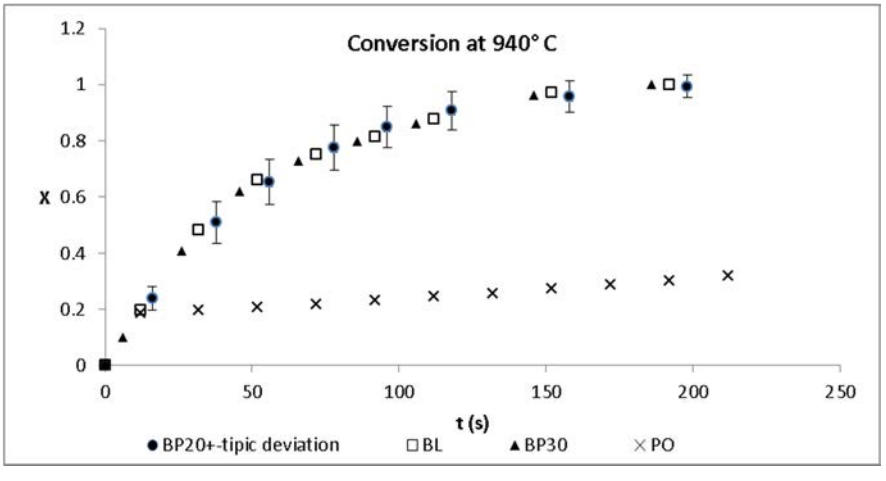

Figure 33. Char conversion vs. gasification time of Black liquor (BL), pyrolysis oil (PO), and their mixtures (BP20 and BP30) at T=940 °C and PCO2=1 bar.

5.2.2 Comparison of char reactivity

Figure 33 is the plot of char conversion against reaction time. There was no statistically significant difference in char conversion behaviour among black liquor and mixture of black liquor and pyrolysis oil (BP20 and BP30).

5.2.3 Model

Conversion rate of char gasification is usually expressed as the product of two functions: the rate coefficient, *k*(p,T), determined by the reaction conditions, and a structural function, *f*(X), dependent on char conversion, *X*,

$$r = \frac{dX}{dt} = k(p,T) \cdot f(X) \tag{3}$$

We applied Arrhenius equation for rate coefficient and random pore model (RPM) for structural char parameters. Char reaction takes place on the surface of the particles. Char particles are porous, and typically, the internal surface of a char particle is of an order of magnitude 1000 times larger than the external surface22. Therefore *f*(*X*) is controlled by pore development. RPM explains the dynamics of char conversion rate, *f*(*X*), considering that pore surface grows as conversion proceeds. RPM has been successfully applied to model conversion rate of biomass chars. The structural function of RPM, *f*(*X*), is shown in Equations 4 and 5.

$$f(X) = (1-X)\sqrt{1-\psi ln(1-X)} \tag{4}$$

$$\psi = \frac{4\pi L_0(1-\varepsilon_0)}{S_0} \tag{5}$$

The structural parameter, ψ, determines the pore surface growth due to the consumption of carbon. L_0 is the initial average length of the pores while ε_0 and S_0 represent the initial porosity and surface area respectively.

The Arrhenius expression (Equation 6) can then be introduced to model temperature dependent kinetics. A modification including a reference temperature was used to reduce the sensitivity of the pre-exponential factor to small changes in the activation energy. A regression analysis was used to estimate the parameters of the Arrhenius equation.

$$k = Ae^{-\frac{E_a}{R}\left(\frac{1}{T}-\frac{1}{T_{ref}}\right)} \tag{6}$$

Table 12 shows the parameters estimated from the least square method. These parameters had reasonable agreement with previous kinetic studies of black liquor at lower temperature ranges

Table 12. Kinetic parameters for the CO2 gasification of BL, BP20 and BP30 char.

	A (s^{-1} kPa^{-n})	n	E (kJ/mol)	T_{ref} (K)	Ψ
BL	1.96×10^{-3}	0.37	144.7	1183	1.22
BP20	1.30×10^{-3}	0.42	160.3	1183	2.11

5.3 Conclusions

Both mixed samples, BP20 and BP30, showed high reactivity, not significantly different from that of BL, implying strong catalytic activity of alkali from BL in the mixtures. Char reactivities of BL, BP20 and BP30 were significantly higher than those for other types of biomass. Char reactivity determined for BL was slightly higher than that from extrapolation of a previous study at lower temperatures.

The random pore model with Arrhenius equation was found to fit the dynamics of char conversion in CO2 well. In summary, the results indicate that the black liquor gasification process may also be used for mixture of pyrolysis oil and black liquor without major modification.

Chapter 3

Thermochemical equilibrium modelling of slagging behaviour in pressurised entrained-flow gasification of woody biomass

Charlie Ma[1], Marcus Öhman[1] and Rainer Backman[2]
[1] Luleå University of Technology, Sweden
[2] Umeå University, Sweden

Contents

Thermochemical equilibrium modelling of slagging behaviour in pressurised entrained-flow gasification of woody biomass

1. Introduction

During pressurised entrained-flow gasification (PEFG) of woody biomass feedstock, inorganic elements comprising the fuel can react between themselves as well as with organic material to result in the formation of ash. Such ash materials have an effect upon the gasification process and can interfere with the immediate operation of the reactor; e.g., plugging of the outlet. Hence, there is a need to predict the behaviour of the ash, and in particular, the formation of melt and particles that can adhere to the reactor wall. Global thermodynamic equilibrium calculations have been undertaken to predict the phases that could be formed during PEFG of stem wood and a bark fuel. Based on these results, the viscosities of the oxide melt components were then predicted using a slag viscosity model. Scenarios depicting the firing of the fuels alone and with kaolinite and olivine additives have been investigated. Some of the thermochemical equilibrium modelling results are compared with experimental characterisation results of deposits collected from inside a pilot-scale PEFG reactor firing these woody biomasses. The deposits were characterised by their elemental compositions, and for the bark fuel, the crystalline phase composition also. The results serve as a basis for discussion regarding the slag formation process that occurs during PEFG of woody biomass, as well as highlighting the need for modelling refinements in order to realise the prospect of improving slag behaviour.

2. Method

2.1 Fuel compositions

The main inorganic elements in woody biomasses are, inclusive of natural contaminant minerals due to harvesting processes, Na, Mg, Al, Si, P, S, Cl, K, Ca, Mn, Fe (Werkelin, 2008). While it is possible to consider all these main ash-forming elements in the thermochemical equilibrium calculations, some omissions are necessary to reduce complexity and to facilitate the observation of succinct trends. P is relatively very low in woody biomass and thermodynamic data with regards to its solid and liquid phases remains in need of experimental data (Lindberg, Backman, Chartrand, & Hupa, 2011). Hence, it is omitted from the calculations in this study. Mn and Fe are also omitted due to their low contents. It is noted, however, that the omitted elements may play a significant role in determining crucial slag melt properties; e.g., viscosity, surface tension.

Two woody biomass fuels were used in the pilot-scale experimental campaigns and their compositions as given in Table 1. They were also used as inputs for the thermochemical equilibrium calculations. They are based upon actual stem wood and bark fuels commercially-available in Sweden (Glommersträsk and Mönsterås, respectively). The wood fuel was comprised of stem wood from pine trees, while the bark was from spruce trees. The former conformed to the typical composition of stem wood while the latter contained significantly elevated levels of Si, Al and Na compared to typical bark (Werkelin, 2008). This was likely due to harvesting or timber treatment processes that led to the inclusion of soil minerals; i.e., feldspars and quartz.

Table 1. Composition of fuels and oxidant (oxygen).

g/kg dry fuel	Wood	Bark
Na	0.015	0.431
Mg	0.187	0.79
Al	0.026	1.106
Si	0.079	4.808
S	0.06	0.33
Cl	0.045	0.119
K	0.357	2.034
Ca	0.736	8.719
C	509	522
H	63	56
N	1	4.1
O	424	375
H_2O	49.32	82.25
O_2 oxidant	501.23	511.06
Inorganics (wt%)	0.14	1.73

2.2 Additives

Since the composition and quantity of woody biomass ash-forming elements are generally significant less than that of coal, an additive such as kaolinite ($Al_2Si_2O_5(OH)_4$) or olivine ($(Mg,Fe)_2SiO_4$ ≈ 49.8 wt% MgO, 8.5 wt% FeO, 41.7 wt% SiO_2) could be necessary in order to provide adequate slag for wall coverage. These compounds were chosen based on their contrasting behaviour within oxide slags; i.e., Al_2O_3 and SiO_2 are considered to raise slag viscosities, while MgO and FeO are regarded as slag fluxing. Both kaolinite and olivine additives are readily available resources that can be acquired for experimentation. The phase distributions were observed as functions of increasing kaolinite and olivine inclusion, from 0–20 wt% of the respective fuels, at increments of 0.02 wt%; i.e., 1001 calculations. This interval was chosen because coal PEFG typically uses fuels with such levels of ash-forming matter. The viscosities based upon the resultant melt compositions were obtained from the MS Excel toolbox created by Duchesne et al. (Duchesne, Bronsch, Hughes, & Masset, 2013). The slag viscosity model involves an artificial neural network algorithm developed by Duchesne et al. (Duchesne, Macchi, Lu, Hughes, McCalden, & Anthony, 2010) using the composition of the slag melt and the temperature.

2.3 Thermochemical equilibrium modelling

2.3.1 Global reactor conditions

The temperature was varied from 1000–2500 °C for the calculations representing the firing of the fuels without additives to cover the likely temperature range from the flame region (hottest) to the reactor wall (coolest). This interval was divided into 1°C increments; i.e., 1501 calculations, so that relatively sharp elemental phase transitions could be captured. The calculations representing the inclusion of additives were carried out at 1000 °C, 1200 °C, 1400 °C, 1600 °C and 1800 °C to cover the approximate temperature range of the reactor wall. For the two aforementioned calculation scenarios with and without additives, absolute pressures were set at 2 bar, 10 bar and 80. 2 bar was the pressure employed during campaigns with the pilot-scale reactor at the ETC (described later), while 10 bar is the maximum pressurisation of this reactor. 80 bar represents the approximate syngas pressure necessary for methanol synthesis. The air-to-fuel ratio λ was chosen to be 0.35 and the oxidant was pure O_2 for all calculations.

2.3.2 Calculation tool and thermodynamic databases

The thermochemical equilibrium phase compositions were obtained by utilisation of the Equilib module of the FactSage 6.4 package (Bale, o.a., 2009) (Bale, o.a., 2002) with the accompanying thermodynamic databases. For the global calculations without additive and those involving addition of kaolinite, the solution database SLAGD (FToxid) was chosen to evaluate potential oxide melts with dissolved CO_2, since a relatively high CO_2 partial pressure may prevail inside the reactor. For the calculations involving olivine additive, SLAGE (FToxid) was chosen to account for Fe in the slag, while also considering the solubility of H_2O, another abundant gaseous species during gasification. OlivA (FToxid) was also selected to account for the potential stabilisation of olivine crystal group species. MELTA (FTpulp) was additionally selected in every calculation set to account for the potential formation of salt mixture melts.

2.3.3 Limitations and scope

The calculations contained herein are based upon global thermochemical equilibrium. This treats the reactor as an ideal constant closed system in which the fuel, additive and oxidant interact. This assumption does not materialise in practice as it would require all elements in the system to be available for interaction with each other at constant conditions with an infinite duration for reaction. In reality, some elements are bound to non-reactive compounds or are kinetically- or physically-restricted such that they are effectively rendered unavailable for reaction. Conditions during the PEFG process are also unstable and spatially heterogeneous. Coupled with relatively short residence times, all of these factors mean that global

thermochemical equilibrium cannot be reached. Crystalline phases that can co-exist in equilibrium with the melt phase were not considered for the viscosity calculations, since the thermochemical equilibrium calculations cannot predict the size, shape and locations of these solids. Due to these difficulties and as yet unascertained process characteristics, the results from these calculations serve only as a first indicator of what phases could be present during PEFG. There also remains a need for critical evaluation and optimisation of oxide systems that are highly relevant for woody biomass; e.g., SiO_2-K_2O-CaO (Lindberg, Backman, Chartrand, & Hupa, 2011). Nonetheless, it is of interest to observe the outcomes derivable from currently available models and thermodynamic databases. The focus is specifically on the formation of oxide melts and their viscosity behaviour. In regards to the latter, the chosen viscosity model was recently developed using data from a wide range of slag viscosities and compositions. While it has been reported to be superior to most other earlier models, not all compositions derived from the thermochemical equilibrium calculations may fall within the range, so considerable errors can arise. By complementing with future experimental analyses, these results may enable a degree of elucidation of the ash behaviours that occur during the PEFG process as well as revealing necessary refinements to existing models.

2.4 Experimental facility and deposit characterisation

The slag formation/behaviour has been studied in an enriched oxygen-blown pilot-scale entrained-flow gasifier (1 MW_{th}) located at the ETC in Piteå, Sweden. The facility and operating procedure details are found in Weiland et al. (Weiland, Hedman, Marklund, Wiinikka, Öhrman, & Gebart, 2013) and the details of the wood- and bark-fired campaigns are found in Ma et al. (Ma, Weiland, Hedman, Boström, Backman, & Öhman, 2013). The reactor ash deposit sampling method is also discussed in the latter. Figure 1 shows a schematic of the reactor with the location of the reactor ash deposit sampling probe shown in the middle-left. Two separate experimental campaigns were conducted with the wood and bark fuels with compositions as given in Table 1. Ash deposits were collected from the inside of the reactor during each campaign. These samples were characterised by scanning electron microscopy (SEM) equipped with energy-dispersive spectroscopy (EDS) to reveal elemental composition. Based on these results, the viscosities of the oxide melt components were then predicted through utilization of a recently developed slag viscosity model. For the bark campaign, X-ray diffractometry (XRD) was also utilised for crystalline phase identification.

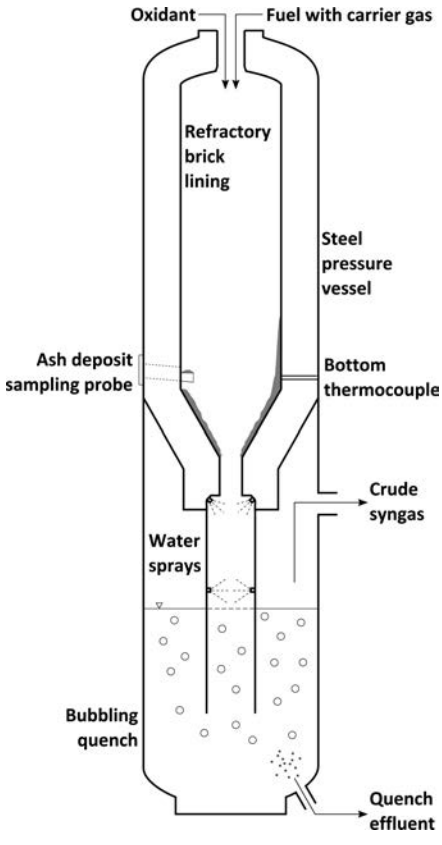

Figure 1. Schematic of PEFG reactor indicating location of ash deposit collection probe and thermocouple.

3. Results

3.1 Global thermochemical equilibrium calculations – no additives

K, Ca and Si are the most abundant ash-forming elements for both fuels and they have a crucial role in determining the ash-forming behaviour. Hence, their phase distributions are shown for the scenario where the fuels are fired without an additive. The plots are labelled with major distinct solid and gas phases in approximate orders of decreasing quantity. They are only coarse quantitative indicators, since their distributions vary along the curves.

Figure 2 and 3 show the K distribution as a function of temperature for the wood and bark fuels, respectively. A greater amount of K is present within the oxide melt for the bark fuel as compared to the wood fuel across the temperature range. Generally, the incorporation of K in the slag phase increases with pressure but decreases with temperature. Also when the temperature is relatively low, the amount of CO_2 dissolved with the oxide melt increases with pressure. KOH is the dominant gaseous K phase at low temperatures; however, monoatomic gaseous K becomes dominant with increasing temperature. It is also apparent that K can only be stabilised in a condensed phase within the silicate-based oxide melt.

Figure 4 and 5 show the distribution of Ca for the wood and bark fuels, respectively. The stronger dependence upon pressure for the wood fuel is clear; i.e., the amounts of Ca in the oxide melt increases with pressure, while for bark, the effect of pressure is relatively negligible. Also for the wood fuel, there is a sharp transition from α'-larnite to hatrurite at 1300 °C for both 2 bar and 10 bar conditions as indicated by the broken black vertical line. The crystalline phases are predominately CaO and Ca-silicates, and they exist up to approximately 2000 °C and 1500°C for wood and bark fuels, respectively. Conversely, the presence of gaseous Ca species is 1500 °C and 2000 °C for the wood and bark fuels, respectively. Also, given the higher level of Ca in the bark fuel and the significant presence of Ca in the slag phase, the amounts of slag from the bark fuel is much greater than the wood fuel.

Figure 6 and 7 show the distribution of Si for the wood and bark fuels, respectively. As for Ca, the pressure-dependence for the wood fuel is apparent; i.e., the amounts of Si in the oxide melt increases with pressure. Also, as before for the wood fuel, there is a sharp transition from α'-larnite to hatrurite at 1300 °C for both

2 and 10 bar conditions as indicated by the broken black vertical line. The Si distribution of the bark fuel mirrors that of the Ca distribution and they combine to form stable crystalline Ca-silicates when the temperature is < 1500 °C. Both the wood and bark fuels show the presence of gaseous SiO at temperatures > 1900 °C. The higher level of Si in the bark fuel combined with the significant presence of Si in the slag phase again emphasises the greater amounts of slag compared to the wood fuel.

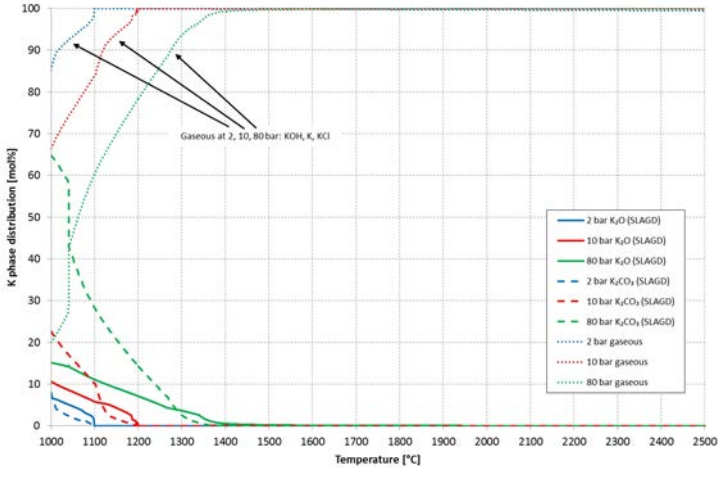

Figure 2. Wood fuel: distribution of K.

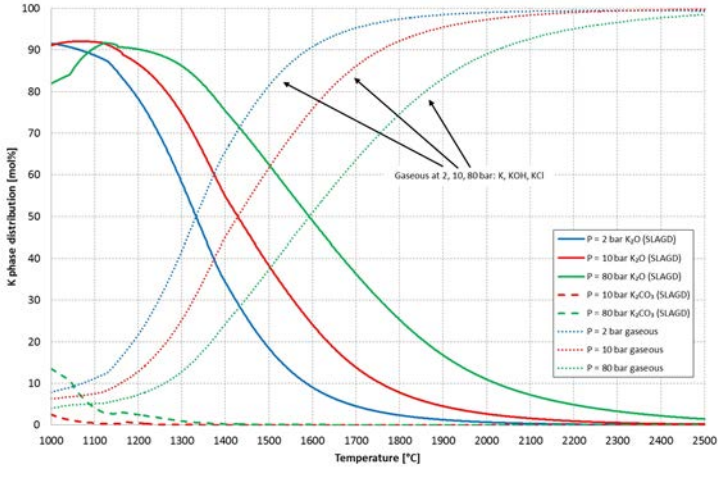

Figure 3. Bark fuel: distribution of K.

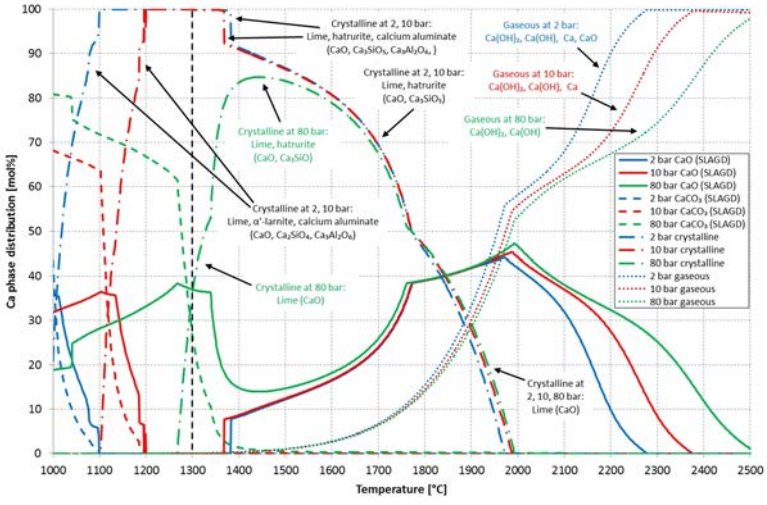

Figure 4. Wood fuel: distribution of Ca.

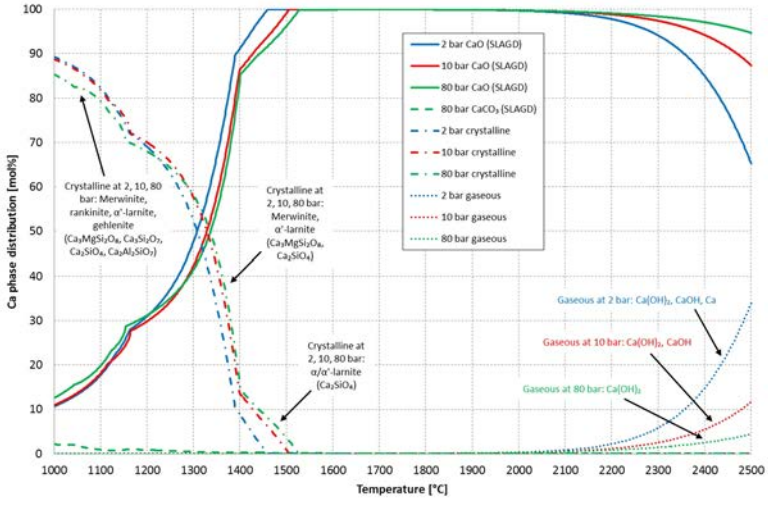

Figure 5. Bark fuel: distribution of Ca.

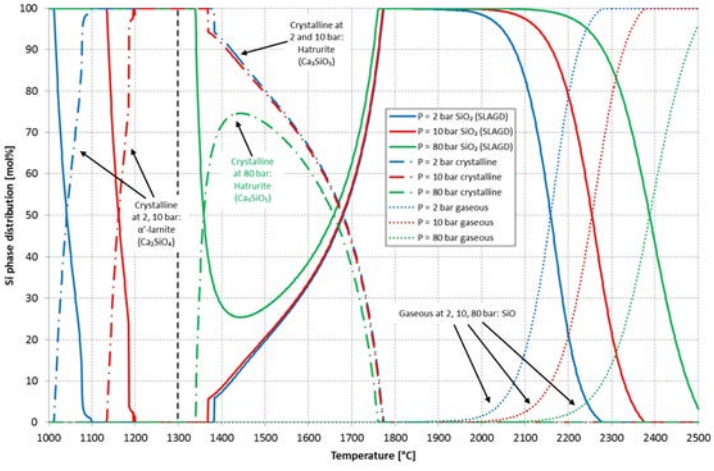

Figure 6. Wood fuel: distribution of Si.

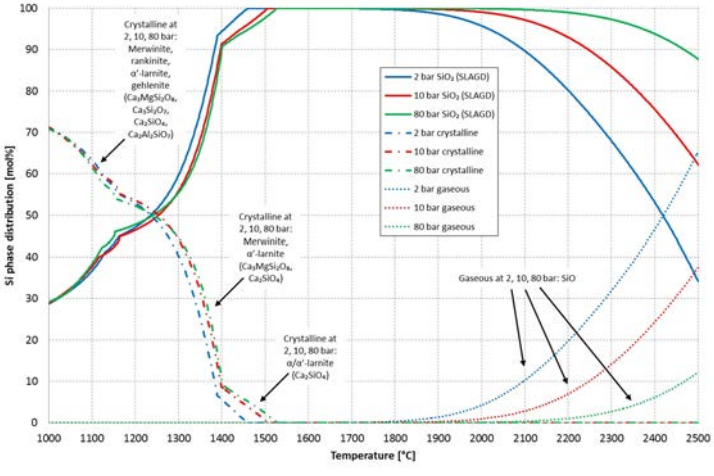

Figure 7. Bark fuel: distribution of Si.

3.2 Experimental characterisation of reactor deposits

Figure 8 and 9 show the backscattered electron (BSE) image from the SEM-EDS analyses of the deposits collected from inside the ETC reactor during PEFG of wood and bark, respectively. These images, as well as more detailed discussions about the analyses and results, are found in Ma et al. (Ma, Weiland, Hedman, Boström, Backman, & Öhman, 2013). The wood deposit, Figure 8, contained a relatively extensive coverage of branched crystals (main feature labelled on figure) that may have derived from the cooling of a melt high in Si, Al and Ca. Towards

the centre top, a molten structure rich in Si, Al, K, and Ca can be seen. These K-rich features were not observed as frequently as the aforementioned branched crystals. The bark campaign yielded loosely sintered ash aggregates; a typical example is shown as Figure 9. Aggregates were observed to consist of a possible melt component that embedded particles of sand and feldspars to varying degrees, with alkaline-silicates lying on the peripheries of the aggregates. The composition of melt showed consistency between different particles and often the aggregate outlines were similar to that of the embedded quartz particle. Asides from common biomass fuel contaminants such as quartz (sand) and feldspars (albite, microcline), the semi-quantitative XRD analysis of the bark deposit indicated the dominance of the crystalline phases by alkaline-silicates (åkermanite, wollastonite, merwinite, 39 wt%). These are likely found on the peripheries of the aggregates as indicated. Leucite was also detected at a quite high level (22 wt%). An amorphous background observed from the XRD analysis is presumably due to the melt component.

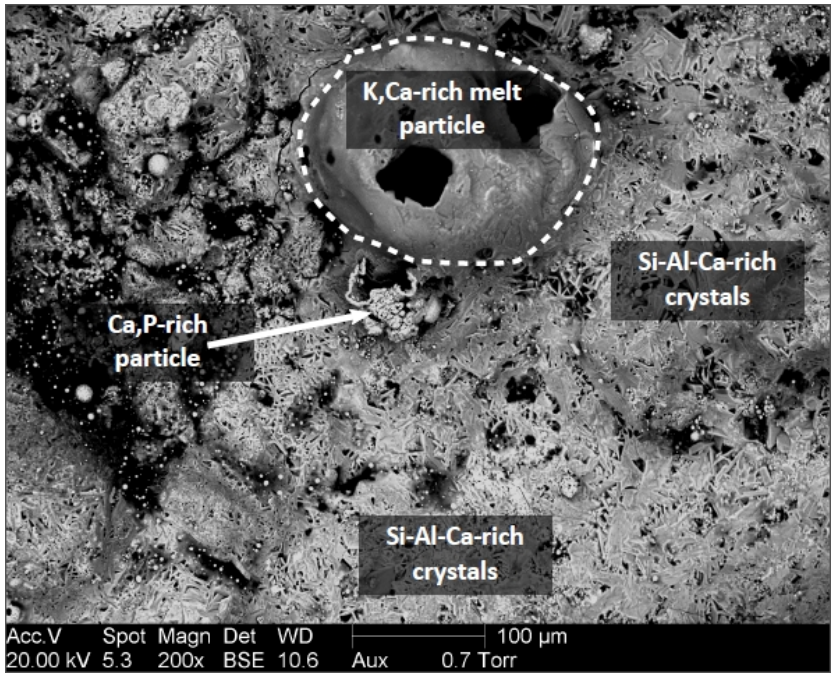

Figure 8. Wood fuel: SEM-BSE image of deposit collected upon reactor ash probe.

The major inorganic elemental distributions in the deposits are compared with each respective fuel in Figure 10. The coverage of Si-Al-Ca branched crystals was taken for the wood case, while the bulk ash deposit composition from the bark fuel was obtained by SEM-EDS of crushed specimens. For the wood deposit, the

share of Al and Si are enriched compared to the fuel, while K and Ca are reduced. The reason for the former could be due to the unintended detection of the underlying mullite-based probe used to collect the deposit, or reactions between the ash-forming elements in the fuel and the ceramic lining in the hot reactor. Nonetheless, accounting for this the level of Si in the deposit was still enriched compared to the fuel ash. The bark deposit also exhibited enrichment in the share of Si while reduction in Ca as the most obvious differences. The levels of the other elements are relatively similar except for S and Cl, which are depleted from the deposit. S, Cl and K are also depleted for the wood case.

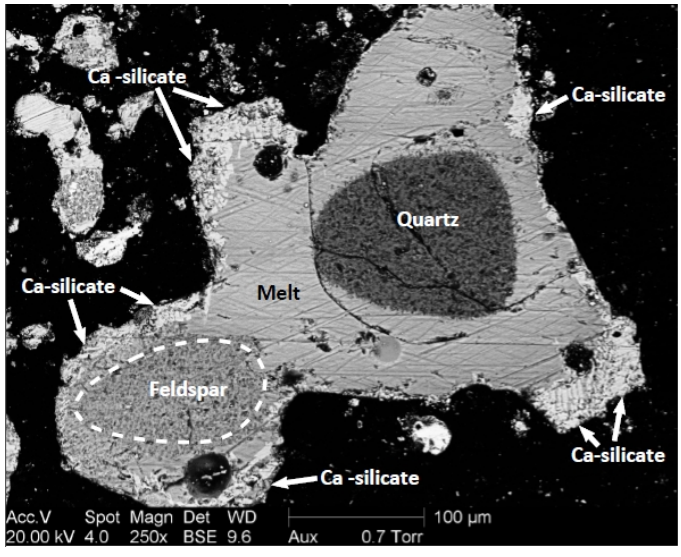

Figure 9. Bark fuel: SEM-BSE image of deposit collected upon reactor ash probe.

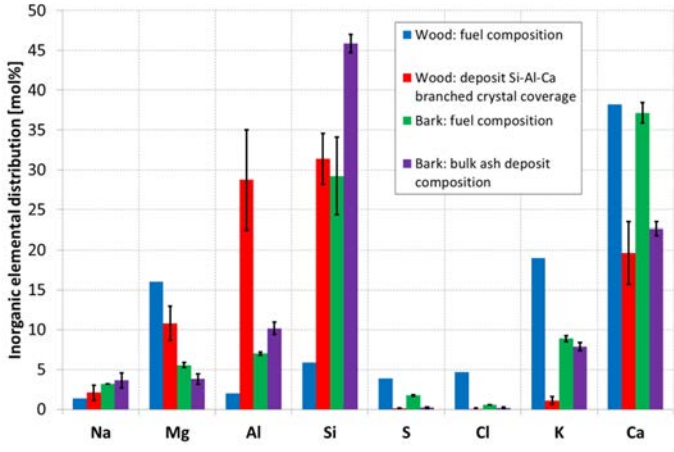

Figure 10. Comparison between major inorganic elements of fuels and bulk ash deposit compositions.

3.3 Comparison between thermochemical equilibrium modelling and experimental results

Figure 11 compares the composition of the Si-Ca-Al branched crystal coverage of the wood fuel deposit with the slag composition as predicted by thermochemical equilibrium calculations. Treating the carbonate components as oxide equivalents, the thermodynamic model predicts Ca as the dominant element, whereas Si was by far the dominant element from the SEM-EDS analysis. Furthermore, no slag phase is predicted by the model in the vicinity of the maximum temperature as recorded by a thermocouple placed near to the reactor wall, which can be considered as an estimate of the deposit temperature. It must also be pointed out that the predicted composition has excess Ca for use in the viscosity model, which may render it a particularly poor estimate. The predicted viscosity for the Si-Al-Ca coverage based on the SEM-EDS analysis is approximately 35 Pa.s at the maximum near-wall temperature. This means it could have flowed readily and possibly explains its relatively extensive coverage. By contrast, the viscosity of the Si-Al-K-Ca molten structure is predicted to be up to one order-of-magnitude higher than the Si-Al-Ca coverage across the temperature range, despite the relatively high level of K and a more molten appearance. The composition based on thermochemical equilibrium calculations is predicted to have an even lower viscosity, probably due the high level of Ca. Figure 12 compares the composition of the melt component from the bark ash deposit aggregate with the slag composition as predicted by thermochemical equilibrium calculations. The predicted composition is somewhat better than for the wood fuel, though Si is also calculated to be lower than that measured by SEM-EDS. The predicted viscosity of the bark aggregate melt component is approximately 4000 Pa.s, a relatively high value which may

explain why there is no widespread agglomeration or significant slag formation. The thermochemical equilibrium is predicted to have a lower viscosity, again probably due to the high level of Ca predicted.

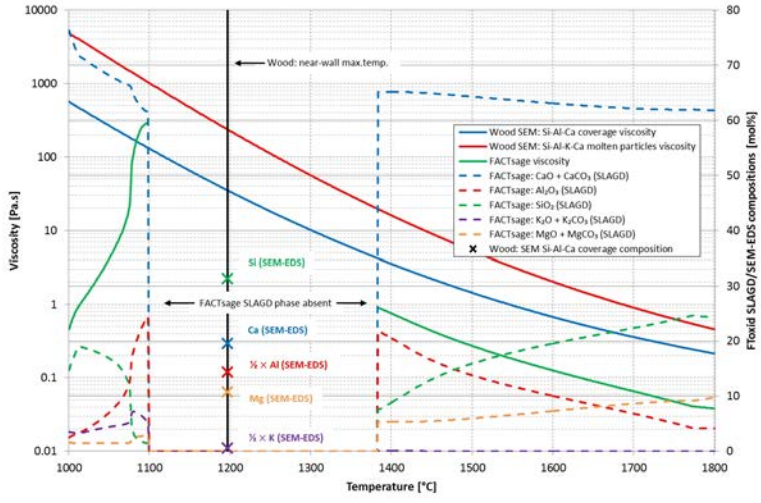

Figure 11. Wood: comparison between possible melt component identified from SEM-EDS and thermochemical equilibrium calculation results, along with modelled viscosity.

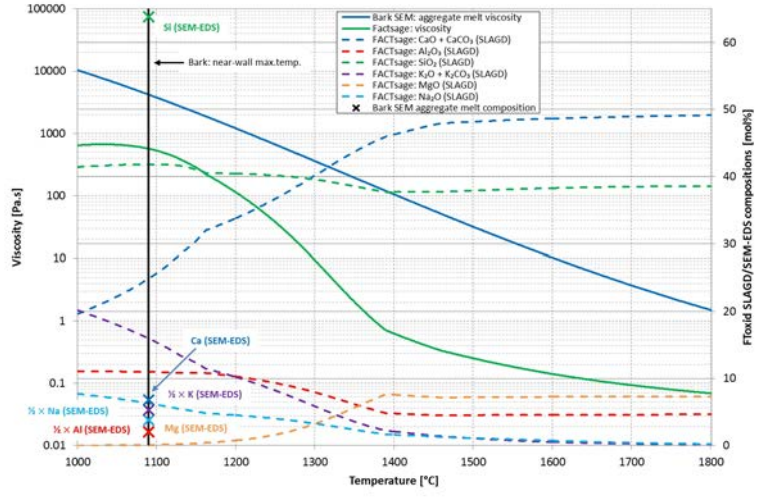

Figure 12. Bark: comparison between possible melt component identified from SEM-EDS and thermochemical equilibrium calculation results, along with modelled viscosity.

3.4 Global thermochemical equilibrium with kaolinite additive

Figure 13 and 14 show the oxide melt phase amounts as the quantity of kaolinite additive is increased from 0–20 wt% fuel for the wood and bark fuels, respectively. The amounts have been normalised by the total mass of inorganic elements represented as oxides (Na_2O, MgO, Al_2O_3, SiO_2, SO_3, K_2O, CaO); i.e.,

$$\text{y-axis} = \frac{\text{Mass of calculated slag phase}}{\text{Theoretical maximum mass of inorganic oxides}} \times 100 \quad (1)$$

Tentatively, the ratio above represents the slag formation potentials at the different conditions; i.e., stabilisation of inorganic elements in a slag phase. The major phases comprising the remaining inorganic elements not stabilised within the slag are labelled along the curves. This has been carried out to highlight the stability of crystalline phases that can pose problems with predicting viscosities due to crystallisation and/or the presence of solid particles. It is noted that the viscosity toolbox developed by Duchesne et al. (Duchesne, Bronsch, Hughes, & Masset, 2013) facilities the inclusion of both crystalline and solid particles; however, this component was not incorporated for this study due to the lack of knowledge about possible crystalline shapes and sizes. Pressure is considered only to affect the composition of the melt, with no direct physical effect upon the viscosity.

For the wood fuel at the lower temperatures, an increase in the kaolinite additive generally stabilises more crystalline phases. At higher temperatures, the additive components (Al_2O_3, SiO_2) are stabilised within the slag more readily. For the bark fuel, there is greater formation of oxide melts. For both fuels, the effect of pressure upon the melt composition and quantity is relatively insignificant. Also, as the amount of kaolinite additive increases, the stable crystalline phases shift from Ca-silicates to K- and Ca-aluminosilicates, and with further addition, to aluminosilicates.

Figure 15 and 16 show the viscosities of the oxide melt phases as a function of kaolinite additive at various temperatures and pressures for the wood and bark fuels, respectively. In the occurrence of oxide slag phases Na_2CO_3, $MgCO_3$, K_2CO_3 and/or $CaCO_3$, they were inputted as additional oxides Na_2O, MgO, K_2O and CaO, respectively, into the viscosity model. This was done because the latter are formalisms output by the software, even though the CO_3^{2-} anion may not be associated with particular cations. There is an absence of the slag phase for the compositions involving wood fuel at 1000 °C. Table 2 is an indicative guide of the flow characteristics at different viscosity values.

Table 2. Viscosity and flow characteristics.

Flow characteristic	Viscosity [Pa.s]
Onset of sintering	10^9–10^{10}
Moderate sintering	10^7–10^9
Rapid sintering	10^5–10^7
Non-flowing slag	10^3–10^5
Slow moving slag	100–1000
Flow slag (coal PEFG)	25

The viscosity magnitudes and trends are similar for both the wood and bark fuel scenarios, though the latter is generally approximately one order-of-magnitude lower. An increase in the viscosity is observed as the amount of kaolinite additive is added. The viscosities tend to be within the slow or non-flowing and sintering regimes, unless the temperature is > 1400°C. At 1600°C and above, the viscosity can drop well below the desired viscosity of slags during PEFG of coal. This is likely due to Ca exhibiting transition in stability from anorthite to the slag phase with increasing temperature.

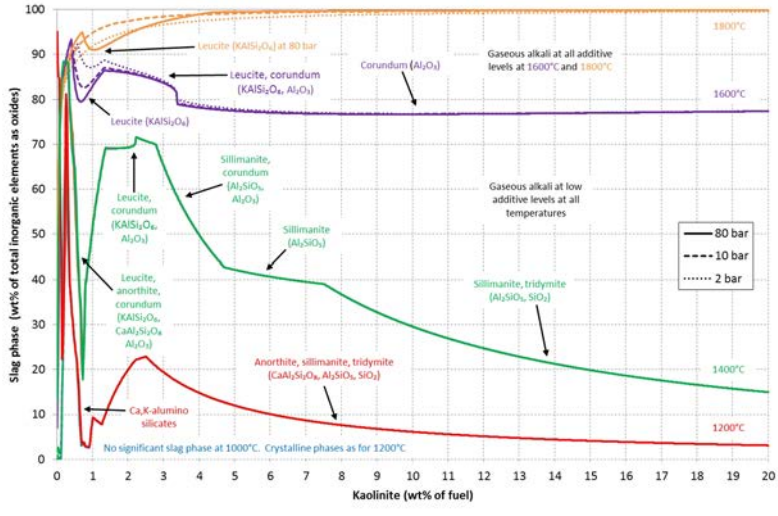

Figure 13. Wood: amount of oxide melt and major crystalline phases with kaolinite additive.

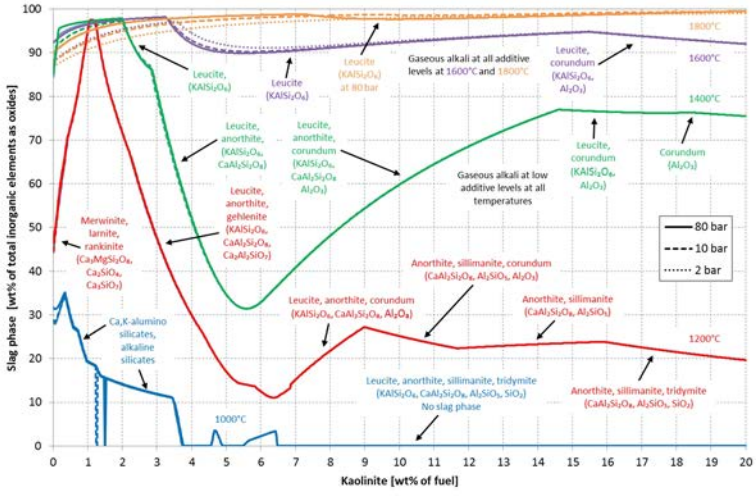

Figure 14. Bark: amount of oxide melt and major crystalline phases with kaolinite additive.

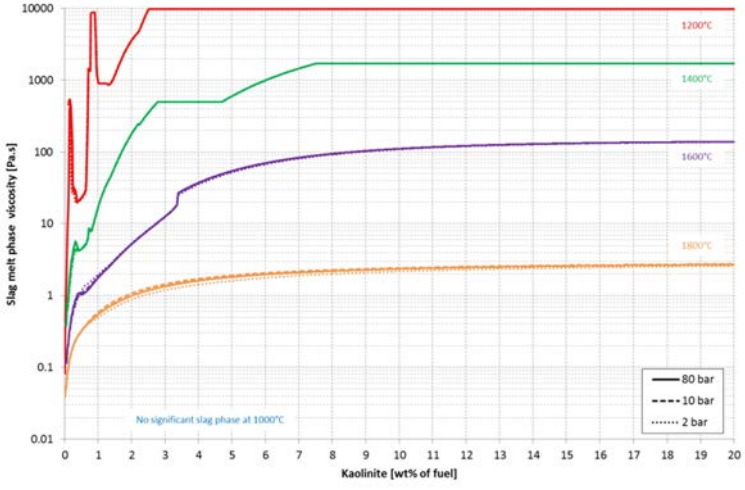

Figure 15. Wood: viscosity of melt with kaolinite additive.

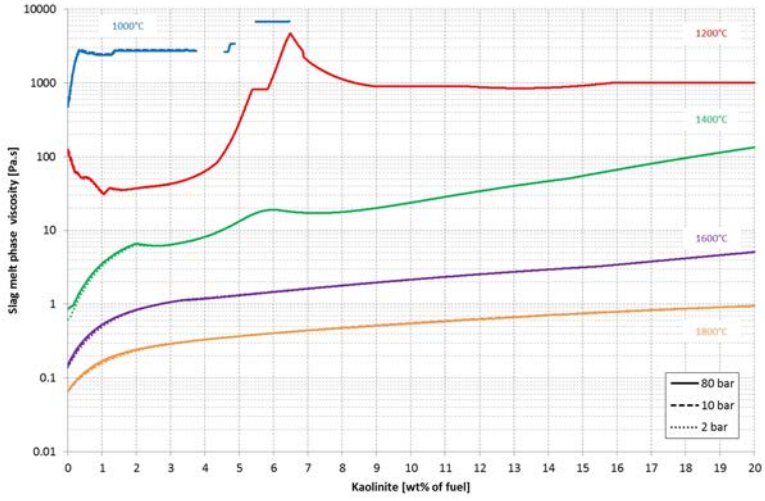

Figure 16. Bark: viscosity of melt with kaolinite additive.

3.5 Global thermochemical equilibrium with olivine additive

Figure 17 and 18 show the oxide melt phase amount as the quantity of olivine additive is increased from 0–20 wt% fuel for the wood and bark fuels, respectively, with normalisation according to the previously de-scribed ratio (with FeO added to denominator). As before, this ratio tentatively indicates the slag formation potentials at the different conditions. The major phases comprising the remaining inorganic elements not stabilised within the slag are again labelled along the curves. For the wood fuel at the lower temperatures, an increase in the olivine additive generally stabilises more crystalline phases. At higher temperatures, the additive components (MgO, FeO, SiO_2) are stabilised within the slag more readily. For the bark fuel, there is greater formation of oxide melts. For both fuels, the effect of pressure is relatively insignificant except at the higher temperatures. As the additive increases, the stable crystalline phases shift from mainly alkaline-oxides and/or -silicates to olivine group phases (forsterite, olivine, monticellite). Compared to the scenario with kaolinite additive, the formation of melt is significantly lower for all temperatures and pressures. This is mainly due to the dominating stability of the olivine group phases.

Figure 19 and 20 show the viscosities of the oxide melt phases as a function of olivine additive at various temperatures and pressures for the wood and bark fuels, respectively. In the occurrence of oxide slag phases $Mg(OH)_2$, $Ca(OH)_2$, NaOH, $Fe(OH)_2$ and/or $Fe(OH)_3$, they were inputted as additional oxides MgO, CaO, Na_2O, FeO and Fe_2O_3, respectively, into the viscosity model. Similar to the kaolinite scenario, the large differences in viscosity due to temperature are contrasted by the similarities at different pressures; i.e., composition does not vary

significantly with pressure. The broken dotted red line in Figure 19 is due to the absence of the slag phase for certain compositions at the conditions (1200 °C, 2 bar). The large changes between 5–9 wt% fuel of olivine addition at the conditions at 1400 °C (2 bar and 10 bar) coincide with the incorporation of SiO_2 into the slag with simultaneous reduction of FeO, CaO and MgO. This occurrence is also responsible for the abrupt changes at 1600°C and 80 bar between approximately 12–17 wt% of fuel olivine addition. In general, though, the viscosities do not exhibit variations as significant as those of the kaolinite scenario as the amount of additive increases. Additionally, the viscosities are significantly lower with olivine as the additive. However, the flow characteristics are still mainly in the slow and non-flowing regime for temperatures < 1400 °C. The viscosity magnitudes and trends are similar for both the wood and bark fuel scenarios.

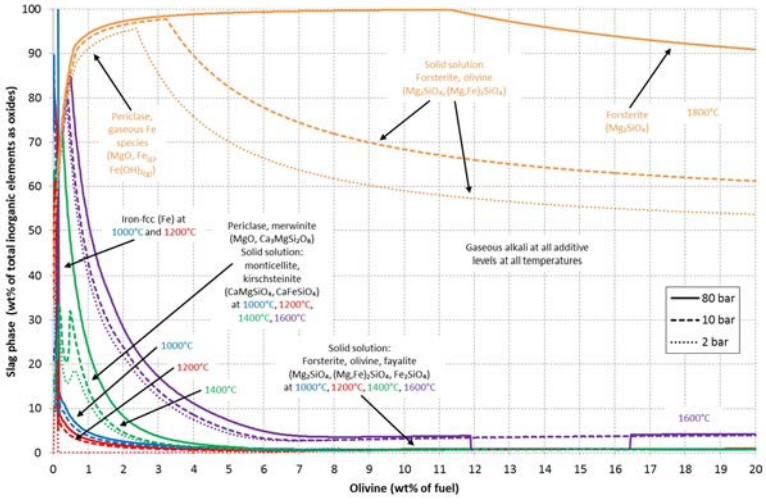

Figure 17. Wood: amount of oxide melt and major crystalline phases with olivine additive.

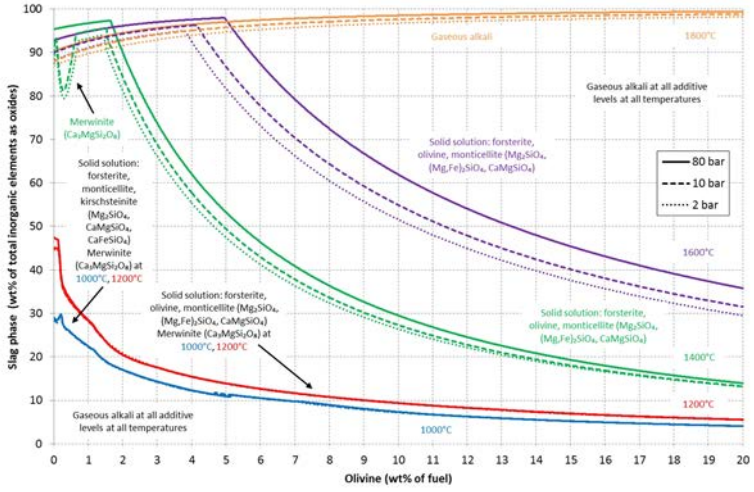

Figure 18. Bark: amount of oxide melt and major crystalline phases with olivine additive.

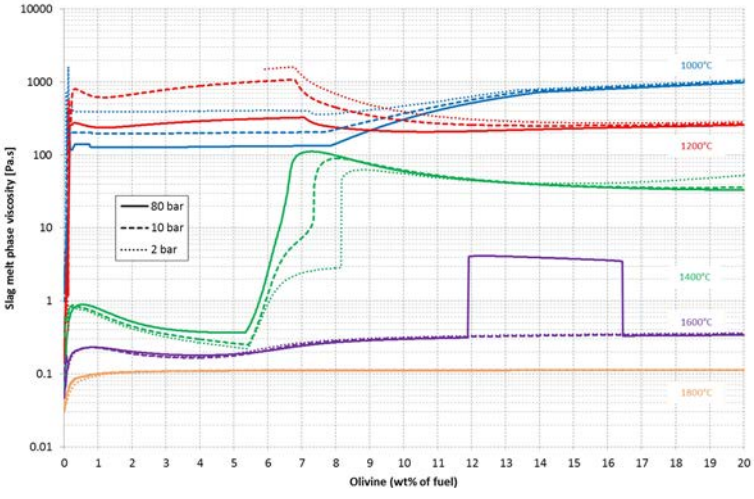

Figure 19. Wood: viscosity of melt with olivine additive.

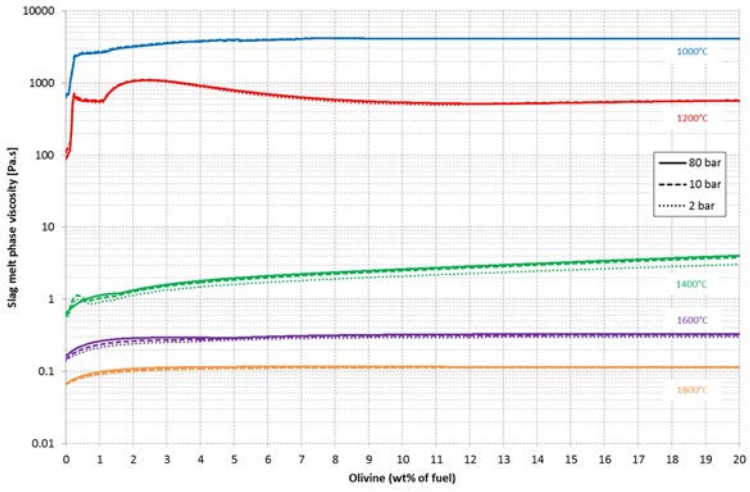

Figure 20. Bark: viscosity of melt with olivine additive.

4. Discussion

The major difference between the wood and bark fuels from the results of the thermochemical equilibrium calculations is the amounts of K, Ca and Si comprising the oxide melt with increasing temperature. The greater amount of oxide melt for the bark fuel could be due to the greater amounts of Si and Al. Practically, this could mean that the slagging tendency of the bark fuel is greater. It must, however, be noted that the composition of the bark is not typical of a pure bark fuel; the levels of Si, Al and Na are exceptionally high, which is consistent with the inclusion of soil minerals. The most consistent and clearest trend exhibited by the comparisons between the ash deposits with both the original fuel ash compositions (Figure 10) and the melt compositions derived from thermochemical equilibrium calculations (Figure 11 and 12) is that Si is enriched and Ca is diminished in the actual deposits. This difference may reflect the stickiness of Si-rich deposits that could have rendered this preferential collection. Ca could be released as sub-micron CaO particles that can leave the reactor if there are no significant reactions with Si. However, reactivity could be enhanced if either or both Ca and Si are gaseous coming from the flame region, which are shown to be stable species at very high temperatures. This may also be applicable to K, except K is significantly more likely to be released gaseously even at much lower temperatures. With this in mind, the components of the aggregates collected from the bark campaign indicate possible initiation of a sticky silicate layer by reaction between Si-rich particles and gaseous K before adhesion and interaction with Ca-containing particles. These aggregates also demonstrate clearly that localised reactions occur upon Si-rich particles, which limit the applicability of global thermochemical equilibrium assumptions. More discussion regarding the ash deposits can be found in Ma et al. (Ma, Weiland, Hedman, Boström, Backman, & Öhman, 2013). Another important factor is that though the relative degree of K volatility is higher for the wood fuel, the much higher level of K in the bark may imply that both have deleterious effects for certain reactor wall refractories (Scudeller, Longo, & Varela, 1998). Because of this, and the fact that woody biomasses generally contain low levels of ash, it is likely that an additive is needed to allow steady removal of ash deposits as well as formation of a protective layer for gasifier refractories.

When kaolinite is the additive, the viscosity model indicates that increasing amounts of additive would require higher operating temperatures to reduce viscosity to acceptable values (15–25 Pa.s). This is in agreement with the premise that

Al_2O_3 and SiO_2 serve as network-forming components that raise slag viscosities. Maintaining homogeneity in the mixing of fuel and additive would then be important for controlling the viscosity. Operation of the reactor in a predominantly non-slagging mode at relatively low temperature < 1400 °C does not appear to be possible. Although all or almost all K may be captured within leucite, the small amounts of high viscosity slag contacting the wall may pose problems by accumulating in the reactor. The presence of crystalline phases at the lower temperatures (1000–1400 °C) in equilibrium with the melt components can also cause large increases in the viscosity as compared to the melt viscosities shown. The higher levels of alkali and alkaline metals in the bark fuel appears to stabilise greater formations of oxide melt at temperatures < 1600 °C when kaolinite additive is present, thereby also lowering the viscosity substantially compared to the wood fuel. The results from the viscosity model are therefore also concordant with the premise that CaO, K_2O and MgO are generally slag fluxing. The solubilities of water vapour and CO_2 into the oxide slag may also cause changes to the viscosity, though they are not of high levels. Pressure does not seem to change the composition of the composition of the oxide melt significant for most scenarios. In fact, pressure seems to only affect phase compositions when Si content is low; i.e., in the wood fuel. This could be due to the fact that condensed phases (more prominent when Si is abundant) are less prone to be affected by pressure.

Olivine appears less prone to slag formation than kaolinite due to the stability of olivine group crystal phases. Practically, this could mean that olivine added to the process would not interact even if given long residence times during adherence upon the reactor wall. Furthermore, the similarities in viscosities of the melts that are formed from both fuels indicate that neither fuel ash compositions interact significantly with the olivine with respect to slag formation. In order words, slag formation is predominately restricted to the olivine additive itself. Because of this, the volatility of K is also higher, compared to the kaolinite scenario. For these reasons, olivine appears less attractive as an ash control additive.

Given the relevance of equilibrium conditions for molten deposits that may have extended residence times upon the reactor wall, neither kaolinite nor olivine additives exhibit ideal behaviour in terms of viscosity behaviour or amount of melt formed at equilibrium conditions. An alternative could be phosphorus-based additives, which have been observed to be highly reactive towards the main ash-forming elements Ca, Mg and K (Grimm, Skoglund, Boström, & Öhman, 2011). Low temperature eutectics can be formed, which are also possibly miscible with silicate melts. This could lower the melting temperature of the latter (Lindberg, Backman, Chartrand, & Hupa, 2011) and in turn may also lower the viscosity.

The viscosity model developed by Duchesne et al. (Duchesne, Macchi, Lu, Hughes, McCalden, & Anthony, 2010) utilised for this study can account for crystalline and solid particle inclusions. This can prove valuable in woody biomass slags that are likely to contain soil minerals and high levels of Ca that can induce crystallisation readily. Moreover, datasets of slags relevant to those formed during PEFG of woody biomass can be used as training sets to offer better predictions if

they are known in the future. Hence, it is necessary to assess its suitability in handling such slags.

Finally, as mentioned previously, none of the thermochemical equilibrium calculation results herein are intended to accurately represent actual phase compositions during PEFG. Physical characteristics pertaining to the operation of the reactor as well as chemical kinetics can lead to localised compositions and conditions significantly different to those studied here. These factors need to be examined and quantified in order to introduce additional modelling parameters or measures to account for them. Selection of other solid solution databases, such as mullite and wollastonite, may also result in different results under identical compositional and conditional inputs, though trends are likely to be similar. Also of importance is the lack of critical evaluation and optimisation for the relevant SiO_2-K_2O-CaO system (Lindberg, Backman, Chartrand, & Hupa, 2011) as well as higher order systems. Re-calculations will probably be necessary in the future as more thermodynamic data is accrued.

4.1 Conclusion

Comparison of the elemental compositions of possible melts within actual reactor deposits and those predicted by thermochemical equilibrium calculations for PEFG of wood and bark fuels have shown large discrepancies. The most obvious difference is the enrichment of Si and reduction of Ca in the actual deposits compared to their respective calculation results, as well as compared to the fuel ash compositions. It is clear from the bark campaign deposits that there are interactions between K, Ca and Si upon quartz and feldspar particles. This demonstrates the fractionation of different ash-forming elements during the PEFG process can lead to speciation of particular phases. Such instances constitute localised behaviour that cannot be adequately studied with global thermodynamic analysis. Hence, ascertaining the ash fractionation and speciation in different regions and pathways through the reactor is necessary to enable appropriate thermochemical equilibrium modelling of such localised interactions. Consequently, these more relevant comparisons would, in turn, lead to greater elucidation of the ash transformation processes during the PEFG process. In order to achieve this, the suggested ash collections at various locations to establish the K mass balance are depicted in Figure 21. The speciation of Si and Ca, as well as other less abundant elements, are also of importance. In addition to the ash collections, there must also be longer and more consistent experimental campaigns. The experimental campaigns utilised for this study had interruptions and did not reach steady-state, as least thermally. With the aforementioned limitations inherent to thermodynamic studies and uncertainties in mind, further knowledge (e.g., reactions kinetics and bulk process phenomena) in addition to extended experimental studies of pertinent systems (e.g.,SiO_2-K_2O-CaO (Lindberg, Backman, Chartrand, & Hupa, 2011)) are required in order to refine calculation inputs and verify results.

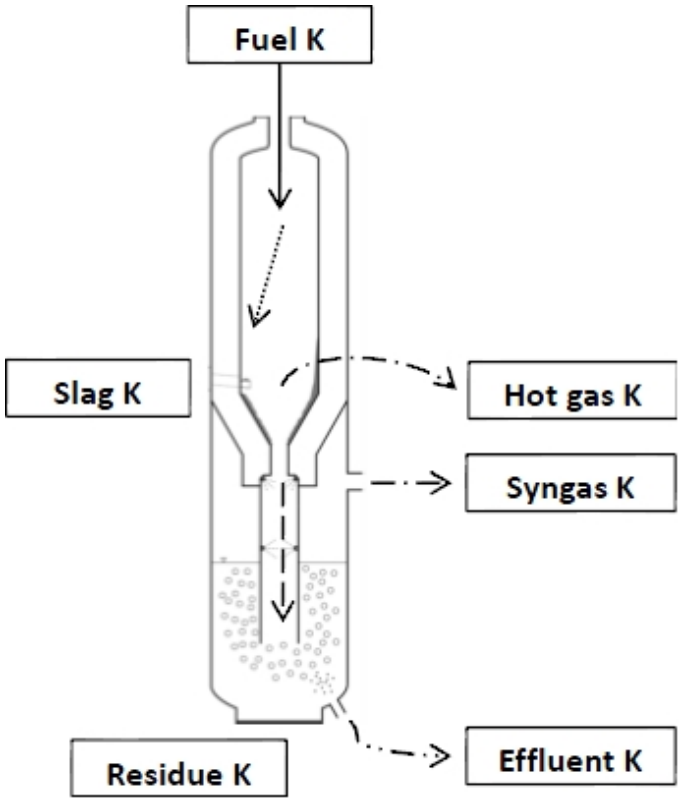

Figure 21. Ash sampling locations to quantify condensed and gaseous phase fractionation of K.

The following list is a summary of observations from the thermochemical equilibrium modelling study using currently commercially available software and thermodynamic databases. The level of applicability and/or relevance to the PEFG of woody biomass can only be ascertained with further experimental investigation as well as availability of reliable thermodynamic data.

When no additive is present:

- Oxide melt formation potential is greater for the bark fuel than wood fuel
- K is readily volatilised from wood and bark with increasing temperature
- Substantial amounts of Ca and Si can also be volatilised for both wood and bark fuels between 1600–1800 °C
- More elements are stabilised into the oxide melt and solubility of CO_2 is higher with increasing pressures. These occur relatively more markedly for the wood fuel.

- For wood, crystalline CaO and Ca-silicates can exist up to 1800–2000 °C but their levels are reduced with increasing pressure; instead Si and Ca stabilise within the oxide melt
- For bark, there is a tendency to form crystalline Ca-silicates at temperatures < 1300 °C independent of pressure, giving rise to similarity in the fractionation of Si and Ca

When kaolinite additive is present:

- K volatility increases with increasing temperature and decreases with increasing levels of kaolinite additive.
- Increasing levels of the additive produces alkali/alkaline-aluminosilicate, aluminosilicate and aluminium oxide crystalline phases that can co-exist with the oxide melt phase at temperatures < 1600°C
- Temperature plays a more significant role in determining the oxide melt composition than pressure
- Oxide melt viscosity generally decreases with increasing temperature, but increases with increasing amounts of additive
- Oxide melts from the bark fuel show significantly lower viscosities compared to those from the wood fuel

When olivine additive is present:

- The slag formation potential is lower than kaolinite; stabilisation of olivine group crystalline phases is favoured even up to high temperatures
- Temperature plays a more significant role in determining the oxide melt composition than pressure
- Viscosity of the oxide melt is lower than that for the kaolinite additive scenario
- Volatility of K is higher than for the kaolinite additive scenario

References

Bale, C., Bélisle, E., Chartrand, P., Decterov, S., Eriksson, G., Hack, K., et al. (2009). FactSage thermochemical software and databases — recent developments . *Calphad, 33*(2), 295–311.

Bale, C., Chartrand, P., Degterov, S., Eriksson, G., Hack, K., Mahfoud, R. B., et al. (2002). FactSage thermochemical software and databases . *Calphad, 26*(2), 189–228.

Duchesne, M., Bronsch, A., Hughes, R., & Masset, P. (2013). Slag viscosity modeling toolbox. *Fuel, 114*, 38–43.

Duchesne, M., Macchi, A., Lu, D., Hughes, R., McCalden, D., & Anthony, E. (2010). Artificial neural network model to predict slag viscosity over a broad range of temperatures and slag compositions. *Fuel Processing Technology, 91*, 831–836.

Grimm, A., Skoglund, N., Boström, D., & Öhman, M. (2011). Bed Agglomeration Characteristics in Fluidized Quartz Bed Combustion of Phosphorus-Rich Biomass Fuels. *Energy & Fuels, 25*, 937–947.

Lindberg, D., Backman, R., Chartrand, P., & Hupa, M. (2011). Towards a comprehensive thermodynamic database for ash-forming elements in biomass and waste combustion – Current situation and future developments. *Fuel Processing Technology*.

Ma, C., Weiland, F., Hedman, H., Boström, D., Backman, R., & Öhman, M. (2013). Characterization of Reactor Ash Deposits from Pilot-Scale Pressuized Entrained-Flow Gasification of Woody Biomass. *Energy & Fuels, 27*, 6801–6814.

Scudeller, L., Longo, E., & Varela, J. (1998). Potassium Vapor Attack in Refractories of the Alumina-Silica System. *Journal of the American Ceramic Society, 73*(5), 1413–1416.

Weiland, F., Hedman, H., Marklund, M., Wiinikka, H., Öhrman, O., & Gebart, R. (2013). Pressurized Oxygen Blown Entrained-Flow Gasification of Wood Powder. *Energy & Fuels, 27*, 932-941.

Werkelin, J. (2008). *Ash-forming elements and their chemical forms in woody biomass fuels elements.* Turku: Ph.D. thesis, Åbo Akademi.

Chapter 4

Behavior of inorganic species and char reactivity during biomass gasification

Liang Wang, Berta Matas Güell and Judit Sandquist, SINTEF Energy Research, Norway

Contents

1. Behavior of inorganic species and char reactivity during biomass gasification

1.1 Introduction

Biomass gasification represents a promising and efficient way to convert biomass into energy and valuable products. Compared to other thermochemical conversion routes, biomass gasification has several advantages with respect to large flexibility for feedstocks properties, and diverse options for products and high process efficiency.

Biomass gasification can be conceptually divided into two steps. Pyrolysis of biomass is the first step to produce volatiles and solid char. The pyrolysis step is also termed as devolatilization, considering high reaction rate and short reaction time of the step. The volatiles and solid char generated in the pyrolysis step undergo further reactions with a gasifying agent such as steam, oxygen or carbon dioxide, leading to reforming of volatiles towards syngas and gasification of char.[1] The char gasification is much slower than volatiles reforming, and is an overall rate-limiting step for the biomass gasification process. The conversion degree of char is critical for the overall energy conversion efficiency of the biomass gasification process. Char conversion behaviours strongly correlate with: 1) the reactivity of the char to gasifying agents, 2) structural factures of the char, and 3) amount of catalytic inorganic species such as alkali and alkaline earth metals retained in the carbon skeleton of char.[2]

One important aspect to consider during biomass gasification is the presence of inorganic species in the biomass. Biomasses from different sources contain a wide range of concentrations of inorganic species, which depends on type of plant biomass and growing conditions. Typically, biomass contains certain amounts of alkali and alkaline earth metals that are essential nutrients for plants growth. During biomass gasification, the alkali and alkali earth metals tend to react with other inorganic species and cause ash sintering, slagging and defluidization. In addition, vaporized alkali and alkali earth metals undergo further reactions and may lead to fouling and corrosion of gas turbine blades in biomass gasification based energy generation systems. On the other hand, alkali metals retained in the char after the pyrolysis/devolatilization stage may have an important catalytic effect on the char thermal conversion behaviors[3]. Presence of alkali metals enhances a reduction of

the gasification temperature and an increase of the overall gasification process efficiency and thus its profitability.[4] The volatilized alkali metals also act as catalyst for promoting the steam reforming of volatiles in gas phase. In order to get a good understanding of the complex role of alkali metals during biomass gasification, it is crucial to get a better understanding of the release of alkali metals during the process. Such knowledge and understanding are useful for taking advantage of special thermochemical properties of biomass, maximizing the catalytic role of alkali metals and reducing unpreferred influences from them.

1.2 Release of alkali metals during devolatilization of biomass fuels

1.2.1 Introduction

The use of biomass for energy production has been mainly restricted to woody biomass including sawdust, wood chips and cutter shavings. However, the availability of these raw materials is limited and the price of the conventional woody biomass has increased. Due to rapid increasing demand of biomass fuel in the past decades, new woody biomasses from the forest sector are entering the market. Compared to the conventional woody biomass, the concentrations of inorganic species in the new woody materials, such as bark, twigs, branches and needles, are much higher and significantly more heterogeneous. However, knowledge about the presence and transformation of these inorganic species during a gasification process is still limited.

Devolatilization is the first step of the biomass gasification process. As biomass is heated up to the decomposition temperature, volatiles are released to vapour phases containing organic compounds and gases whereas carbon-rich solid mass retains as the char. The volatiles and solid char then undergo gasification reactions at sufficiently high temperatures in the presence of gasifying agents. The devolatilization conditions such as heating rate, biomass particle size, peak temperature and holding time have significant effects on 1) amounts and compositions of released volatiles, 2) structure evolution of char and 3) release and transformation of inorganic species.[1, 5, 6] Furthermore, devolatilization conditions will influence the reactivity of char and conversion efficiency of the biomass gasification process.

The aim of this work is to investigate the release of K from bark as function of heating rate, peak temperature and particle size.

1.2.2 Experimental section

The biomass samples studied were spruce bark named Mönsterås and pine bark named Koirasaari. The raw bark was first ground to a particle size less than 1 mm. The particles with size in the range of 125–180 µm and 500–600 µm were collected by sieving the ground raw bark.

Devolatilization of biomass samples was performed in a novel thermogravimetric analyzer (TGA) (TA Q5000, TA Instruments) as shown in Figure 1. The predried biomass samples with different particle sizes were pyrolyzed at heating rates of 50, 200 and 1000 K/min from ambient to a prescribed temperature in the range of 600 to 1000 °C. Before each experiment, around 5–10 mg biomass sample was loaded in a sample pan. In order to avoid heat and mass transfer limitations, the biomass particle sample was as good as possible evenly distributed on the bottom of the sample pan as a thin layer. The sample was then purged in the TGA furnace with N_2 (purity>99.9999%) and heated up to a prescribed temperature without further holding. The char yield of the sample after a pyrolysis experiment was calculated.

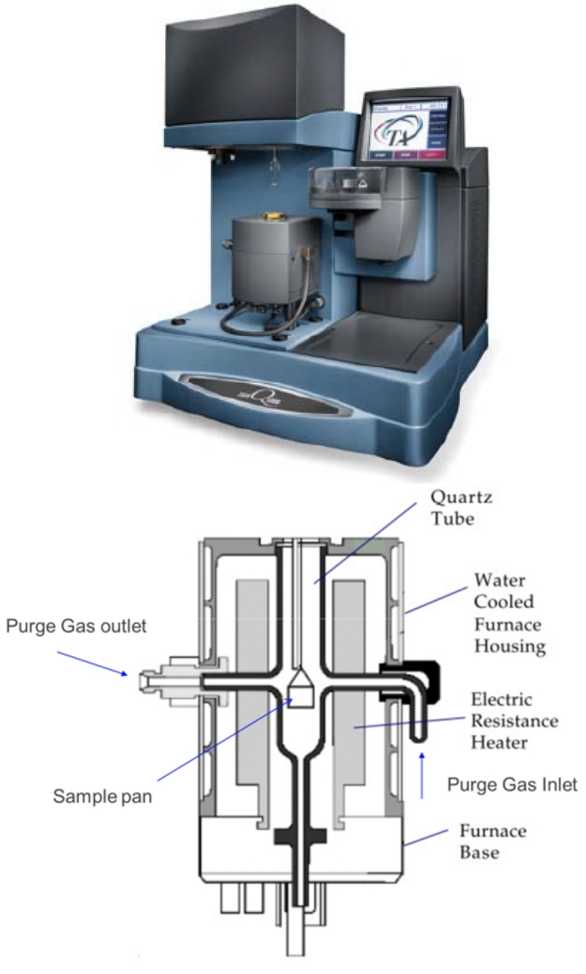

Figure 1. The thermogravimetric analyzer (TGA) used for pyrolysis experiments (above) and its schematic drawing of the furnace section (below).[7]

The solid residues left after each experiment were further collected and analysed by inductively coupled plasma atomic emission spectroscopy (ICP-AES) for quantifying concentrations of inorganic elements. The same analyses were done for the raw biomass samples with different particle sizes. The fraction of alkali and alkaline earth metals (AAEM) elements released during the devolatilization of one sample was further calculated based on concentration of an element in the raw fuel and in the solid residue, and the weight of fuel and its solid residue after the pyrolysis experiment. Selected solid residues were also examined by scanning electron microscopy with energy dispersive X-ray spectroscopy (SEM/EDX), in order to obtain more detailed micro ash chemistry information.

1.2.3 Results and discussion

The chemical compositions of the raw fuels with different particle sizes are presented in Table 1. Concentrations of main inorganic elements in spruce bark are significantly higher than those in pine bark. Such big differences of concentrations of inorganic elements are mainly related to the nature of the two tree species. Three key elements molar ratios are also shown in Table 1. It is clearly shown that the spruce bark is a Si-rich fuel. In combination with high K content in the fuel, the ash characteristics are expected to be dominated by K-silicate chemistry.

Table 1. Chemical compositions of spruce and pine bark particles (mg/kg, dry fuel).

	Spruce bark			Pine bark		
Element	d<1 mm	125<d<180 mm	500<d<600 mm	d<1 mm	125<d<180 mm	500<d<600 mm
K	2349	2720	2229	580	597	524
Na	323	254	227	33	55	31
Si	3550	3710	3380	500	540	485
Ca	8449	8191	8067	6120	6159	5822
Mg	697	718	659	173	193	133
P	454	477	422	128	136	96
S	346	386	332	271	245	169
Al	438	373	321	438	354	265
Fe	429	477	324	59	97	16
Molar ratio						
K/Si	0.48	0.53	0.47	0.83	0.79	0.78
(Ca+Mg)/Si	1.90	1.77	1.90	8.97	8.53	8.72
(K+Ca+Mg)/Si	2.37	2.30	2.37	9.80	9.32	9.50

Figure 2 shows char yields of the studied spruce and pine bark particles as function of pyrolysis temperature, particle size and heating rate. The results show that

both pyrolysis conditions and particle size have significant effects on char yields for two fuels. As expected, char yields decreased with increasing temperature due to further conversion of the fuel samples at higher pyrolysis temperatures. One should note that, at a particular temperature, higher char yields were obtained with the samples with larger particle sizes. This effect can be attributed to several factors. First, the mass transfer resistance in large particles is much higher than the in smaller ones. As a result, residence time of tarry vapours in the char structure of larger particles is longer, enhancing recombination of tarry compounds on the char internal surface, which in turn reduces the weight loss of the char. Second of all, heat transfer resistance giving temperature gradients from the surface to the centre of the larger particles are more pronounced. Thus, temperatures in the centre of larger particles can be much lower than those in the outer part, resulting in slower devolatilization and fuel conversion and therefore increased char yields.

Figure 2 shows that higher char yields were obtained at low heating rates. Low heating rates tend to slow down the release of volatiles, resulting in longer residence times of volatiles in the particles. This facilitates the repolymerisation of volatiles within the particles, enhancing char yield as compared to higher heating rates (rapid/flash pyrolysis). As a result of condensation of tarry vapours on solid char surfaces, the reactivity of char is lower, which again gives negative effects on char conversion.

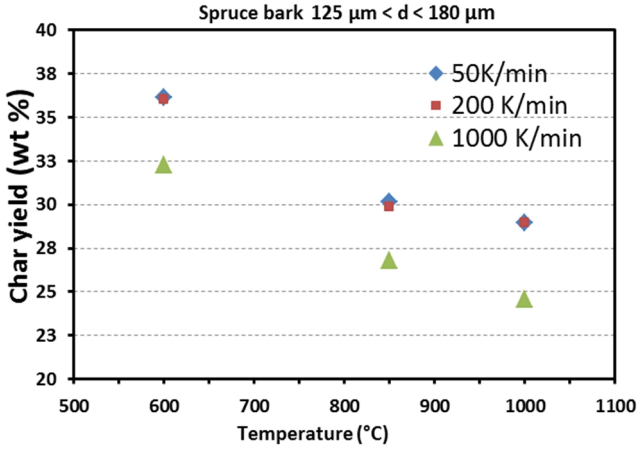

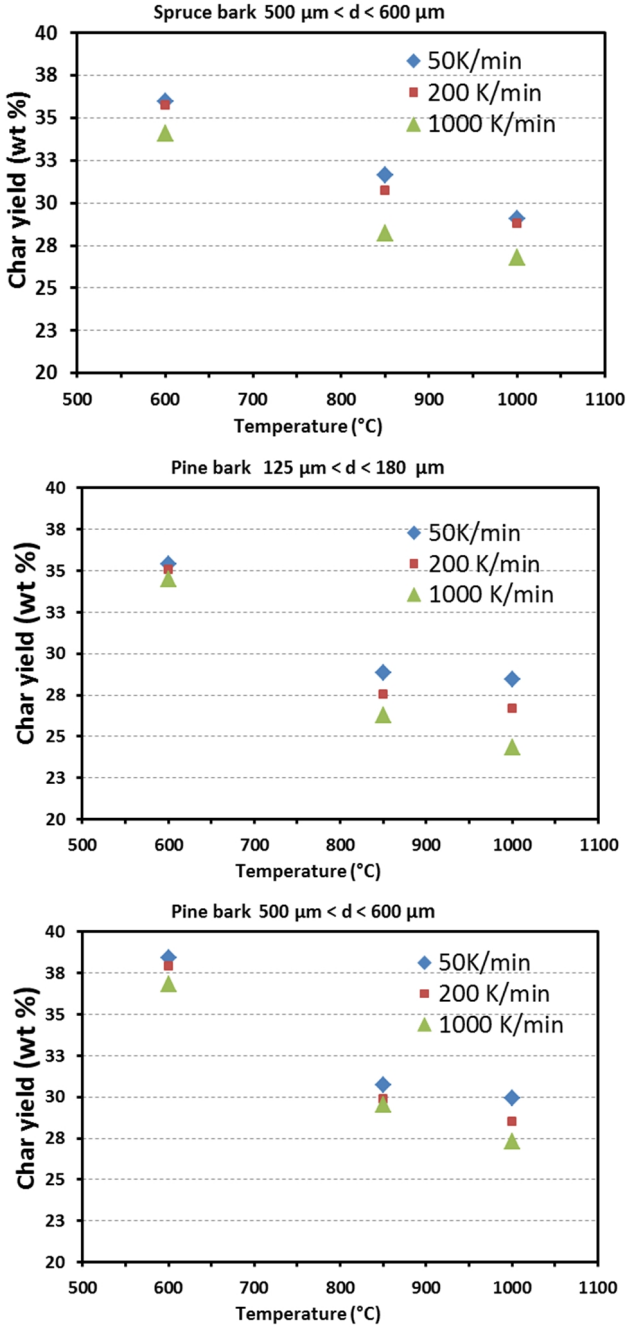

Figure 2. Char yields of studied samples at different pyrolysis temperatures and heating rates.

Release of potassium during devolatilization of spruce and pine bark is shown in Figures 3 and 4. For the spruce bark, no evident potassium release was observed at temperatures as low as 600 °C. In contrast, more than 5% of the potassium was released from the pine bark particles after pyrolysis experiments at 600 °C. When increasing the pyrolysis temperature from 850 to 1000 °C, distinct potassium release behaviours were observed from both spruce and pine bark. In addition, the fractions of potassium released from pine bark were clearly larger than those from spruce bark. Usually, Cl is a main inorganic element in biomass fuel for facilitating the release of K in the form of chlorides.[8] At the same time, K will be retained by Si in the fuel through formation of K-silicates in solid residues. The alkali earth metals Ca and Mg will compete with K to be incorporated into the silicates, enhancing release of K to the gas phase. Table 1 summarizes the molar ratios of key elements regarding K release and retention properties. Considering the low Cl content in both bark fuels, the K/Cl molar ratio was not calculated. It is clear that K/Si, (Ca+Mg)/Si and (Ca+Mg+K)/Si molar ratios of the pine bark are significantly higher than those of spruce bark. With high K/Si, (Ca+Mg)/Si and (Ca+Mg+K)/Si molar ratios, high K release can be expected as proved in the present work (Figure 3). The present work implies that potassium release from the two studied fuels is also influenced by fuel chemical compositions in the studied temperature range.

The data in Figure 3 illustrates that release of K from the two studied bark fuels was also considerably influenced by heating rate. Significant differences in the release of potassium between the fast heating and slow heating rate experiments were observed as pyrolysis experiments were carried out at temperatures of 850 and 1000 °C. The substantial release of potassium at higher temperatures at high heating rate was partly due to more intensive interactions between volatiles and char under such experimental conditions. During pyrolysis of the biomass, tar and light hydrocarbons are released as volatiles that tend to crack and lead to production of free radicals (mainly K radicals).[4] At a sufficiently high temperature, the bonds between AAEM species and the char matrix are broken due to presence of free radicals, resulting in volatilization of AAEM species. Considering that at high heating rates, more intensive devolatilization occurs and thus larger amount of volatiles are produced, free radicals will be produced also to a larger extent, promoting the release of AAEM from the char matrix (see Figure 3).

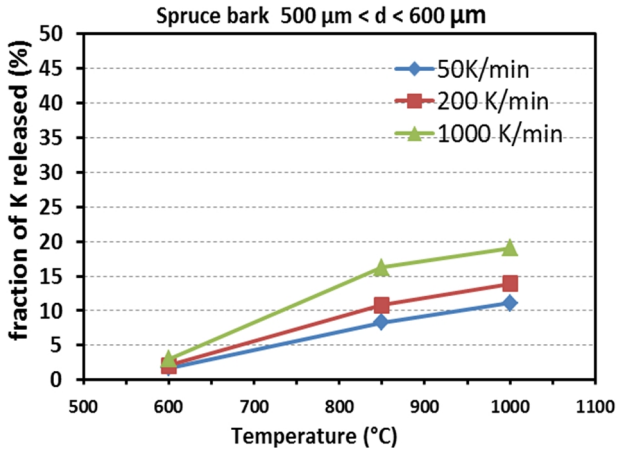
Spruce bark 500 µm < d < 600 µm
fraction of K released (%)
50K/min
200 K/min
1000 K/min
Temperature (°C)

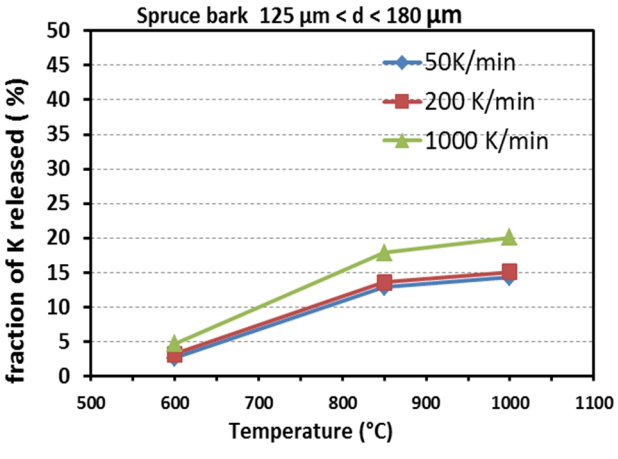
Spruce bark 125 µm < d < 180 µm
fraction of K released (%)
50K/min
200 K/min
1000 K/min
Temperature (°C)

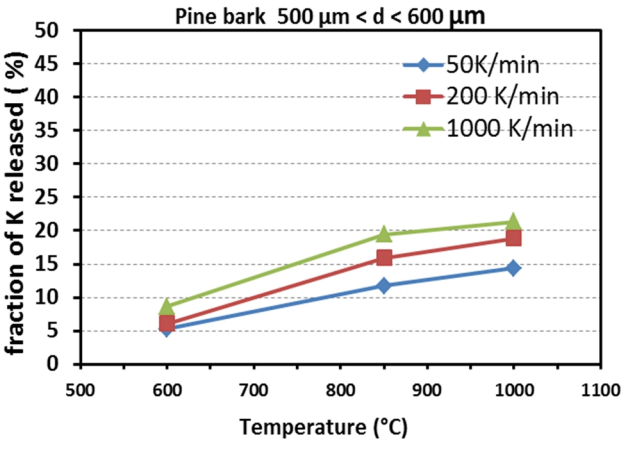
Pine bark 500 µm < d < 600 µm
fraction of K released (%)
50K/min
200 K/min
1000 K/min
Temperature (°C)

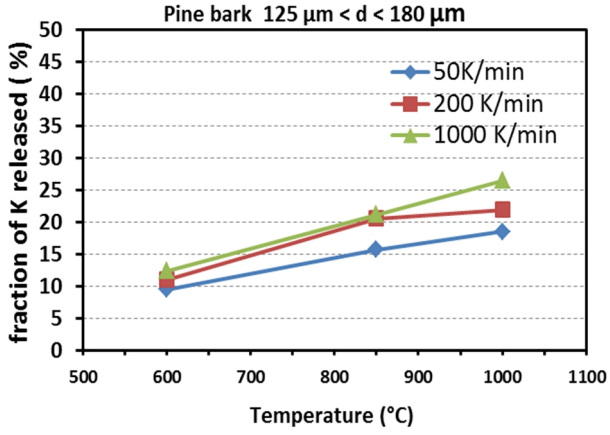

Figure 3. Release of potassium during pyrolysis of spruce and pine bark particles as a function of temperature and heating rate

As Figure 4 shows, the release of potassium increases with decreasing particle size. During biomass pyrolysis, the potassium will primarily be released together with other volatiles. In the larger particles, the internal pressure of volatiles and released inorganic species is more intense due to mass transfer resistance in the skeleton of the carbon matrix in the char residues.[3] Therefore, the potassium is preferentially deposited on char surfaces and inside the carbon matrix. In addition to intra-particle volatile-char interactions, the volatiles already released will surround and interact with the char particles formed earlier. Such interactions are more intensive for smaller particles, which again cause breakdown of bonds between potassium and the char matrix and further volatilization of potassium into the vapour phase.

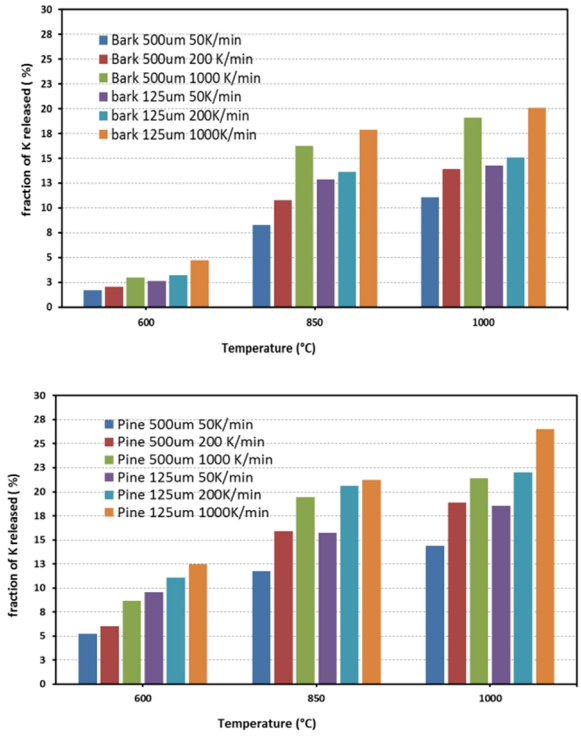

Figure 4. Potassium release from large and small biomass particles at 600, 850 and 1000 °C

Figures 5–8 show SEM images from the char residues generated during biomass pyrolysis with a 1000 °C/min heating rate to 1000 °C. In Figure 5, a few grains with light grey colour can be easily distinguished. The EDX analysis revealed that they are silica-rich particles that probably originate from sand and soil contamination. These silica-rich particles can also react with K released during the spruce bark conversion and thus reduce the fraction of K volatilized to the gas phase. It partly explains that smaller fractions of K are released from the spruce bark particles at all experimental conditions, compared to those from the pine particles.

The char residues also show some white grains dispersed on the surface and embedded in the structure of the organic char matrix that appears as a dark-grey surface. These white grains are rich in Ca, as indicated by EDX analysis, and are either discrete or sintered together. Fast pyrolysis treatment of biomass particles causes intensive release of carboxyl groups like char-COOM, where the M can be K, Na, Ca and Mg. The char-COOM will further decompose into solid char on the one hand and into CO_2 and M in the gas phase on the other hand.[1] Such Ca-rich grains represent release of volatiles from the fuel particles and dispersion of calcium from the char matrix to outer surfaces.

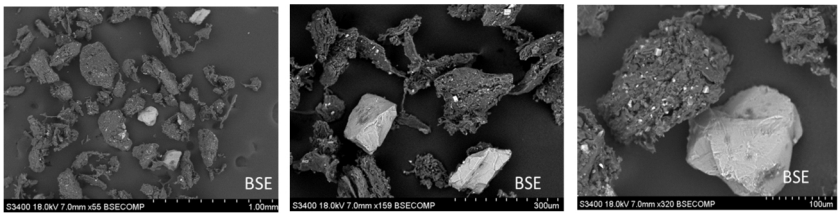

Figure 5. SEM images of char residues of spruce bark particles (125 µm < d < 180 µm) pyrolyzed from 25 °C to 1000 °C with a 1000 °C/min heating rate.

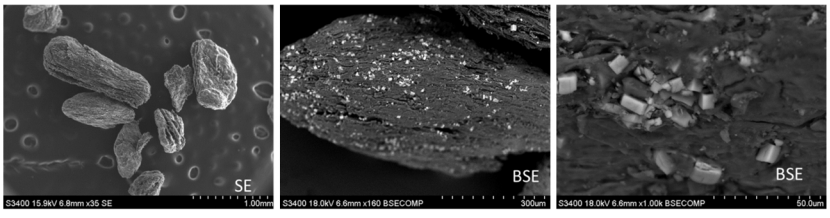

Figure 6. SEM images of char residues after spruce bark particles (500 µm < d < 600 µm) pyrolyzed from 25 °C to 1000 °C with a 1000 °C/min heating rate.

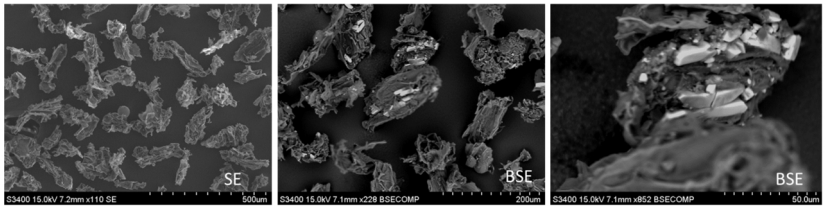

Figure 7. SEM images of char residues after pine bark particles (125 µm < d < 180 µm) pyrolyzed from 25 °C to 1000 °C with a 1000 °C/min heating rate.

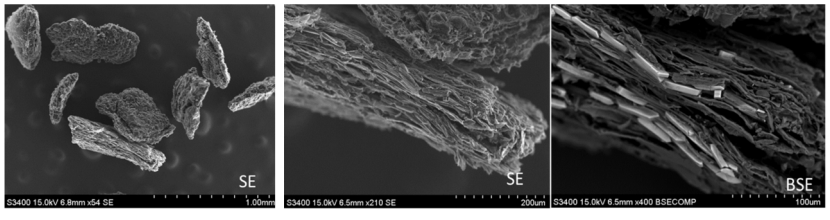

Figure 8. SEM images of char residues after pine bark particles (500 µm < d < 600 µm) pyrolyzed from 25 °C to 1000 °C with a 1000 °C/min heating rate.

1.3 Release of alkali and heavy metals during thermal conversion of biomass fuels

1.3.1 Introduction

The alkali metals and heavy metals, as well as S and Cl are among the most important ash forming elements causing operational problems in thermal biomass conversion processes. Alkali metals and heavy metals are partly released from the fuel to gas phase, which either undergo complex chemical reactions or instantly form aerosols. The release and transformation of alkali metals and heavy metals are relevant for formation of particulate matters, deposits formation on heat transfer surfaces and deposits induced corrosion in the bioenergy production system. Reliable quantitative data are needed regarding release of alkali metals and heavy metals during thermal conversion of biomass, in order to predict ash related operational problems and propose proper solutions.

The release of inorganic species during thermal conversion of biomass fuels have been investigated in a number of studies. For most of them, the studied fuels were ground or pulverized before the experiment. However, pelletized biomass fuels are more relevant since they are used directly in different processes for energy purposes. It is important to obtain a better understanding of release of ash forming elements during the thermal conversion of biomass pellets.

In the present study, the release and transformation of ash forming elements during thermal conversion of a single biomass pellet were studied. The fuel pellet was converted at combustion and pyrolysis conditions in a single particle reactor. The aim of this study was to reveal the influence of temperature, inlet gas atmosphere composition and char conversion on the release of a number of ash forming elements.

1.3.2 Experimental section

To study the release of alkali metals and heavy metals, thermal conversion of biomass pellets was performed in a Single Particle Reactor (SPR, Figure 9). In the SPR, a quartz tube was heated in an electrically heated ceramic furnace. Mixtures of air and nitrogen are fed directly to the tube reactor and the flows of gases are controlled by mass flow controllers. An oxygen concentration of 3 vol% was used for creating an oxidizing atmosphere. The milled fuels were first pelletized at 10 bar pressure into pellets with size of 8 x 6 (d x h) mm and a mass around 200 mg. Before one experiment, the reactor was first heated up to the desired temperature. Then the sample pellet was inserted into the hot reactor by using a movable probe in a fraction of a second. The sample holder is a quartz plate on which one pellet was placed. The evolved gas from the pellet combustion were monitored by three commercial gas analyzer for the measurement of O_2, CO, CO_2, NO and SO_2.

In total four fuels were converted at two gas atmospheres, three peak temperatures and four different holding times. The gas atmospheres were 1) 3% O_2 + 97%

N_2 and 2) 100% N_2. The temperatures were 800 °C, 900 °C and 1050 °C. The four holding times are: devolatilization, 50% char burnout, char burnout and char burnout with extra 5 minutes holding time.[9] The time for the devolatilization time was established based on a flame out criteria and the third stage was determined from the recorded CO and CO_2 gas signals. The extra 5 minutes holding time represents the ash cooking process after the complete combustion of the pellet. Table 2 shows the time used for spruce bark and spruce wood to finish devolatilization and char burnout.[9]

The inorganic species in the fuel, in the solid residues after experiments, were analyzed by both ICP-AES and ICP-MS analysis. Each sample was first digested in a mixture of HNO_3 (4ml), $HClO_4$ (2ml) and HF (0.5ml) in a microwave digester. In addition, selected char and ash residues after fuel conversion were collected and further analyzed by SEM-EDX.

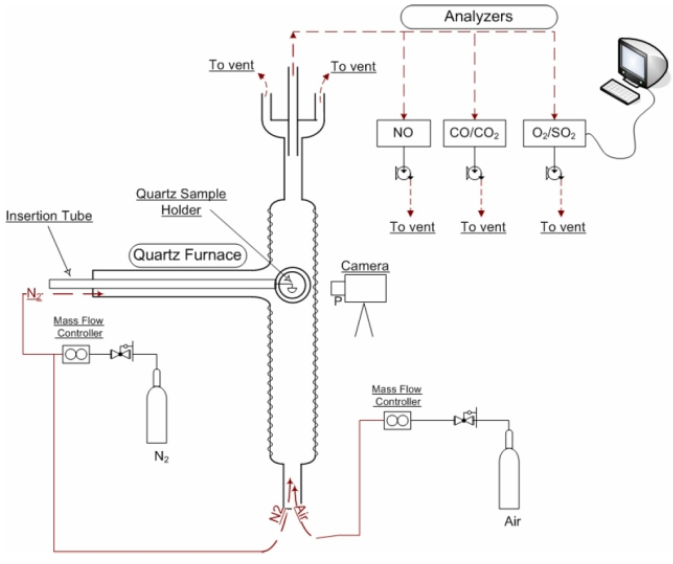

Figure 9. Schematic of the single particle reactor setup and emission monitoring devices.

Table 2. Time (seconds) required for the devolatilization and char burnout.

Fuel	Devolatilization (flameout)			Char burnout		
	800 °C	900 °C	1050 °C	800 °C	900 °C	1050 °C
Spruce wood	60	50	40	2850	1790	1200
Spruce bark	60	50	50	2240	1540	1140

1.4 Results and discussion

The fuel chemical composition analysis results are presented in Table 3. The concentrations of most of the ash forming elements in the bark are much higher than those in the wood. K, P, S and Mg are soluble in different types of sap solutions and might translocate between different parts (i.e., stem, bark and twig) of a tree. These elements are likely to accumulate in the young and biological active tissues with rather higher water contents. The bark contains significant amounts of such active tissues and a large fraction of ash forming elements as well. The large differences in the content of ash forming elements in spruce bark and wood have been well studied and well reported in previous studies.[10]

Table 3. Ash content and chemical composition (mg/Kg) of the fuels.

	Ash content (wt %)	Ca	Si	K	Na	Mg	Al	P	S	Mn	Cl
Spruce bark	5.0	12900	3180	1840	98	813	733	335	301	675	98
Spruce wood	0.48	1160	83	574	7	243	15	60	38	75	11

Table 4. Molar ratio of key ash forming elements.

Molar ratio (mol/mol)	Si/K	Si/(Ca+Mg)	(Si+P+K)/(Ca+Mg)
Spruce wood	0.20	0.08	0.48
Spruce bark	2.40	0.32	0.50

Figure 10 shows the release of K from spruce wood and bark pellets as function of conversion temperature and time. It can be seen that the release of K from the two kinds of fuel pellets already started at 800 °C. With longer holding times, the increases of K released from both fuels are less pronounced. Release of K from woody biomass in the temperature range 500–800 °C is related to the volatilization of organically bonded K in the char matrix. As shown in Figure 10, as the temperature is above 900 °C, the release of K from the pellets is more pronounced, especially for the spruce wood. At 1050 °C, about 70% of the K was already released as gases after the char burnout stage. During thermal conversion of woody biomass, char-bonded K is released first in the low temperature range from 500–800 °C, and a significant fraction of the remaining K will transform into K_2CO_3 in solid phase as the temperature is lower than 850 °C.[8] The $K_2CO_{3(s)}$ starts to decompose as the temperature reach 850 °C. This can explain the evident increase of K released at 900 and 1050 °C. The SEM images in Figure 11 show the sintering process of the bark ash residues at elevated temperatures.

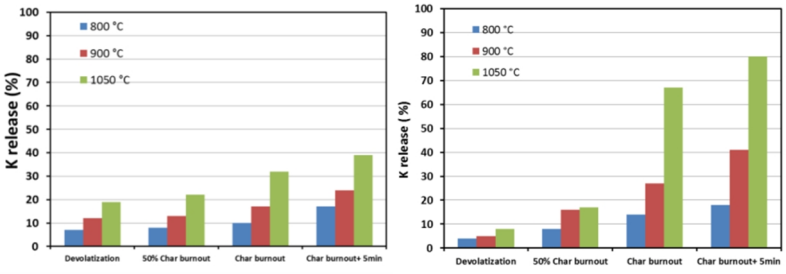

(1) spruce bark (2) spruce wood

Figure 10. Release of K as function of conversion temperature and time.

The K release profiles at the temperature 1050 °C were significantly different between the spruce bark and spruce wood pellets. The differences in K release from the two fuels are partially related to the chemical compositions of the two kinds of fuel pellets. During thermal conversion of the pellets, reactions between K and silicates in the char/ash are more active at such high temperature.[8] The K readily incorporates into silicates and form K-silicates consequently. This process will reduce the amount of K that is volatilized into vapours. Therefore, the release of K at high temperature may be influenced by the Si/K molar ratio of the fuel. As shown in Table 4, the Si/K molar ratio of the spruce bark is much higher than that of the spruce wood, implying intensive retention of K by silicates in the fuel. In addition, Ca in the fuel may also compete with K for positions in the silicate matrix. Presence of Ca and Mg in the fuel will cause release of K to a certain extent. Therefore, the low Si/(Ca+Mg) molar ratio is more favorable for K release for the spruce wood at high temperature.

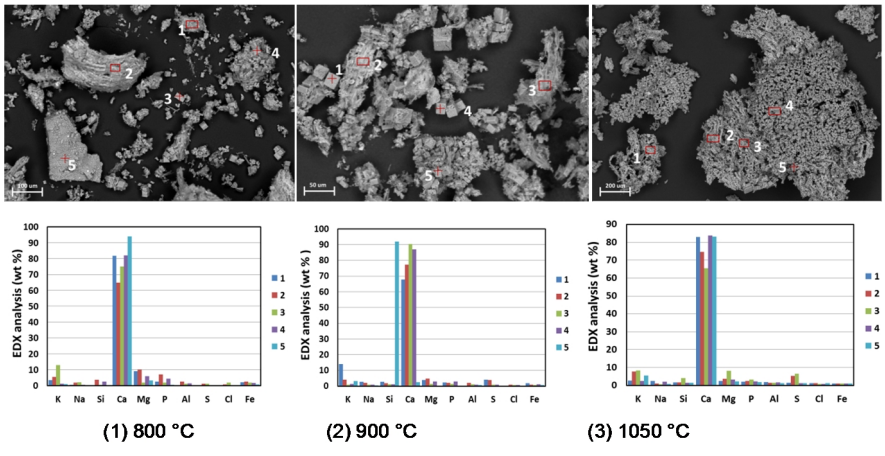

(1) 800 °C (2) 900 °C (3) 1050 °C

Figure 11. SEM-EDX analyses of residues collected after spruce bark combustion experiments.

1.5 Kinetic study of CO_2 gasification of chars prepared from wood and forest residues

1.5.1 Introduction

Presently, forest residues, as abundant low-cost biomass resources, are gaining interests and entering the renewable energy market while wood is considered as a raw material for higher-value products. Gasification is a highly efficient technology to convert biomass fuels and produce electricity and synthesis liquids/chemicals. The biomass gasification process conceptually consists of two consecutive steps: 1) pyrolysis of biomass to produce volatiles and solid char, and 2) reforming of volatiles in the gas phase and gasification of char residues with gasifying agents like CO_2, O_2 or H_2O. The gasification of the char is an important partial reaction of the biomass gasification. It is considered to be a rate limiting step because it is kinetically slower than the devolatilization and reforming reactions. Accordingly its heterogeneous kinetics highly impacts the design of gasifiers. In addition, CO_2 gasification of biomass may become a separate technical process in the future for converting biomass resources into energy and different valuable products, if charcoal is firstly produced from the raw biomass. Therefore, it is essential to characterize the CO_2 gasification kinetics of the chars produced from different woody biomass sources.[11]

The present work deals with the CO_2 gasification of stem wood and forest residues from Norway spruce [*Picea abies* (L.) Karst], which is a widespread tree species in the Nordic countries. CO_2 gasification of char produced from stem wood and forest residues under kinetic control were studied to provide a background for future kinetic sub-models. With its high precision and well-controlled experimental conditions, TGA is a useful tool for studying gasification in the kinetic regime. Particular efforts were made in the present work to obtain dependable kinetic information. This goal was achieved by the following means:

(i) The chars were almost completely devolatilized during the preparation so that the gasification reaction could be studied without the disturbance of a considerable devolatilization;

(ii) The study was based on linear, modulated and constant reaction rate (CRR) experiments so that the obtained kinetics would be valid for very different T(t) programs;

(iii) Care was taken to carry out the experiments in the kinetic control regime. The potentially disturbing effects of the heat and mass transfer processes were diminished by low sample masses and slow heating rate programs.

1.5.2 Experimental section

1.5.2.1 Sample characterization and preparation

The stem wood and forest residues (containing branches, tops and needles) originated from a Norway spruce forest in East Norway from stands with poor site quality. The received samples were first milled in a cutting mill equipped with a 1 mm bottom sieve, then dried for 24 h at 105 °C in a drying oven. Afterwards the chars were prepared at 950 °C following the carbonization procedure of ASTM standard E 872-82, which serves to determine the amount of volatile matter in particulate wood fuels. In this way the chars used in the study could be regarded as the “fixed carbon” plus ash of the raw materials if the standard volatile content of the samples was zero by definition. The char samples produced at 950 °C were further characterized by a Brunauer-Emmett-Teller (BET) specific surface analyzer, laser diffractometer, in terms of particle surface area, size distribution and chemical compositions. The chemical compositions of raw stem wood and forest residues were analysed by inductively coupled plasma atomic emission spectroscopy (ICP-OES) and the results are shown in Table 6.

1.5.2.2 Experimental setup and procedure

The reactivity studies were conducted in a Q5000 IR analyzer from TA instruments which has a sensitivity of 0.1 µg. 60% v/v CO_2-argon mixture and pure CO_2 were used as purge gas with a gas flow of 25 mL/min. Particular care was taken to avoid the presence of oxygen traces because a char+O_2 reaction would result in disturbing TGA signals. The initial sample mass was around 1 mg to avoid the self-cooling of the samples that the high endothermic reaction heat may cause. For a comparison, another set of experiments were carried out with ca. 2 mg initial sample masses.

Three temperature programs were used:

(i) linear T(t) with a heating rate of 10 °C/min;

(ii) modulated T(t), where sinus waves with 5 °C amplitudes and 200 s wavelength were superposed on a 10°C/min linear T(t);

(iii) “Constant reaction rate” (CRR) T(t), when the employed equipment regulated the heating of the samples so that the reaction rate would oscillate around a preset limit.

1.5.2.3 Numerical methods and kinetic evaluation

Fortran 95 and C++ programs were employed for the numerical calculations and for graphics handling, respectively. The employed numerical methods have been described in details earlier. The kinetic evaluation was based on the least squares evaluation of the -dm/dt curves. The method used for the determination of -dm/dt does not introduce considerable systematic errors into the least squares kinetic

evaluation of experimental results. The model was solved numerically along the empirical temperature – time functions. The model parameters were determined by nonlinear least squares minimization, as outlined in the next section.

1.5.3 Results and discussion

The particle size distribution of the obtained chars was measured by laser diffractometer (Coulter LS230 Laser Diffraction Particle Size Analyzer). The mean particle size of the chars from wood and forest residues was 69 and 75 µm, respectively. 90% (v/v) of the particles were above 16 and 18 µm in the two chars, respectively. Less than 1% (v/v) of the chars was below 4 µm. The Brunauer-Emmett-Teller (BET) specific surface areas were 271 and 205 m^2/g for the charcoal produced from the stem wood and forest residues, respectively. Compared to the stem wood, the forest residues contain significant amounts of alkali and alkali earth metals (AAEM), as shown in Table 5. Presence of AAEM in the biomass can give considerable effects on gasification behaviours of raw fuel and char residues, considering the catalytic effects of the AAEM.

Table 5. The Concentration of Ash Forming Elements in the Raw Materials [a].

	Ca	Si	K	Na	Mg	Al	P	S	Mn	Fe	Zn	Ba
Forest residues	6479	3399	2747	31	408	140	402	248	409	67	49	25
Spruce Wood	719	456	584	7	169	9	28	42	145	16	10	10
Ratio[b]	9	7.5	4.7	4.4	2.4	15.6	14.4	5.9	2.8	4.1	4.9	2.5

[a] ppm (mg/kg, dry basis). [b] Ratio of the concentrations of the forest residue and the wood. (It is not given for the concentrations near the sensitivity limit of the equipment)

Figures 10 compares the behavior of the wood and forest residues samples, respectively, at 10 °C/min heating rate, in 60% and 100% CO_2, for 1 and 2 mg initial sample masses. This comparison indicates that the char prepared from forest residues reacts at lower temperatures than the wood char. The temperatures were recorded at 50% mass loss as a simple, comparable characteristic value. These values showed 20–34 °C differences between the two chars at 10 °C/min heating rate. The observed behavior can be attributed to the catalytic effect of the high ash content of the forest residues. Note that the majority of the cations listed in Table 2 have proved to have catalytic effect on the char gasification rate.

The samples with 2 mg initial mass (colors magenta and green) reacted at higher apparent temperatures than their counterparts with 1 mg initial sample mass (colors dark red and dark blue, respectively). This behavior indicates a self-cooling effect for the higher sample mass: i.e. the real temperature in the sample was lower than the one measured by the equipment. It is worth noting that this effect was particularly visible in the case of the wood char sample, which gasified at higher temperatures with higher reaction rates. In the following treatment the results obtained from the 1 mg experiments are detailed because they are prone to be less influenced by heat transfer limitations.

The CO_2 concentration had a particularly significant effect on the curves, as displayed in Figure 12. A higher concentration of CO_2 in the inlet gas is expected to give a promoting effect on the gasification rate of char.

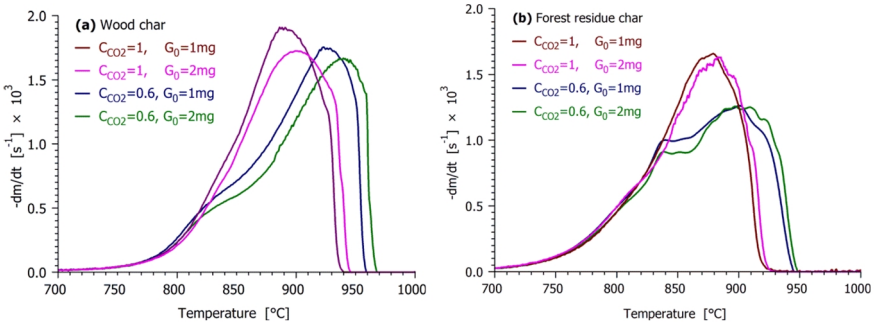

Figure 12. Effect of the initial sample mass and the CO_2 concentration on the char gasification rates with 10 °C/min heating rate.

The fit quality obtained in Evaluation 3 is shown in Figure 13, where the observed and calculated curves are denoted by colors gray and red, respectively. The difference between the experimental and simulated curves appears to be very low in Figure 13.

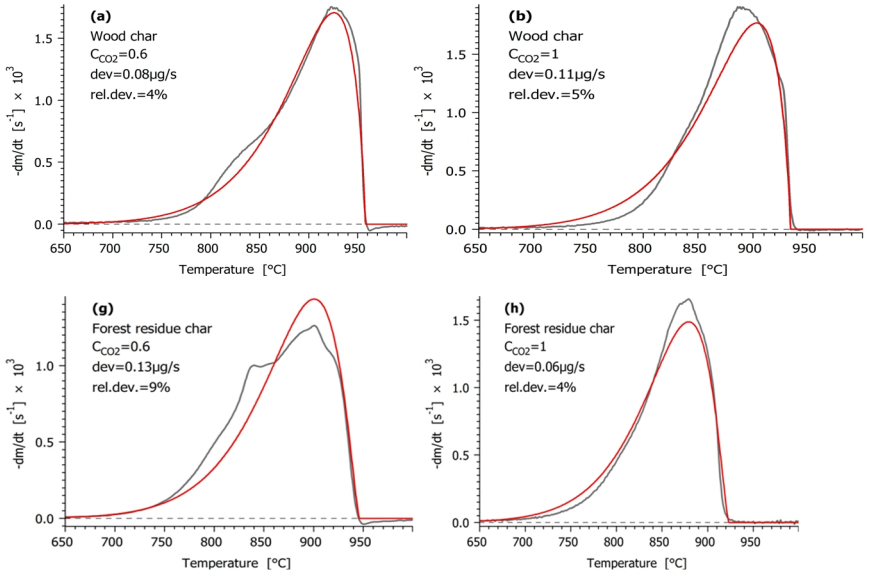

Figure 13. Evaluation of the linear heating experiments assuming common E (activation energy (kJ/mol)) and v (reaction order with respect of CO_2 concentration) values. Notation: experimental DTG curves normalized by the initial sample mass (grey —); their calculated counterpart (red —).

The obtained gasification process parameters are shown in Table 6. For both stem wood and forest residues, the resulting parameters were similar, as Table 6 reveals. The difference between the corresponding *E* values is only 4.7 kJ/mol, for gasification of 1 mg and 2 mg samples, respectively. The n values (reaction order with respect to fraction of converted fuel) are nearly identical in the two cases while the ν values show some differences. Altogether these reaction constants, shown in Table 6, indicate that heat and mass transfer limitations had little effect on the resulting parameters in the 2 mg experiments.

Table 6. Parameters Obtained by Evaluation 3 from the Two Series of 12 Experiments with Results from an Earlier Work for Comparison.

	Experiments with 1 mg initial sample mass		Experiments with 2 mg initial sample mass		Results from an earlier work[12]	
	Spruce Wood char	Forest residue char	Wood char	Forest residue char	Birch char	Pine char
E / kJ mol^{-1}	221	=	225	=	262	=
ν	0.89	=	0.81	=	0.40	=
n	0.44	0.58	0.45	0.58	0.44	0.75
$\log_{10} A/s^{-1}$	7.32	7.54	7.47	7.70	9.02	9.25

1.6 Conclusions

Biomass gasification has attracted continuous interests during the last decades. A comprehensive practical and theoretical knowledge about gasification of conventional and rather clean woody biomass have been obtained. However, competition for using such woody biomass has increased significantly due to the rapid increasing demand of biomass recently. Thus new raw materials from the forest sector are entering the market for energy production purpose. These new raw materials are more heterogeneous in terms of fuel properties, chemical compositions and thermal conversion behaviors.

In comparison to conventional woody biomass, there are a number of distinct differences related to contents of ash forming elements and heterogeneities of inorganic species for the new raw woody biomass fuels from the forest sector. For the spruce bark and pine bark studied in the present work, Ca, Si and K are main inorganic elements in the fuel, with presence of small amounts of Mg, Fe, Al, S and Na. However, there are significant differences between absolute concentrations of inorganic elements in the two bark fuels. In addition, there are large variations in ash forming matters and contents between different constituents from a wood species. Compared to stem wood, bark from the same tree species has a

much higher ash content and concentration of ash forming matters. The behaviors of these inorganic species under gasification conditions undergo complex reactions and exhibits large differences. More detailed knowledge about behaviors of these inorganic species is a prerequisite for a technical developed and efficient forest residues biomass gasification process.

Devolatilization is the first and critical step during the biomass gasification process in terms of volatilization of inorganic species and reactivity of char for further gasification reactions. The devolatilization conditions heating rate, particle size, peak conversion temperature and residence time have significant effects on char yields and release behaviors of inorganic elements like K and Ca. The char yield increased with increasing particle size as shown in the present work. In contrast, the char yield decreased with increasing heating rate, peak temperature and residence time applied during the devolatilization process. Release of potassium during the devolatilization increased consistently with increasing heating rate and peak temperature. More potassium was retained in the char from the larger fuel particles.

The fuel chemical compositions have significant effects on potassium release and transformation during a thermal biomass conversion process. The relative concentrations of key inorganic elements in woody biomass have major influences on potassium release sequences. High content of Si in the woody biomass fuel will restrain potassium release at high temperature. On the other hand, Ca and Mg have high thermodynamic affinities towards silicates and readily incorporate into silicates. Therefore, the Ca and Mg will compete with potassium for positions in silicates. Therefore, the K in fuel and char particles will be driven out by Ca and Mg to a certain extent, with volatilization of K as a result. The molar ratio of key inorganic elements, such as K/Si and (Ca+Mg)/Si ratios, can be very useful for predicting and interpreting potassium release behaviors.

Behavior and kinetics of chars prepared from wood and forest residue gasification under CO_2 atmosphere were studied. Different gasification rates of the two types of char were observed, which are largely related to the amounts and compositions of inorganic elements in the char. A relatively simple but widely used reaction kinetics equation described well the experiments. The dependence of the reacted fraction as well as the dependence of the CO_2 concentration was described by power functions (n-order reactions).

References

1. Li, C.-Z., Importance of volatile–char interactions during the pyrolysis and gasification of low-rank fuels – A review. Fuel 2013, 112, (0), 609–623.

2. Umeki, K.; Moilanen, A.; Gómez-Barea, A.; Konttinen, J., A model of biomass char gasification describing the change in catalytic activity of ash. Chemical Engineering Journal 2012, 207–208, (0), 616–624.

3. Asadullah, M.; Zhang, S.; Min, Z.; Yimsiri, P.; Li, C.-Z., Effects of biomass char structure on its gasification reactivity. Bioresource Technology 2010, 101, (20), 7935–7943.

4. Keown, D. M.; Hayashi, J.-i.; Li, C.-Z., Effects of volatile–char interactions on the volatilisation of alkali and alkaline earth metallic species during the pyrolysis of biomass. Fuel 2008, 87, (7), 1187–1194.

5. Asadullah, M.; Zhang, S.; Li, C.-Z., Evaluation of structural features of chars from pyrolysis of biomass of different particle sizes. Fuel Processing Technology 2010, 91, (8), 877–881.

6. Okuno, T.; Sonoyama, N.; Hayashi, J.-i.; Li, C.-Z.; Sathe, C.; Chiba, T., Primary Release of Alkali and Alkaline Earth Metallic Species during the Pyrolysis of Pulverized Biomass. Energy & Fuels 2005, 19, (5), 2164–2171.

7. High resolution thermogravemetric analysis – A new technique for obtaining superior analytical results. TA Instruments report TA-023. Available at: http://www.tainstruments.co.jp/application/pdf/Thermal_Library/Applications_Briefs/TA023.PDF.

8. van Lith, S. C.; Alonso-Ramírez, V.; Jensen, P. A.; Frandsen, F. J.; Glarborg, P., Release to the Gas Phase of Inorganic Elements during Wood Combustion. Part 1: Development and Evaluation of Quantification Methods. Energy & Fuels 2006, 20, (3), 964–978.

9. Houshfar, E.; Wang, L.; Vähä-Savo, N.; Brink, A.; Løvås, T., Experimental Study of a Single Particle Reactor at Combustion and Pyrolysis Conditions. Chemical Engineering Transactions 2013, 35, 613–618.

10. Werkelin, J.; Skrifvars, B.-J.; Hupa, M., Ash-forming elements in four Scandinavian wood species. Part 1: Summer harvest. Biomass and Bioenergy 2005, 29, (6), 451–466.

11. Wang, L.; Sandquist, J.; Varhegyi, G.; Matas Güell, B., CO2 Gasification of Chars Prepared from Wood and Forest Residue: A Kinetic Study. Energy & Fuels 2013, 27, (10), 6098–6107.

12. Khalil, R.; Várhegyi, G.; Jäschke, S.; Grønli, M. G.; Hustad, J., CO2 Gasification of Biomass Chars: A Kinetic Study. Energy & Fuels 2008, 23, (1), 94–100.

Chapter 5

System studies on biomass-to-liquids integrated to forest industry

Jim Andersson and Joakim Lundgren, Luleå University of Technology, Sweden

Contents

1. System studies on biomass-to-liquids integrated to forest industry

1.1 Introduction

Large scale production of biomass based motor fuels and green chemicals will most likely be integrated in existing pulp mills and other large forest industries. This is, amongst other things, due to the already existing biomass handling infrastructure and the possibility to exploit by-products. In chemical pulp mills, gasification of black liquor is a highly interesting technology for motor fuel and chemical production. Another interesting technology is direct gasification of forest residues. Operating the two technologies in combination, i.e. in parallel, constitute a third interesting option, where both upstream (oxygen plant) and downstream process equipment (gas conditioning units and synthesis loop) can be co-utilized resulting in enhanced economies of scale.

The main aim of this sub-project was to techno-economically investigate the opportunity to integrate a pressurised entrained flow biomass gasifier process for green chemical production (methanol and ammonia) into an existing pulp and paper mill. The objectives were to find possible and measurable added values with integrated system solutions compared to stand-alone units. The evaluations were performed by calculating the overall system efficiency for all production cases (non-integrated and integrated systems). The process economics was evaluated via a cash flow analysis (IRR) complemented with a sensitivity analysis.

1.2 Material and method

A process integration (PI) model was used to evaluate the integration of gasification based methanol or ammonia production in an existing pulp and paper mill. The most important modelling constraint was to maintain the pulp production, which consequently translate to a maintained process steam balance. A detailed Aspen Plus process model was used to model energy and material balances of the complete biomass gasification system. The system boundary for the biomass gasification model ranges from incoming raw biomass to the main final syngas product, i.e. methanol or ammonia. An iterative modelling approach between the

two models was adopted to ensure that all constraints of the pulp and paper mill as well as for the gasification plant were met. The resulting material and energy balances were used to analyze the different system configurations in terms of overall energy efficiency and process economics.

1.2.1 The process integration model

The PI model was based on mathematical programming, i.e. mixed integer linear programming (MILP) using a Java based software – reMIND [1]. The model structure is represented by a network of nodes and branches, where each node contains linear equations to express the materials and energy balances of each steam generating units and steam consumers in the mill. The branches connect the steam generating units and steam consumers in the mill, by representing the internal network of material and energy flows. Thus an entire energy system is created. The model of the existing mill configuration was validated against operational data. The model development and validation are further described in [2].

1.2.2 Modelling of the biomass gasification system

The main process steps during thermo-chemical conversion of biomass into syngas and subsequent syngas upgrading to green chemicals are illustrated in Figure 1. The dashed line describes the case configuration when a black liquor gasifier (BLG) and a solid biomass gasifier are operated in parallel.

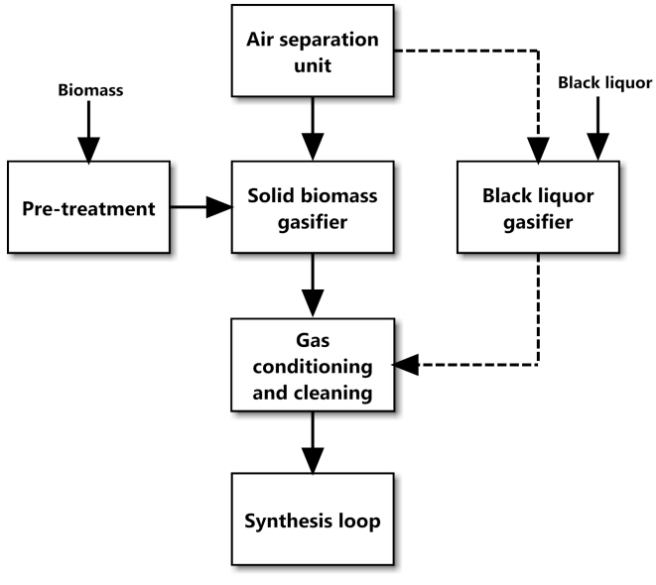

Figure 1. Simplified flowsheet of the modelled gasification plants in Aspen Plus.

The gasifier model was based on the PEBG technology and created in Aspen Plus. The PEBG was modelled in a detailed manner treating the major reaction steps in the gasifier separately (drying, pyrolysis, char combustion and gasification). The zones were internally connected by material and heat streams. All zones are represented by conventional Aspen Plus blocks, except for the pyrolysis zone, where an external calculator was implemented into the model. This approach increases the dependencies between various parameters and the outcome from the gasifier [3]. The temperature of the syngas leaving the reactor was assumed to be 1200 °C after which the gas was partially quenched to 500 °C. The gasification pressure was set to 30 bar(a) in all the modelling cases.

The short residence time of the entrained particles in the reactor requires that the incoming raw solid biomass feedstock is grinded into sufficiently small particles and dried to the desired water content. This is necessary to achieve a steady operation in the reactor and to enable a high fuel conversion rate. In the model, the incoming biomass was specified according to the ultimate and proximate analysis. The specific power consumption of the dryer was set to 15 kWh/wet ton [4]. The incoming biomass was assumed to be dried to a water content of 8 wt%. Based on the LHV, 1–3% of the thermal input is required for power consumption for size reduction. In the modelling, 3% of the thermal input was assumed.

The entrained flow BLG was modelled using the same approach as described for the PEBG and the results were validated against gas composition data presented in [5]. Typical black liquor contains 19.4 wt% sodium and 5 wt% sulphur [5]. The sulphur content in the black liquor has a higher tendency to form H_2S via black liquor gasification route than the combustion alternative [6]. A weaker green liquor was therefore recovered when black liquor is gasified compared to when combusted in a recovery boiler. The outgoing syngas from the black liquor gasifier was quenched to saturated water temperature.

An air separation unit (ASU) supplies pure oxygen to the gasifier. The power demand for a cryogenic air separation unit producing oxygen with 99.6 mol% purity was assumed to consume 1.0 $MW_e/(kg\text{-}O_2/s)$ [7].

1.2.3 Modelling of the gas cleaning, conditioning and synthesis

For the downstream catalysts, a hydrogen (H_2) to carbon monoxide (CO) ratio slightly above 2 in the syngas favours the methanol generation. For ammonia production, the H_2 content in the syngas should be maximized. This is because ammonia is formed by the reaction between H_2 and N_2. Depending on the gasifier type (i.e. PEBG or BLG) the actual H_2:CO ratio of the gas leaving the gasifier is normally in the range of 0.6–1.0 with a hydrogen content in the range of 25–40 vol%. A sulphur tolerant water gas shift (WGS) reactor was therefore required to raise the H_2 concentration by converting CO and steam to H_2 and CO_2.

An acid gas removal (AGR) unit was placed after the WGS, to remove the sulphur contaminations as well as CO_2, NH_3 and HCl. The AGR unit uses cooled methanol to remove separated unwanted impurities and gas species, similar to the Rectisol process [7]. In the case when the BLG was operating in parallel to the

PEBG, the sulphur content in the syngas became considerably higher. The sulphur rich stream from the AGR process was then supplied to a Claus sulphur recovery unit, where the elemental sulphur was recovered [6].

The pressure of the shifted and cleaned syngas was raised to the operating pressure of the methanol catalyst (106 bar with a Δp of 8 bar, [8]) by a multistage compressor. The low conversion rate in the catalyst requires recycling of the gas. A fraction of the recycled gas was withdrawn in order to prevent accumulation of inert gas in the methanol synthesis loop. The purged off-gases contain a large amount of volatiles gases and are thereby suitable for combustion for heat recovery purposes. Before recycling the unreacted gases, methanol, water and some CO_2 were separated for further purification. The heat needed for distillation was generated by condensation of 4 bar steam. Steam was raised in the methanol synthesis both by maintaining a constant exit temperature of 260 °C out from the catalyst and by cooling the outgoing gas prior to the methanol separation.

When ammonia was produced, a liquid N_2 wash was also required. The N_2 wash was located downstream the AGR unit and used the already cooled and partly conditioned syngas. Remaining methanol from the AGR unit and the residual traces of CO_2 in the syngas needs to be removed before the N_2 wash to avoid freezing problems in the cold box heat exchanger. Remaining CO was also removed due to its poisonous effect on ammonia catalysts [9].

After the N_2 wash, the outgoing syngas was mixed with N_2 fixed from regular air to reach the desired 3:1 ratio between H_2 and N_2 [9]. The syngas was pressurized to the operating pressure of the ammonia catalyst (180 bar) before entering the synthesis loop. The ammonia synthesis takes place over an iron promoted catalyst [10], modelled using a Gibbs reactors with an outgoing gas temperature of 440°C. The conversion efficiency is typically in the range of 20-30% per pass. Recycling of unreacted gases is necessary to increase the ammonia production [11]. The ammonia reaction is exothermic, thus cooling of the outgoing gases generates high quality steam [10]. The produced ammonia was separated from the unreacted gases by condensation in a refrigeration system. Part of the recycled gas needs to be purged to avoid inter gas accumulation in the synthesis loop [10].

1.3 Case description

The Billerud Karlsborg AB pulp mill, located in the northern part of Sweden, was used as case basis. This chemical pulp and paper mill produce pulp via the so-called kraft process (i.e. sulphate process). In the process of making wood pulp (basically pure cellulose fibers), wood chips and white liquor (NaOH and Na_2S) are cooked in a digester to dissolve the hemicellulose and lignin in order to release the cellulose fibers. The resulting wood pulp continues along the fibre line that extends until the pulp bleaching/paper making section of the mill, see Figure 2.

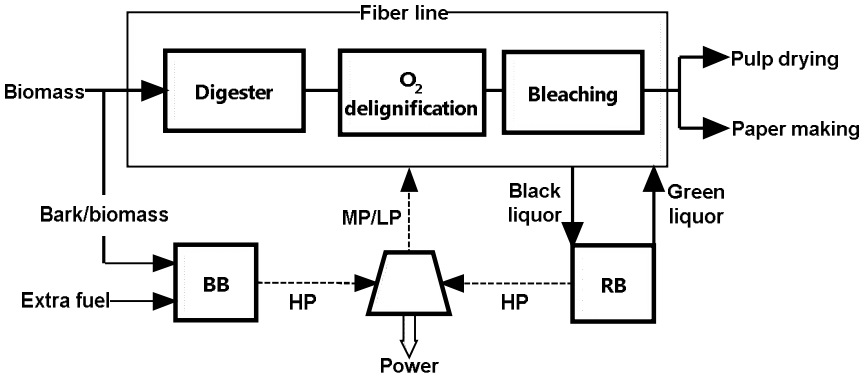

Figure 2. Conventional fibre line and chemical looping.

An integrated (closed) chemical recovery cycle is a necessary part of the mill in order to make the overall process economically feasible and environmentally sound. Black liquor is a by-product from the pulp cooking that contains the spent cooking chemicals (inorganic matter) and dissolved organic matter in form of smaller lignin fragments, carbohydrates from the dissolved hemicellulose and extractives. The solid content of the outgoing black liquor from the digester is typically around 15 wt%. A multi-effect evaporator unit is used to raise the solid content of the black liquor to improve the efficiency and the chemical recovery in the downstream recovery boiler (RB). By combusting concentrated black liquor in a RB, the organic part provides heat and electricity to the mill simultaneously as the inorganic part is partly regenerated back to cooking chemicals. The final chemical regeneration to white liquor (NaOH and Na_2S) is made in a causticizing plant (i.e. lime kiln). In the process of concentrating black liquor, rosin soap (another by-product) separates from the black liquor and is possible to extract. By removing the rosin soap a more efficient energy and chemical recovery can be achieved. The extracted rosin soap can be further processed into tall oil that internally can be used as a fuel in the lime kiln.

The heat generated from combustion of black liquor in the RB, is recovered to generate high pressure (HP) steam. A biomass fired bark boiler (BB) is used to cover the marginal steam demand of the mill, by combusting internal surplus of bark with the required extra biomass (or oil depending on the current fuel market price). The produced HP steam expands to medium pressure (MP) and low pressure (LP) steam in a turbine. A small quantity of the steam is extracted at intermediate pressure for soot-blowing of the RB, while MP and LP steam are consumed in the internal processes in the pulp and paper mill. The key energy data of the reference mill is presented in Table 1.

Table 1. Current key energy data of the reference mill (MW).

Electricity produced/purchased	35/16
Steam production for internal consumers	208
Biomass to bark boiler total consumption/purchased	51/7
Oil to recovery boiler	5
Tall oil to lime kiln	17

Three different case configurations were considered, a non-integrated stand-alone (Case A) gasification unit and two integrated gasification systems (Case B and C). In Case A, the PEBG was operated as a stand-alone gasification plant alongside the mill. To be able to compare the different cases, the production capacity of the stand-alone plant was determined by Case B, meaning that the thermal input of the biomass to the PEBG is equal as in Case B. Heat was recovered for steam generation to satisfy the internal steam demand. The recovered surplus heat was assumed to be sold as district heating during the heating season (assumed to correspond to 5,000 hours per year).

In Case B, the BB was removed and replaced by a PEBG unit for either methanol or ammonia production. The available heat surplus from the gasification processes were not suitable to be recovered as (HP) steam. The HP steam generated by the boilers in the mill was used to produce electricity and to some extent soot-blowing of the RB. Only MP and LP steam were necessary for the pulp and paper making. The modelling constraint was, as previously mentioned, to keep the pulp and paper production unaltered by maintaining the MP and the LP steam balance. It was furthermore assumed that the internal surplus of bark originally used in the BB could be pre-treated (dried and grinded) and used as a fuel in the PEBG together with required additional biomass. The excess off-gas (purge gas) from the synthesis loops and the tail gas from the N_2-wash (when ammonia was produced) were assumed to replace/reduce the firing oil demand in the lime kiln. The surplus tall oil was assumed to be sold on the market.

In Case C, the RB was replaced by a BLG operating in parallel with a PEBG. The most important constraint was also here to maintain the MP and LP steam balance of the mill. Since the amount of available black liquor is dependent on the pulp production capacity, the size of the BLG is fixed.

The size of the PEBG unit was therefore dimensioned to produce the marginal steam demand to maintain the steam balance of the mill. The bark boiler was kept in operation in this case to limit the size of PEBG unit. The weaker green liquor (compared to combustion), can be compensated by increasing the causticization by 25% [12], i.e. increasing the lime kiln fuel demand. The purge gas from the synthesis loop and the tail gas from the N_2-wash (only used for ammonia production) are valuable gases that can be used as supplement to the tall oil use in the lime kiln. The surplus tall oil can be sold on the market.

Figure 3 illustrates how the green chemical (methanol or ammonia) production pathways affect the pulp mill in the different integration cases (Case B–C). The

biomass used for pulp making and the final pulp products were the same for all three cases.

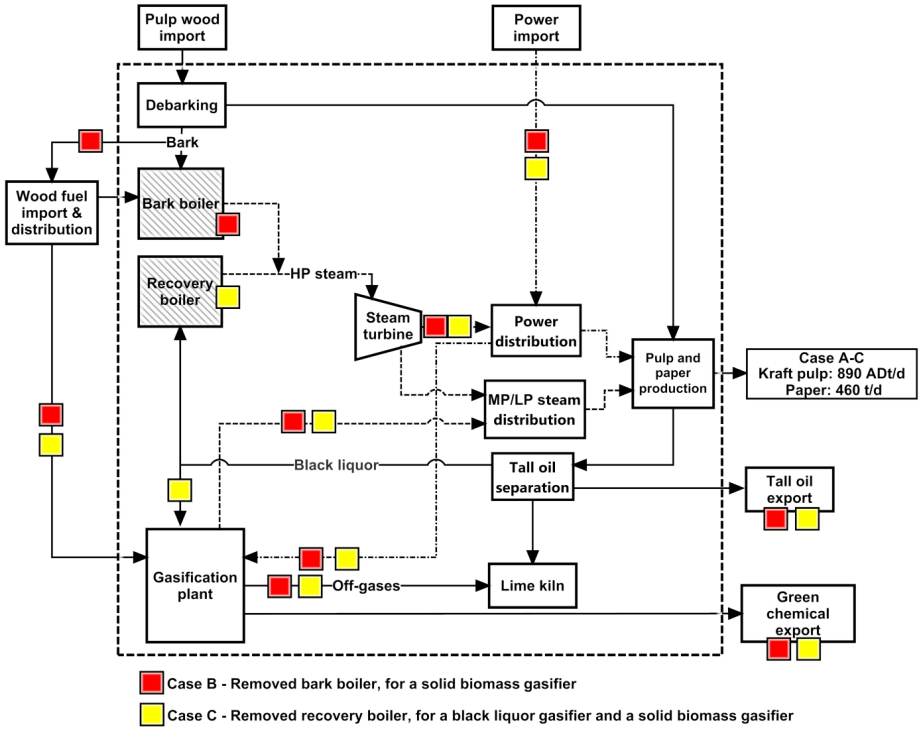

Figure 3. Generic overview of a pulp and paper mill with the integrated biomass gasification pathways. The coloured boxes specify which units/streams that is active/affected in the different integration scenarios. A hatched unit indicates a process that is removed after integration.

1.3.1 Overall energy system analysis

The overall energy system efficiency was estimated using electricity equivalents, all energy carriers being converted to their corresponding electricity equivalents (see Table 2) according to the efficiency of the best-available technologies known to the authors. Only using mixed sources of energy carriers in MW_{out}/MW_{in} for efficiency calculations contributes to a tendency to overestimate the “quality” of certain energy carriers, especially when the level of exergy in the different flows (biomass, bark, hot water, steam, power, motor fuel and chemical products) may be highly diverse [13].

Table 2. Power generation efficiencies used for calculation of the electricity equivalents.

Energy carrier	Power generation efficiency (η)	Reference
Biomass	46.2%	[13]
Methanol	55.9%	[13]
Ammonia [a)]	49%	
Tall oil	57.6%	Assumed the same as methanol
Hot water, 95 °C	10%	[13]

a) Ammonia is converted into its electrical equivalent by multiplying the methanol power generation efficiency with the ratio of the lower heating values between ammonia and methanol.

The material and energy balances in Case B and C were calculated on an incremental basis compared to the operation of the pulp mill prior to the integration, i.e., required marginal supply of biomass and other energy carriers needed to produce a biofuel or green chemical.

The system efficiencies for all configurations were therefore calculated based on the marginal energy supply (Q) and later converted to electrical equivalents by the first law of thermodynamics according to (1):

$$\eta_{EL} = \frac{\eta_{Green\,chem.} \cdot Q_{Green\,chem.} + \eta_{Other} \cdot Q_{Other}}{\eta_{Biomass} \cdot Q_{Biomas} + Q_{Power} + \eta_{Other} \cdot Q_{Other}} \quad (1)$$

The subscripts denote the different material and energy flows. The system boundaries used for the overall system efficiency calculations is illustrated by the dashed boxes in Figure 4. The integrated gasification units (Case B and Case C) were compared to the original operation of the pulp and paper mill and the stand-alone gasification plant (Case A) to analyse the effects on the overall energy system and to determine the most effective production alternative. The material and energy streams in the stand-alone gasification plant were therefore included in the overall system efficiency calculation for Case A. Biomass for pulp making and the final pulp products are not accounted for in the resulting overall energy system efficiency calculations. Bark is an unwanted biomass sort in the cooking process due to its high ash content and other contaminations. The bark was therefore not accounted for as pulp making biomass

1.3.2 Economic calculations and sensitivity analysis

In the economic calculations, the incremental investment, calculated as the difference between the investment in a new boiler and the investment in an integrated gasification plant were used in Case B–C. This implies that the mills' bark or recovery boiler is old and an investment in a new unit is required in any case. Costs and revenues associated with the original operation of boiler was included in Case

A, where the cost of operation and maintenance was taken from the “Mill stand-alone case” presented in [14].

The annual capital cost was calculated by multiplying an annuity factor to the investment cost of the gasification plant. An annuity factor of 12% corresponding to an economic lifetime of 20 years and a 10% interest rate was used in the production cost calculations. The investment cost for equipment and assembly was calculated as the over-night installation cost by the sum of the major units (pre-treatment, gasifier, AGR, etc). The investment costs for each unit were calculated according to the actual capacity, reference size and reference investment cost according to (2):

$$I = I_{ref} \cdot \left(\frac{P}{P_{ref}}\right)^{n} \cdot F \qquad (2)$$

where I and P denotes the investment and size, respectively. The subscript (ref) refers to the investment cost and size of the reference plant. n denotes the scale factor and F is the overall installation factor. Reference size and cost for the major units in the plant are all in detailed presented in [15] and [16].

Methanol was assumed to be sold to replace fossil gasoline (selling price 1.67 Euro/litre gasoline) with a distribution cost of 0.222 Euro/litre gasoline equivalents. Ammonia was assumed to be sold to replace fossil fuel based ammonia (selling price 514 €/ton, [17]). The biomass feedstock cost was assumed to 22 €/MWh and the cost of electricity to 63 €/MWh. In the economic evaluations, the produced methanol and the ammonia were assumed to be exempted from taxes when sold. The cost and selling price for the other commodities and products were based on the “*today case*” published in [15].

The above selling prices for methanol and ammonia were used for calculation of the internal rate of return (IRR) in a cash flow analysis. In the cash flow analysis, a start-up period was considered, where the production capacity was 25% of maximum during year one and thereafter increased by 25%-points per year until the fourth year when the maximum production capacity was reached. The investment cost was assumed to be paid during a three year construction period. The influence of a ±30% fluctuation of the biomass feedstock cost and the investment cost were also investigated.

1.4 Results and discussion

The material and energy balances for the different case configurations for each final product are presented in Figure 4. The gasification capacities for the ammonia production were roughly 100–150 MW_{th} smaller, compared to when methanol was produced. The reason was that more steam is generated per ton of biomass input during ammonia production than during methanol production, primarily due to the operating condition of the ammonia synthesis (i.e. high operating pressure and high temperature). Moreover, the methanol production cases consistently

received higher overall system efficiency (calculated as electricity equivalents) than for the ammonia cases, see Figure 4. This was mainly due to that the ammonia production required significantly more electric power than the methanol production.

The recovery boiler generates almost 80% of the total HP steam in the original operation of the pulp mill. By replacing the recovery boiler with a PEBG unit operated in parallel with a BLG (Case C) nearly no HP steam was produced. A zero power production was therefore accounted for in Case C (see Figure 4) for both products.

The results showed that the non-integrated case, Case A, reached an overall system efficiency of 50% when methanol was produced. The system efficiency increased to 57% when the bark boiler was removed in favour of an integrated methanol production pathway (Case B). The reasons were mainly that the available internal surplus of biomass (bark) was more effectively used in Case B and the possibility to export the liberated tall oil. Replacing the recovery boiler (in Case A) by a black liquor gasifier operated in parallel with a PEBG unit also increased the system efficiency to 57%.

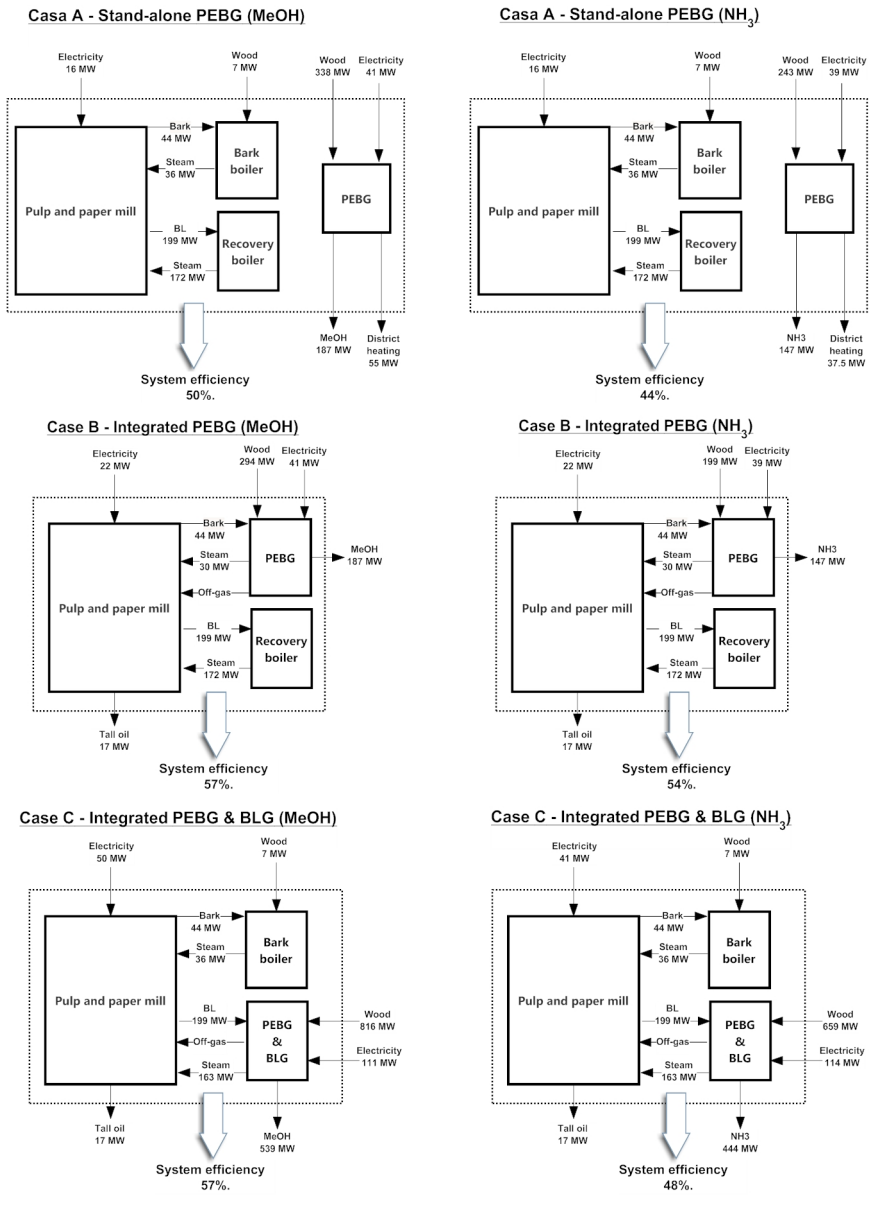

Figure 4. Energy and material balances for the methanol (left side) and the ammonia (right side) cases. The dashed boxes represent the system boundaries used for the overall energy efficiency calculations**.**

The non-integrated stand-alone plant (Case A) reached an overall energy system efficiency of 44%, when ammonia was produced. By replacing the bark boiler with the PEBG unit in Case B, two additional product streams

(ammonia and tall oil) were added to mill's existing production. This increased the required biomass import to the mill by 50%, while the electricity production decreased (due to lower production of HP steam) while the electricity consumption was almost doubled. The calculations showed, however, that the overall system efficiency was increased by 10%-units compared to the Case A. The reasons were, as Case B when methanol was produced, a more efficient use of the surplus bark and the possibility to export tall oil. The zero power production in combination with the high power demand in Case C reduced the energy-related advantages from integration in comparison to Case B. The system efficiency in Case C was however improved by 4%-units compared to Case A.

Total investment cost (CAPEX), IRR and EBITDA (earnings before interest, taxes, depreciation and amortization) are presented in Figure 5 and 6 for the methanol and the ammonia cases, respectively. Avoided boiler investments for the integrated cases and the investment in the new bark boiler in the stand-alone case were accounted as operating costs (e.g. in the EBITDA). The methanol production cost was lowered by 41 and 22 €/ton produced methanol for the integrated Cases B and C, respectively, in comparison to the stand-alone plant (Case A, 507 €/ton). The effect of the zero electricity production in Case C became evident in the production cost calculations and was one of the main reasons why Case C received a higher methanol production cost than Case B. However, the economy-of-scale effect reduces the investment cost for Case C and this case receives a slightly higher IRR in comparison to Case A and B (see Figure 5). Still, Case A and B showed attractive production profitability.

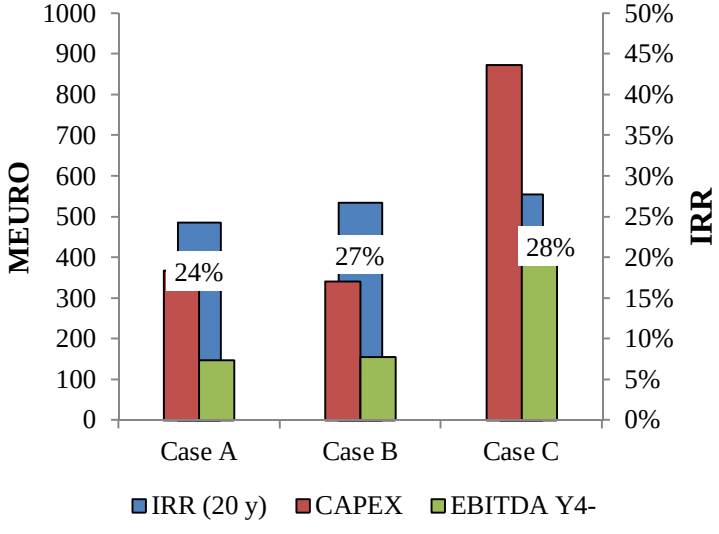

Figure 5. Result of the cash flow analysis for methanol as the main final product.

When ammonia was produced, approximately 45% of the total investment cost was directly connected to the synthesis loop in Case A and B. This indicates that the ammonia production capacities of the studied configurations (228 000 t/y NH_3) were rather small. The larger production capacity in Case C reduced the investment cost per ton of produced ammonia (see Figure 6) and the synthesis loop accounts for less than 40% of the total investment cost. Although, the positive economy-of-scale effect was diminished by the lower overall system efficiency reached in Case C compared to Case B. The ammonia production cost was therefore reduced in the same range (65 €/t) in both Case B and C in comparison with Case A (540 €/ton). Considering the internal rate of return, Case B receives the highest IRR, see Figure 6.

Production of ammonia via gasification of lignocellulosic biomass is, per MW of produced chemical, significantly more capital intensive than methanol production. In combination with the small annual revenues, the received IRR was rather low for all of the ammonia cases. By comparing the results from the cash flow analysis between the two products (Figure 5 and 6), the production profitability seems much more viable for the methanol production pathways.

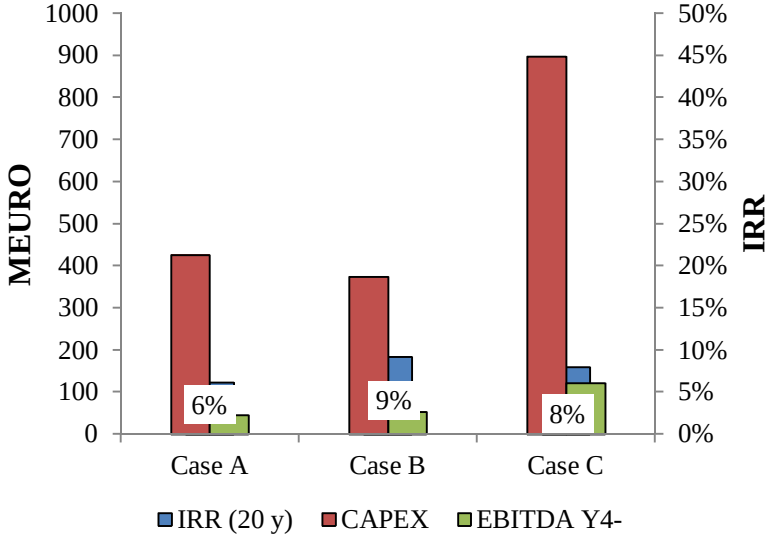

Figure 6. Result of the cash flow analysis for ammonia as the main final product.

Figure 7 and 8 shows the result of a sensitivity analysis of the IRR for the methanol as well as the ammonia production cases. A feedstock price variation of ±30% resulted in an IRR change by maximum ±3%-units in all production cases. Given an investment cost reduction of 30% for the ammonia cases the percental increase of the IRR can be as high as 80% (Case C). At an investment cost reduc-

tion by 20% or more, Case C seemed to be the best alternative among the ammonia cases when considering the IRR.

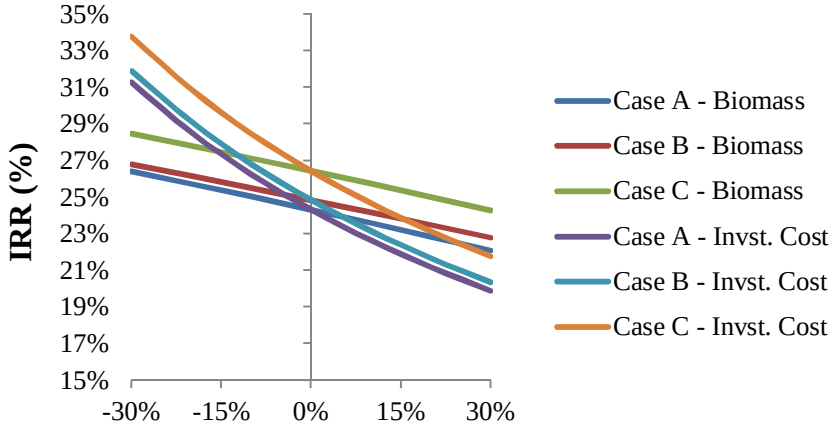

Figure 7. Results of the sensitivity analysis for Cases A-C with methanol as the main final product.

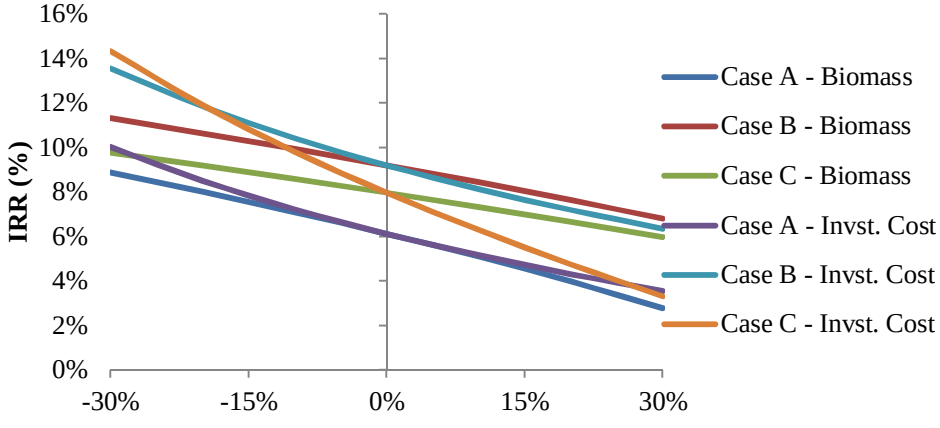

Figure 8. Results of the sensitivity analysis for Cases A-C with ammonia as the main final product.

1.5 Conclusions

The main objective of this work was to perform a techno-economic evaluation of methanol and ammonia production via integrated biomass gasification in an existing pulp and paper mill. In general, methanol assumed to replace fossil gasoline showed good production profitability if exempted from taxes. The ammonia production was per produced unit, significantly more capital intensive than methanol

production. The plant profitability in the ammonia cases was therefore lower in comparison to the profitability in the methanol cases. The highest efficiency and the most favourable economic benefits were reached when methanol was produced via parallel operation of a solid biomass gasifier and a black liquor gasifier. Favourable economies of scale effects were also obtained for this system due to the possibility to co-utilize upstream (air separation unit) as well as downstream process equipment (gas conditioning units and synthesis loop).

The main conclusion was that green chemical production via industrially integrated biomass gasification show technical and economic benefits compared to stand-alone production alternatives. Integration of large scale biomass gasification system is therefore important in the development towards a more sustainable green chemical production.

References

[1] Karlsson M. The MIND method: A decision support for optimization of industrial energy systems – Principles and case studies. Applied Energy 2011;88(3):577–589.

[2] Ji X, Lundgren J, Wang C, Dahl J, Grip C-E. Simulation and energy optimization of a pulp and paper mill – Evaporation plant and digester. Applied Energy 2012;97:30–37.

[3] Andersson J, Lundgren J. Modeling of a Pressurized Entrained Flow Biomass Gasifier in Aspen Plus. In: Proc. of the 3rd International Congress on Green Process Engineering. Kuala-Lumpur, Malaysia 2011.

[4] Sues A. Are European bioenergy targets achievable? An evaluation based on thermoeconomic and environmental indicators. Department of Chemical Engineering and Chemistry. Eindhoven: Eindhoven University of Technology 2011.

[5] Carlsson P. Large Scale Experiments and Modeling of Black Liquor Gasification. Division of Energy Engineering. Luleå, Sweden: Luleå University of Technology 2011. 65 p.

[6] Ekbom T, Lindblom M, Berglin N, Ahlvik P. Black liquor gasification with motor fuel production – BLGMF. Report, Stockholm, Sweden, Contract No. 4.1030/Z/01-087/2001. 2003.

[7] Clausen LR, Elmegaard B, Houbak N. Technoeconomic analysis of a low CO_2 emission dimethyl ether (DME) plant based on gasification of torrefied biomass. Energy 2010;35(12):4831–42.

[8] Hamelinck CN, Faaij APC. Future prospects for production of methanol and hydrogen from biomass. Journal of Power Sources 2002;111(1):1–22.

[9] Higman C, van der Burgt M. Gasification. 2th ed. Burlington, USA: Elsevier Science 2008. Pp. 354–55.

[10] Spath PL, Dayton DC. Preliminary screening – technical and economic assessment of synthesis gas to fuels and chemicals with emphasis on the potential for biomass-derived syngas. Golden, Colorado, USA: National Renewable Energy Laboratory, NREL 2003.

[11] Ahlgren S, Baky A, Bernesson S, Nordberg Å, Norén O, Hansson P-A. Ammonium nitrate fertiliser production based on biomass - Environmental effects from a life cycle perspective. Bioresource Technology 2008;99(17):8034-41.

[12] Ekbom T, Lindblom M, Berglin N, Ahlvik P. Technical and Commercial Feasibility Study of Black Liquor Gasification with Methanol/DME Production as Motor Fuels for Automotive Uses – BLGMF. ALTENER Programme Report, Contract No. 4.1030/Z/01-087/2001. 2003.

[13] Tunå P, Hulteberg C, Hansson J, Åsblad A, Andersson E. Synergies from combined pulp&paper and fuel production. Biomass and Bioenergy 2012;40:174–180.

[14] Wetterlund E, Pettersson K, Harvey S. Systems analysis of integrating biomass gasification with pulp and paper production - Effects on economic performance, CO2 emissions and energy use. Energy 2011;36(2):932–941.

[15] Andersson J, Lundgren J, Marklund M. Methanol production via pressurized entrained flow biomass gasification – Techno-economic comparison of integrated vs. stand-alone production. In Press Biomass and Bioenergy 2014.

[16] Andersson J, Lundgren J. Techno-economic analysis of ammonia production via integrated biomass gasification. In Press Applied Energy 2014.

[17] ICIS pricing, Reed business information limited. December report on ammonia selling prices in Europe and Asia Pacific. 2012. <http://www.icispricing.com/> [accessed February 2013].

Acknowledgements

The authors acknowledge the financial support of the Nordic Energy Research project "Biomass gasification fundamentals to support the development of BTL in forest industry" known as the NORDSYNGAS-project.

Series title and number

VTT Technology 210

Title	**Biomass gasification fundamentals to support the development of BTL in forest industry** Publishable final scientific report of Nordsyngas project
Author(s)	Minna Kurkela (Ed.)
Abstract	The Nordic forest industry creates new concepts and provides solutions to mitigate climate challenge. One of the most interesting concepts is the integrated production of pulp and paper products and transportation fuels. The Finnish and Swedish activities are aiming to the same objective increased profitability of pulp and paper industry by using their by-products for producing high-quality renewable fuels. The technical approaches are different. For the technologies the scientific co-operation in the R & D consortium of VTT-ETC-LTU-SINTEF created background know-how through experiments and modelling in NORDSYNGAS project realised between 2010–2014. The objective of the project was to create new scientific knowledge on fluidised-bed and entrained-flow gasification of biomass residues and black liquor in order to support the Nordic industrial development and demonstration projects. In addition, close co-operation between the Finnish, Swedish and Norwegian R&D organisations was organised.
ISBN, ISSN	ISBN 978-951-38-8220-4 (URL: http://www.vtt.fi/publications/index.jsp) ISSN-L 2242-1211 ISSN 2242-122X (Online)
Date	February 2015
Language	English
Pages	201 p.
Name of the project	Nordsyngas
Commissioned by	Nordic Energy Research
Keywords	gasification, char, reactivity, modelling, slag
Publisher	VTT Technical Research Centre of Finland Ltd P.O. Box 1000, FI-02044 VTT, Finland, Tel. 020 722 111

Biomass gasification fundamentals to support the development of BTL in forest industry

Publishable final scientific report of Nordsyngas project

The Nordic forest industry creates new concepts and provides solutions to mitigate climate challenge. One of the most interesting concepts is the integrated production of pulp and paper products and transportation fuels. The Finnish and Swedish activities are aiming to the same objective increased profitability of pulp and paper industry by using their by-products for producing high-quality renewable fuels. The technical approaches are different. For the technologies the scientific co-operation in the R & D consortium of VTT-ETC-LTU-SINTEF created background know-how through experiments and modelling in NORDSYNGAS project realised between 2010–2014. The objective of the project was to create new scientific knowledge on fluidised-bed and entrained-flow gasification of biomass residues and black liquor in order to support the Nordic industrial development and demonstration projects. In addition, close co-operation between the Finnish, Swedish and Norwegian R&D organisations was organised.

ISBN 978-951-38-8220-4 (URL: http://www.vtt.fi/publications/index.jsp)
ISSN-L 2242-1211
ISSN 2242-122X (Online)